TIME DOMAIN SIMULATION WITH APPLICATIONS IN COMPLIANT WORKPIECE MILLING

by

Mark Andrews Rubeo

A dissertation submitted to the faculty of
The University of North Carolina at Charlotte
in partial fulfillment of the requirements
for the degree of Doctor of Philosophy in
Mechanical Engineering

Charlotte

2016

Approved by:

____
Dr. Tony Schmitz

____
Dr. Matthew Davies

____
Dr. John Ziegert

____
Dr. Scott Smith

____
Dr. Aixi Zhou

ABSTRACT

MARK ANDREWS RUBEO. Time domain simulation with applications in compliant workpiece milling. (Under the direction of DR. TONY L. SCHMITZ)

High performance application fields, such as the defense, power, and aerospace industries, benefit from the enhanced product quality and reduced cost associated with machining thin-walled, metallic structures over traditional fabrication and assembly methods (e.g., sheet metal buildups). The mechanical properties of difficult-to-machine materials, such as titanium and nickel alloys, make them ideal candidates for compliant, thin-walled structures. Near net shape techniques have been used to manufacture compliant structures composed of hard-to-machine materials, but these techniques are often unable to achieve the required dimensional tolerances and surface finishes. Due to the inherent compliance of the preforms, stable machining is difficult to achieve. Prediction of stable machining parameters is therefore critical for the finish machining of such compliant workpieces.

In this research, a time domain simulation is presented for predicting stable and unstable milling conditions with application to finish milling of compliant workpieces. Traditional lobe diagrams provide global stability predictions by dividing the domain of spindle speed and chip width into stable and unstable regions. Time domain simulation provides local information (forces, displacements, etc.) for individual spindle speed-chip width combinations. Stability metrics, based on the local information, are developed to extend the utility of the time domain simulation to provide the global stability predictions of traditional lobe diagrams. The time domain simulation global stability predictions and "local" information are validated experimentally.

DEDICATION

To my parents.

ACKNOWLEDGEMENTS

First and foremost, I would like to thank my academic advisor, Dr. Tony L. Schmitz, under whose direction the work presented in this dissertation was completed. For his mentorship, encouragement, and positivity, I am exceedingly grateful. His work ethic and enthusiasm for engineering are inspiring.

I would like to express my appreciation to my dissertation committee, Dr. Matthew Davies, Dr. John Ziegert, Dr. Scott Smith, and Dr. Aixi Zhou, for their helpful advice and beneficial comments.

Thanks to my colleagues at the University of North Carolina at Charlotte for all the suggestions, support, and helpful discussions.

Finally, I need to thank my wife, sister, and friends for their support throughout this endeavor.

TABLE OF CONTENTS

CHAPTER 1: INTRODUCTION 1

1.1 Project Motivation and Scope 1

CHAPTER 2: LITERATURE REVIEW 4

2.1 Machining Stability 4

2.2 Compliant Workpiece Machining 11

2.3 Low Radial Immersion Milling 13

CHAPTER 3: CUTTING FORCE MODELING 18

3.1 The Mechanistic Approach 20

3.2 Dynamic Compensation of Measured Cutting Forces 21

3.3 Cutting Force Coefficient Determination 28

3.3.1 Average Force, Linear Regression Method 29

3.3.2 Instantaneous Force, Nonlinear Optimization Method 32

3.4 Milling Process Dependent Cutting Force Coefficients 36

3.4.1 Experimental Setup 37

3.4.2 Feed per Tooth Dependence 39

3.4.3 Cutting Speed Dependence 45

3.4.4 Validation Testing 46

3.4.5 Discussion 50

CHAPTER 4: COMPLIANT WORKPIECE MILLING SIMULATION 53

4.1 Time Domain Model 53

4.1.1 Peak-to-Peak Force Diagram 57

4.1.2 Amplitude Ratio Diagrams 59

4.1.3 Spatially Dependent Workpiece Dynamics 63

4.2 Modal Parameter Identification 74

4.2.1 Individual Mode Identification 75

4.2.2 Optimization for All Modes 79

CHAPTER 5: NUMERICAL MILLING SIMULATION COMPARISON 81

5.1 Low Radial Immersion Milling 81

5.2 Helix Angle Induced Islands of Instability 83

CHAPTER 6: EXPERIMENTAL MILLING SIMULATION VALIDATION 87

6.1 Aluminum Milling Stability Validation 87

6.1.1 Experiment Results 92

6.2 Titanium Milling Stability Validation 100

6.2.1 Experiment Results 105

6.3 Spatially Dependent Workpiece Dynamics Validation 111

6.3.1 Experiment Results 116

CHAPTER 7: CONCLUSIONS 121

REFERENCES 124

APPENDIX A: ARBITRARY RADIAL IMMERSION CUTTING FORCE COEFFICIENT SOLUTION 131

APPENDIX B: SUPPLEMENTARY EXPERIMENTAL MILLING SIMULATION VALIDATION 134

B.1 Titanium Milling Stability Validation 134

B.2 Spatially Dependent Workpiece Dynamics Validation 140

LIST OF TABLES

TABLE 3.1: Milling process parameters selected for cutting force measurements. 39

TABLE 3.2: Specific force coefficients calculated using the average force, linear regression method for the 10% radial immersion up milling cut conducted at a spindle speed of 8 krpm. 41

TABLE 3.3. Specific force coefficients calculated using the average force, linear regression method for the 10% radial immersion down milling cut conducted at a spindle speed of 8 krpm. 43

TABLE 3.4: Cutting force coefficients used for milling stability predictions using the PTP force diagram. 48

TABLE 4.1: Material properties for Ti6Al4V 65

TABLE 5.1: Cutting tool modal parameters obtained from impact testing. 82

TABLE 5.2: Modal parameters for the workpiece (flexure) measured using impact testing. 84

TABLE 6.1: Nominal geometric dimensions of the flexible ribs. 88

TABLE 6.2: Modal parameters for the cutting tool. 89

TABLE 6.3: Modal parameters for ribs 1 and 2. 90

TABLE 6.4: Cutting force coefficients used in the time domain simulation. 90

TABLE 6.5: Nominal geometric dimensions of the flexible ribs. 102

TABLE 6.6: Modal parameters for the cutting tool. 103

TABLE 6.7: Modal parameters of the compliant workpiece's first bending mode for different rib thicknesses. 104

TABLE 6.8: Cutting force coefficients used in the time domain simulation. 105

TABLE 6.9: Nominal geometric dimensions of the flexible ribs. 113

TABLE 6.10: Modal parameters for the cutting tool. 114

TABLE 6.11: Modal parameters for the compliant workpiece. 115

TABLE 6.12: Cutting force coefficients used in the time domain simulation. 115

LIST OF FIGURES

FIGURE 2.1: Constant chip thickness when the relative vibrations between the cutting tool and workpiece between two successive passes of the cutting tool are in-phase. 6

FIGURE 2.2: Variation in chip thickness when the relative vibrations between the cutting tool and workpiece between two successive passes of the cutting tool are out-of-phase. 6

FIGURE 2.3: Representative stability lobe diagram detailing stable and unstable chip width-spindle speed combinations. 8

FIGURE 2.4: Representative stability lobe diagram including analytical process damping model. 10

FIGURE 2.5: Poincarè sectioning (i.e., once-per-revolution sampling) of tool motion manifesting as both (a) secondary Hopf instability and (b) period-3 instability [38]. 15

FIGURE 2.6: Stability lobe diagram with secondary Hopf (dashed) and period-2 (solid) stability boundary redrawn from [43]. 17

FIGURE 3.1: Example measurement results of a dynamometer force-to-force FRF in the xyz directions including the coherence and magnitude. 24

FIGURE 3.2: Example results from the two-stage modal fit of a measured dynamometer FRF. 25

FIGURE 3.3: Magnitude response of (a) the inverted, measured dynamometer FRF, (b) second order lowpass filter, and (c) inverse FRF filter. 26

FIGURE 3.4: Example results of the dynamic compensation on the time domain (top) and frequency domain (bottom) cutting forces. 27

FIGURE 3.5: Example results of the dynamic compensation on the x,y, and z components of the measured cutting forces. 28

FIGURE 3.6: Force components and fixed reference frame for the average force, linear regression method. A down milling configuration is shown with a helical endmill. 30

FIGURE 3.7: Measured cutting forces over 100 revolutions of the cutting tool (dotted line) and their average (solid line) shown for a milling operation using a 2-flute cutting tool. 35

FIGURE 3.8: Example results from the nonlinear, optimization method including the measured cutting forces and optimized, simulated cutting forces. 36

FIGURE 3.9: Flow diagram detailing the experimental method used in this study. 37

FIGURE 3.10: Setup for cutting force measurements using a three-axis dynamometer. 38

FIGURE 3.11: Average force, linear regression results from the 10% radial immersion up milling cut conducted at a spindle speed of 8 krpm. 40

FIGURE 3.12: Cutting force coefficients calculated using the instantaneous force, nonlinear optimization method for a 10% radial immersion up milling cut conducted at a spindle speed of 8 krpm. 42

FIGURE 3.13: Cutting force coefficients calculated using the instantaneous force, nonlinear optimization method for a 10% radial immersion down milling cut conducted at a spindle speed of 8 krpm. 43

FIGURE 3.14: The tangential cutting force coefficient, calculated by the instantaneous force, nonlinear optimization method, as a function of radial immersion. 45

FIGURE 3.15: Cutting force coefficients calculated using the instantaneous force, nonlinear optimization method over the range of selected spindle speeds for the 10% radial immersion down milling operation. 46

FIGURE 3.16: Cutting force coefficients calculated using the instantaneous force, nonlinear optimization method for a 10% radial immersion down milling cut conducted at a spindle speed of 8000 rpm. 47

FIGURE 3.17: PTP force diagram generated using the specific force coefficients calculated for a feed rate of 0.05 mmtooth. Stable (circle) and unstable (cross) validation test results are shown. 49

FIGURE 3.18: PTP force diagram generated using the specific force coefficients calculated for a feed rate of 0.25 mmtooth. Stable (circle) and unstable (cross) validation test results are shown. 50

FIGURE 3.19: A milling tool (a) cut into axial disks (b) to facilitate cutting edge radius measurements with an SEM (c). In (c) the flank face is on the left and the rake race is on the right. 52

FIGURE 4.1: Coordinate system definition for the time domain simulation model. A down milling configuration is shown. 55

FIGURE 4.2: Time domain cutting force signal resulting from a simulation conducted at a single spindle speed-axial depth of cut combination with the initial transients and PTP forces denoted. 58

FIGURE 4.3: Example PTP force diagram with process damping region. 59

FIGURE 4.4: The relative displacement of the tool and workpiece given in the time and frequency domains. The tooth passing frequency component and chatter frequency component are indicated, and the amplitude ratio is calculated as 1.56. 61

FIGURE 4.5: Example amplitude ratio diagram. 62

FIGURE 4.6: Representative flexible workpiece with clamped-clamped-clamped-free boundary conditions (a) with refined mesh (b). 65

FIGURE 4.7: First three bending mode shapes for the flexible, thin wall. 66

FIGURE 4.8: Grid of discrete points (green circles) where steady-state dynamic analysis were completed. 67

FIGURE 4.9: Representative frequency response function for two locations at the free edge of the flexible, thin wall. 69

FIGURE 4.10: Measured and simulated workpiece FRF at the location of minimum stiffness for vibration mode one and three (i.e., center of the free edge). 70

FIGURE 4.11: Linearly interpolated mode one stiffness for the flexible, thin wall (a) over the entire *xy* surface (b) and at the free edge (c). 71

FIGURE 4.12: Solid model representation of a peripheral, down milling cut of a flexible, thin wall. 73

FIGURE 4.13: Representative example of time domain simulation outputs including spatially dependent workpiece dynamics. 74

FIGURE 4.14: An illustrative force-to-force FRF with individual modes identified (red circles) and numbered. 76

FIGURE 4.15: The measured force-to-force FRF with the most flexible mode deleted from the response and the removed mode identified by the peak picking method. 78

FIGURE 4.16: The measured FRF and corresponding individual modes identified using the peak picking method. 79

FIGURE 4.17: A comparison of the measured FRF to the fits resulting from the peak picking method and nonlinear optimization. 80

FIGURE 5.1: Stability lobe diagram with secondary Hopf (dashed) and period-2 (solid) stability boundary redrawn from [43] obtained using the semi-discretization method. 82

FIGURE 5.2: Stability lobe diagram with secondary Hopf and period-2 stability boundary using the amplitude ratio method. 83

FIGURE 5.3: Milling stability diagrams for different helical pitches using the semi-discretization method. 85

FIGURE 5.4: Amplitude ratio diagram for different helical pitches using time domain simulation. 86

FIGURE 6.1: Solid model of the flexible workpiece (simulated preform) used for validation testing. 87

FIGURE 6.2: Impact testing setup for the compliant workpiece. 89

FIGURE 6.3: PTP force diagram indicating the selected stable test point for rib 1. 91

FIGURE 6.4. PTP force diagram indicating the selected unstable test point for rib 2. 92

FIGURE 6.5: Coordinate system definition. 93

FIGURE 6.6: Measured and simulated *x*-direction cutting forces for the rib 1 test point (stable case) shown for two cutter revolutions. 93

FIGURE 6.7. Frequency content of the measured (top) and simulated (bottom) *x*-direction cutting forces for the rib 1 test point (stable case). 94

FIGURE 6.8. Measured and simulated *y*-direction cutting forces for the rib 1 test point (stable case) shown for two cutter revolutions. 95

FIGURE 6.9. Frequency content of the measured (top) and simulated (bottom) *y*-direction cutting forces for the rib 1 test point (stable case). 96

FIGURE 6.10. Surface finish of the rib 1 test point (stable case). 96

FIGURE 6.11. Measured and simulated *x*-direction cutting forces for 97

the rib 2 test point (unstable case) shown for two cutter revolutions.

FIGURE 6.12. Frequency content of the measured (top) and simulated (bottom) x-direction cutting forces for the rib 2 test point (unstable case). 98

FIGURE 6.13. Measured and simulated y-direction cutting forces for the rib 2 test point (unstable case) shown for two cutter revolutions. 99

FIGURE 6.14. Frequency content of the measured (top) and simulated (bottom) y-direction cutting forces for the rib 2 test point (unstable case). 99

FIGURE 6.15. Surface finish of the rib 2 test point (unstable case). 100

FIGURE 6.16: Solid model of the flexible workpiece (simulated preform) used for validation testing. 101

FIGURE 6.17: Experimental setup for the compliant workpiece. 103

FIGURE 6.18: Measured and simulated x direction cutting force shown in the time and frequency domains for the 4 mm thick rib. 106

FIGURE 6.19: Measured and simulated y direction cutting force shown in the time and frequency domains for the 4 mm thick rib. 107

FIGURE 6.20: Measured and simulated z direction cutting force shown in the time and frequency domains for the 4 mm thick rib. 107

FIGURE 6.21: Measured and simulated y direction workpiece velocity shown in the time and frequency domains for the 4 mm thick rib. 108

FIGURE 6.22: Measured and simulated x direction cutting force shown in the time and frequency domains for the 2 mm thick rib. 109

FIGURE 6.23: Measured and simulated y direction cutting force shown in the time and frequency domains for the 2 mm thick rib. 110

FIGURE 6.24: Measured and simulated z direction cutting force shown in the time and frequency domains for the 2 mm thick rib. 110

FIGURE 6.25: Measured and simulated y direction workpiece velocity shown in the time and frequency domains for the 2 mm thick rib. 111

FIGURE 6.26: Solid model of the flexible workpiece (simulated preform) used for validation testing. 112

FIGURE 6.27: Impact testing setup for the compliant workpiece. 114

FIGURE 6.28: Simulated x, y, and z direction cutting forces and y direction workpiece velocity. 116

FIGURE 6.29: Measured and simulated cutting forces in the y direction over the entire cut length (top) and over one revolution of the two flute cutting tool (bottom). 118

FIGURE 6.30: Frequency content of the measured (top) and simulated (bottom) y direction cutting forces. 119

FIGURE 6.31: Measured and simulated workpiece velocity in the y direction over the entire cut length (top) and over two revolutions of the two flute cutting tool (bottom). 120

FIGURE 6.32: Frequency content of the measured (top) and simulated (bottom) y direction workpiece velocity. 120

FIGURE B.1: Measured and simulated x direction cutting force shown in the time and frequency domains for the 3.5 mm thick rib. 134

FIGURE B.2: Measured and simulated y direction cutting force shown in the time and frequency domains for the 3.5 mm thick rib. 135

FIGURE B.3: Measured and simulated z direction cutting force shown in the time and frequency domains for the 3.5 mm thick rib. 135

FIGURE B.4: Measured and simulated y direction workpiece velocity shown in the time and frequency domains for the 3.5 mm thick rib. 136

FIGURE B.5: Measured and simulated x direction cutting force shown in the time and frequency domains for the 3 mm thick rib. 136

FIGURE B.6: Measured and simulated y direction cutting force shown in the time and frequency domains for the 3 mm thick rib. 137

FIGURE B.7: Measured and simulated z direction cutting force shown in the time and frequency domains for the 3 mm thick rib. 137

FIGURE B.8: Measured and simulated y direction workpiece velocity shown in the time and frequency domains for the 3 mm thick rib. 138

FIGURE B.9: Measured and simulated x direction cutting force shown in the time and frequency domains for the 2.5 mm thick rib. 138

FIGURE B.10: Measured and simulated y direction cutting force 139 shown in the time and frequency domains for the 2.5 mm thick rib.

FIGURE B.11: Measured and simulated z direction cutting force shown in the time and frequency domains for the 2.5 mm thick rib. 139

FIGURE B.12: Measured and simulated y direction workpiece velocity shown in the time and frequency domains for the 2.5 mm thick rib. 140

FIGURE B.13: Measured and simulated cutting forces in the x direction over the entire cut length (top) and over one revolution of the two flute cutting tool (bottom). 141

FIGURE B.14: Frequency content of the measured (top) and simulated (bottom) x direction cutting forces. 141

FIGURE B.15: Measured and simulated cutting forces in the z direction over the entire cut length (top) and over one revolution of the two flute cutting tool (bottom). 142

FIGURE B.16: Frequency content of the measured (top) and simulated (bottom) z direction cutting forces. 142

CHAPTER 1: INTRODUCTION

In machining, a rotating cutting tool with defined edges (or teeth) is positioned relative to a workpiece for the purpose of material removal and, therefore, it constitutes a subtractive manufacturing process. One of the limiting factors in machining productivity, which can be described in terms of material removal rate (MMR), is the occurrence of self-excited vibrations between the cutting tool and workpiece. These self-excited vibrations, which yield unstable machining processes, are commonly referred to as chatter. Chatter in machining has been extensively researched over the past 75 years due to its complex nature, which makes its study nontrivial, and its detrimental effects on part quality, which include:

- poor surface quality
- unacceptable dimensional deviations
- excessive noise
- increased tool wear
- potential machine tool damage
- increased production costs.

1.1 Project Motivation and Scope

High performance application fields, such as the defense, power, and aerospace industries, benefit from the enhanced product quality and reduced cost associated with machining thin-walled, metallic structures over traditional fabrication and assembly methods (e.g., sheet metal buildups). A methodology for machining compliant aluminum workpieces described in [1-3] has been widely adopted in the aerospace industry. The manufacturing strategy for these components consists of selectively removing material, via high-speed machining, from a solid billet to yield a monolithic component [4].

The mechanical properties of difficult-to-machine materials, such as titanium and nickel alloys, make them ideal candidates for compliant, thin-walled structures. However, the same machining methodology that has been applied to aluminum is often not appropriate for these materials due to the high material costs and removal rate limitations imposed by tool wear [5]. Near net shape techniques have been used to manufacture compliant structures composed of hard-to-machine materials, but these techniques are often unable to achieve the required dimensional tolerances and surface finishes. Due to the inherent compliance of the preforms, stable machining is difficult to achieve. Prediction of stable machining parameters is critical for the finish machining of such compliant workpieces. Additional complexity is introduced by the nonlinear behavior which can occur during low radial immersion milling when contact between the milling cutter's teeth and the workpiece is highly interrupted [6-9].

The purpose of this project is to evaluate the stability of milling operations where the workpiece is considerably more compliant than the machine-tool system. The evaluation is performed by implementing peak-to-peak (PTP) force diagrams as described in [10] and new amplitude ratio (AR) diagrams. These diagrams result from multiple time domain simulations (TDS) completed over a range of spindle speeds and axial depths of cut. The outcome of an individual time domain simulation contains information specific to the spindle speed-axial depth of cut combination (i.e., cutting force, tool/workpiece deflection), while the PTP force and AR diagrams contain the global information provided by a stability lobe diagram. By proper choice of spindle speed and axial depth of cut according to the PTP force and AR diagrams, stable machining parameters may be selected.

In keeping with the experimental nature of manufacturing research, the predictions obtained via the time domain simulation were validated through the comparison of simulated and measured process output signals such as cutting forces, deflections, velocities, and accelerations. To avoid the complicating effects of tool wear, initial validation testing was performed using 6061 aluminum as the workpiece material. Subsequent validation testing shifted to the material of primary interest: Ti6Al4V. For this material, which is categorized as difficult-to-machine, the high spindle speed ranges are typically inaccessible due to prohibitive tool wear. Because of this effect, the stabilizing phenomenon which occurs at low spindle speeds, referred to as process damping, is utilized to achieve increased material removal rates (MRR). The goal of the project is to validate the time domain simulation and determine efficient machining strategies for finish milling near net shape preforms (in a compliant state) composed of Ti6Al4V.

CHAPTER 2: LITERATURE REVIEW

2.1 Machining Stability

The study of machining vibrations can be traced back to the early 1900s. In work published by Taylor [11] the challenges presented by chatter are noted as the "most obscure and delicate of all problems facing the machinist." However, it wasn't until the 1950s and 1960s that the primary mechanism of chatter was revealed by Tobias, Tlusty, and Merritt [12-14]. Their innovative research, which laid the groundwork for all future research in machining dynamics, showed that the stability of machining operations depends on the relative stiffness and damping of the machine-toolholder-cutting tool system and the workpiece. They realized that the phase between undulations left on the workpiece surface after each pass of the cutting tool dictated the stability.

Because the machine-toolholder-cutting tool system and workpiece are not infinitely rigid, forces that occur during machining result in dynamic deflections which are imprinted on the workpiece surface as a wavy profile. The surface waviness generated by the previous pass of the cutting tool, $y(t-\tau)$, is removed by the current pass of the cutting tool, $y(t)$, at the commanded chip thickness, h_m, where τ is a time delay term which captures this "regeneration of waviness"; see Figure 2.1. In turning, the surface waviness is removed by subsequent rotations of the workpiece and, therefore, the time delay is related to the rotational speed of the workpiece. In milling, the surface waviness is removed by the subsequent cutting tooth, so the time delay is related to the tool's rotational speed and number of cutting teeth.

Tobias, Tlusty, and Merritt [12-14] noted that the phase relationship between the wavy surfaces left behind by successive passes of a cutting tool dictated the stability of the machining operation. In a stable machining operation, the instantaneous, uncut chip thickness variation is negligible resulting in cutting forces with no appreciable variations and dynamic deflections that exhibit diminishing periodic fluctuations. This case, shown in Figure 2.1, occurs when the successive passes of the cutting tool are in-phase. Dynamic deflections still occur for this condition, but the favorable in-phase condition results in (nearly) constant chip thickness. Since the cutting tool and/or workpiece vibrate at their natural frequency, which is characteristic of self-excited vibration, it is apparent that the forcing frequency should be matched to the system's natural frequency.

In an unstable machining operation, the instantaneous, uncut chip thickness variation is large resulting in correspondingly large variations in cutting forces and, subsequently, dynamic deflections. These large fluctuations in chip thickness, cutting forces, and dynamic deflections result in a feedback system that exacerbates the unstable condition. This mechanical vibration regime is referred to as self-excited vibration. This case, shown in Figure 2.2, occurs when successive passes of the cutting tool are out-of-phase.

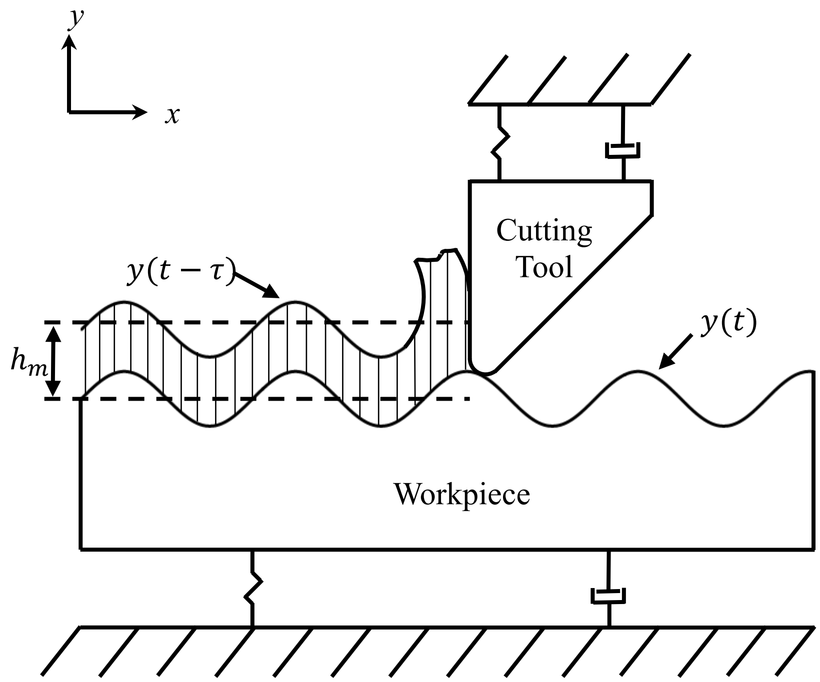

Figure 2.1: Constant chip thickness when the relative vibrations between the cutting tool and workpiece between two successive passes of the cutting tool are in-phase.

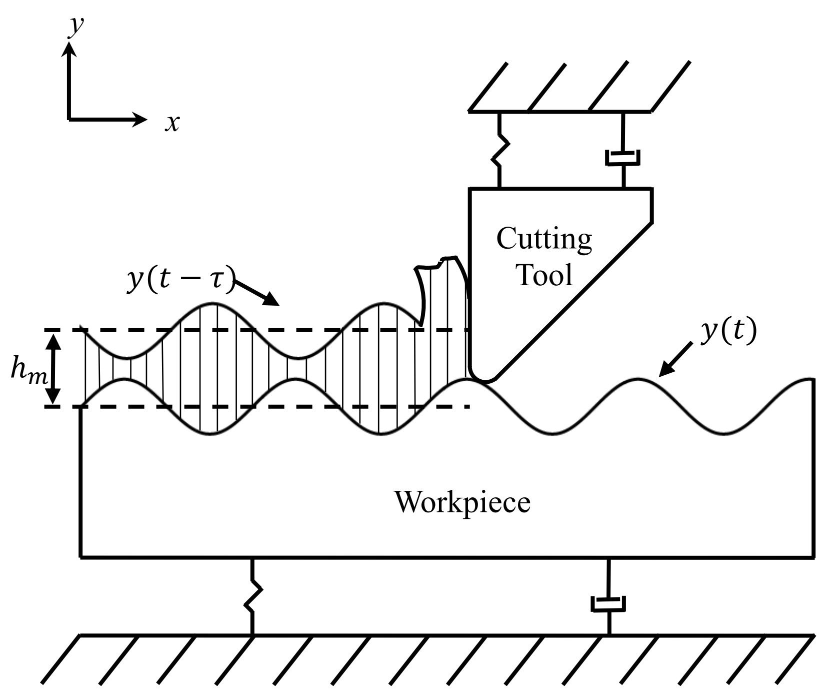

Figure 2.2: Variation in chip thickness when the relative vibrations between the cutting tool and workpiece between two successive passes of the cutting tool are out-of-phase.

Research by Tobias, Tlusty, and Merritt [12-14] revealed regeneration of surface waviness (or the regenerative effect) as a primary chatter mechanism. This discovery led to the development of an analytical model for predicting the occurrence of chatter based on the stability lobe diagram (SLD). The stability lobe diagram distinguishes regions of stable and unstable cutting conditions with respect to chip width (feedback system gain), b_{lim}, and spindle speed (forcing frequency), Ω. Generation of these diagrams requires pre-process knowledge of the system dynamics (mass, stiffness, and damping) as well as a number of process parameters including radial immersion, cutting force coefficients, and tool geometry. A representative example of a SLD with designated stable and unstable regions is given in Figure 2.3.

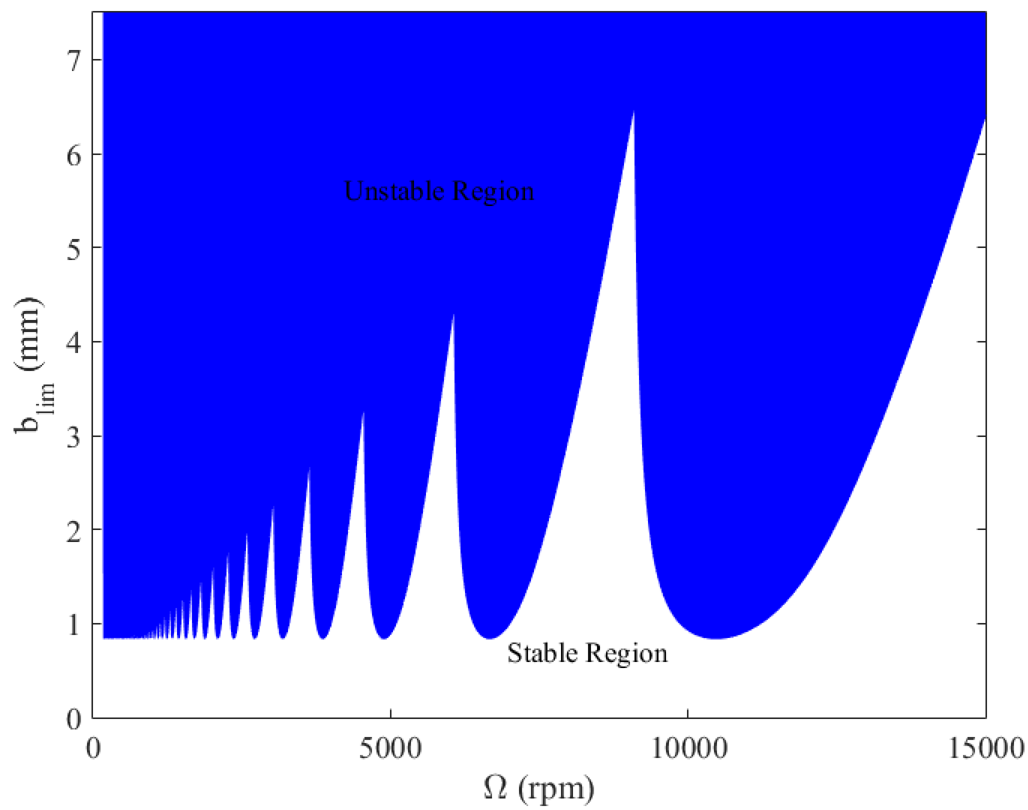

Figure 2.3: Representative stability lobe diagram detailing stable and unstable chip width-spindle speed combinations.

As the stability lobe diagram illustrates, stable machining conditions at increased allowable chip widths may be obtained by selecting from the high spindle speed range where the stable zones are wider. These stable regions are shown to diminish at the low spindle speed range where the stability lobes are closely spaced. However, in early research efforts [15-18] it was noticed that at low cutting speeds stable machining conditions could be obtained at significantly higher chip widths than the stability lobe diagram predicted. This low cutting speed phenomenon, which was termed "process damping", is of particular interest for difficult-to-machine materials due to the prohibitive tool wear which occurs at high cutting speeds. The process damping effect is described as an energy dissipation mechanism which is theorized to occur due to interference between the cutting tool clearance face and machined surface during relative vibrations of the tool and workpiece. For a system with fixed dynamics, process damping increases as cutting speed (spindle speed) decreases because undulations left on the machined surface are more closely spaced resulting in larger slopes. This, in turn, leads to larger interference and increased energy dissipation. An iterative, analytical machining stability model which includes process damping has been detailed in [19] allowing for the generation of stability lobe diagrams that capture the increased allowed chip width at low cutting speeds. As an illustrative example, a stability lobe diagram which includes the analytical process damping model is given in Figure 2.4.

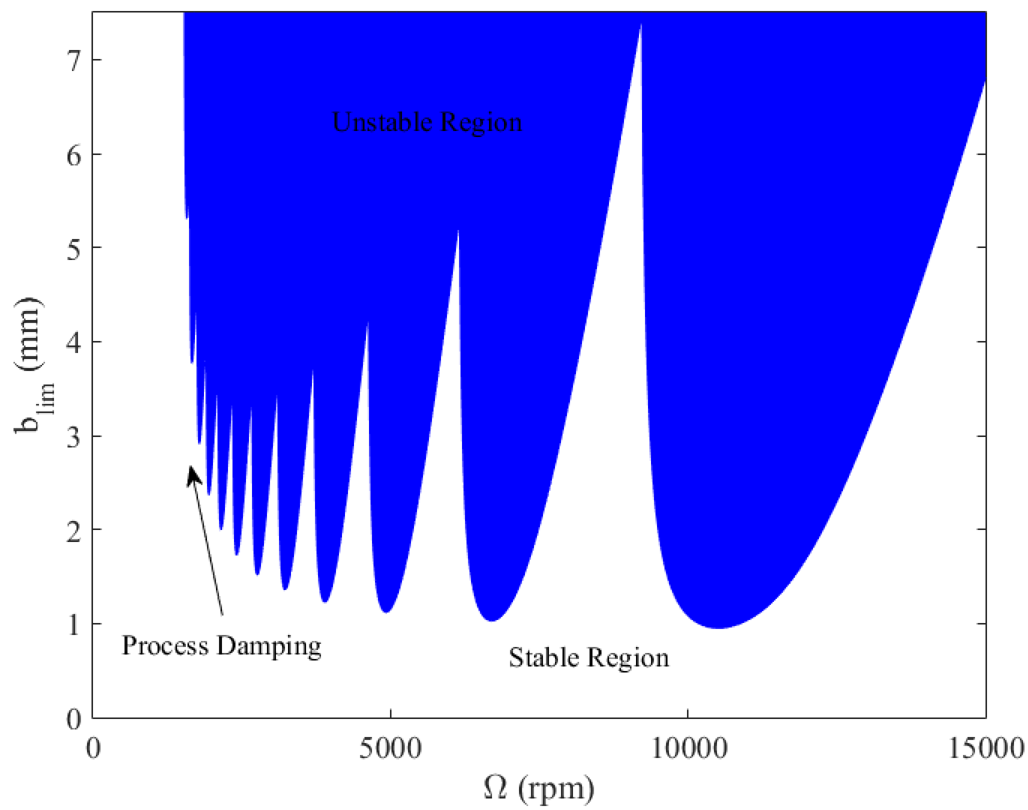

Figure 2.4: Representative stability lobe diagram including analytical process damping model.

For interrupted cutting processes, such as milling and interrupted turning, the stability analysis is complicated by the periodic nature of the cutting force and the time dependence of its direction. Strictly speaking, the stability boundary cannot be expressed in closed form. However, a number of quasi-analytical stability analyses have been proposed in the literature. Tlusty proposed a solution which assumes an average tooth angle, and therefore, an average force direction [20-22]. Another approach by Altintas and Budak uses a Fourier series expansion of the periodic cutting forces [23]. Typically, only the first term of the Fourier series is used to represent the cutting force, and for this reason, it is commonly referred to in the literature as the zero order approximation (ZOA). It has been demonstrated that inclusion of additional terms in the Fourier series expansion enhances the accuracy of the predicted stability boundary [24]. In [25] Insperger *et al.* propose two solution methods: (1) a combination of an exact solution of the tool's free vibration response when the cutting edge is not engaged in the cut and an approximate solution for the vibration of the tool while engaged in the cut using time finite element analysis (TFEA) and (2) a method referred to as semi-discretization which transforms the time delayed differential milling equations into a series of autonomous ordinary differential equations (ODEs) for which the solutions are known.

2.2 Compliant Workpiece Machining

Early work to develop tool path strategies for machining parts with thin, flexible geometric features relied primarily on the inherent stiffness of bulk workpiece material. Upwards of 80% of this bulk material may be removed to achieve the final workpiece geometry. Through the use of relieved shank tooling and the concept of "machine where the part is stiffest", efficient methods for manufacturing thin, aluminum parts via high speed machining were developed by Smith *et al.* [1-3].

The mechanical properties of difficult-to-machine materials, such as titanium and nickel alloys, make them ideal candidates for compliant, thin-walled structures. However, the same machining methodology that has been applied to aluminum is often not appropriate for these materials due to the high material costs and cutting speed (spindle speed) limitations imposed by tool wear [5]. Near net shape techniques have been used to manufacture compliant structures composed of hard-to-machine materials, but these techniques are often unable to achieve the required dimensional tolerances. Due to the inherent compliance of the preforms, stable machining is difficult to achieve. Chatter avoidance, through prediction of stable machining parameters, and chatter reduction, through mechanical manipulation of the structure's dynamics, is critical for the finish machining of such compliant workpieces.

Achieving stable machining of compliant workpieces is complicated by four factors: (1) low structural damping (i.e., in some cases $\ll 1\%$), (2) nonlinear behavior at low radial immersion, (3) continuous variation of workpiece dynamic response as material is removed, and (4) spatially dependent workpiece dynamics.

In [26] Smith *et al.* demonstrated a strategy where sacrificial stiffening elements were added to a structural preform to increase the minimum stiffness such that stable finish machining was achievable while minimizing the volume of material to be removed. Aoyama *et al.* [27] presents a fixturing method, which utilizes low melting temperature alloy and support pins, to suppress workpiece deformation during machining. The method of dynamic absorption is demonstrated in [28] by applying a viscoelastic material (neoprene) and tuned masses to a thin-walled structure to dampen the vibration response across a wide bandwidth of frequencies.

Others have used techniques that may be categorized as chatter suppression (i.e., active modulation of critical stability parameters in situ). In [29] Ismail *et al.* used a combination of pre-process feed rate scheduling and in situ spindle speed variation to suppress chatter during five-axis machining of turbine blades. Shamoto *et al.* [30] implemented opposing milling spindles to machine thin plates on both sides simultaneously at different spindle speeds. Using a finite element approach, the dynamic interaction of the spindle-tool and workpiece were analyzed in [31], and it was determined that it is necessary to regulate spindle speed to achieve optimal chatter free machining conditions when milling thin-walled structures.

Many of the chatter avoidance techniques focus on predicting the continuous change of the thin workpiece dynamics as material is removed. The predicted dynamics are then used in conjunction with typical stability analyses to generate stability lobe diagrams that are material removal dependent. In studies such as those reported in [32-34], the three-dimensional stability lobe diagram is proposed where the third dimension is either the steps of the machining process or the tool position. The flexible workpiece dynamics are predicted using finite element analysis (FEA) or the structural modification technique [35, 36] that uses the frequency response functions (FRF) of the original system and the dynamic structural matrix of the modifying system to predict the FRFs of the modified system.

2.3 Low Radial Immersion Milling

Near net shape preforms must undergo finish milling operations to achieve the required dimensional accuracy and surface finish. Because finish milling operations inherently present low radial immersion conditions, it is necessary to discuss the stability of such operations for full coverage on the topic of milling stability. The traditional stability theory [23] presented in 2.1, which divides the domain of spindle speed and chip width into stable and unstable regions, provides accurate predictions of locally optimal spindle speeds for high radial immersion milling cuts. However, the assumptions of the traditional stability analysis become invalid at low radial immersion [37]. Davies *et al.*

asserted that at low radial immersion the highly interrupted tool-workpiece engagement causes periodic driving terms (i.e. impact dynamics) and that the tool-workpiece engagement time is strongly influenced by tool and/or workpiece deflections.

Using once-per-revolution sampling (i.e. Poincarè sectioning) techniques, Davies *et al.* observed two different types of chatter behavior at low radial immersion [37]. The first type was the traditional quasi-periodic chatter behavior which is associated with secondary Hopf bifurcations occurring in systems governed by time-delayed differential equations. This expected result manifested as an elliptical arrangement of once-per-revolution sampled points in the tool's x-y deflection (i.e., Poincarè section) which was measured perpendicular to the tool's axis of rotation using a spindle-mounted capacitance probe array; see Figure 2.5(a). The second type of chatter behavior (flip bifurcation) was observed as a cluster of three distinct points in the Poincarè section indicating that the tool motion repeats every three revolutions; see Figure 2.5(b).

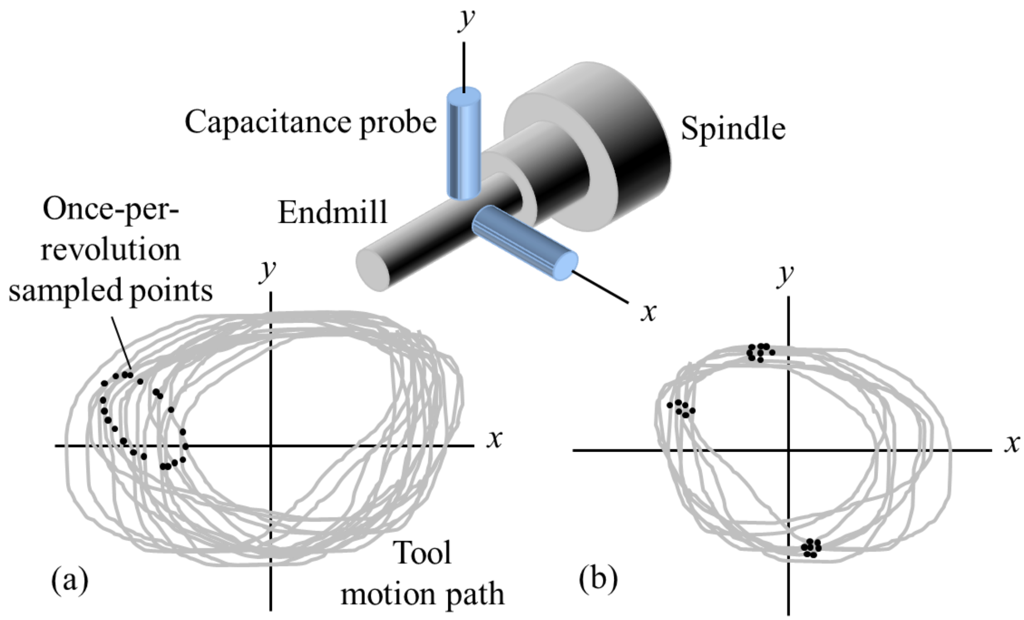

Figure 2.5: Poincarè sectioning (i.e., once-per-revolution sampling) of tool motion manifesting as both (a) secondary Hopf instability and (b) period-3 instability [38].

In [7] an approximate time domain solution is presented wherein the stability of low radial immersion milling is calculated using a “two-stage map.” During the first stage the non-cutting tool motions are governed by the analytical solution for damped, free vibration. In the second stage the cutting tool motions are approximated by modifying the tool momentum using an impulsive force. Later, in [8], Davies *et al.* present the first analytical stability boundary for low radial immersion (i.e., highly interrupted) milling by modeling the system as a “kicked harmonic oscillator” with a time delay. The practical takeaway from this theory is the prediction of additional stable spindle speeds when the spindle period is an odd integer multiple of one-half the period of the tool.

As an alternative to the analytical stability analysis, time domain simulation has been applied to low radial immersion milling. In [39] Campomanes *et al.* uses the actual trochoidal tooth path to improve the simulation of low radial immersion milling. Chatter detection is facilitated by calculating a "nondimensional chatter coefficient" which is the ratio of the maximum uncut chip thickness during a time domain simulation with flexible dynamics and the maximum uncut chip thickness during a time domain simulation with rigid dynamics. They noted that their time domain simulation confirmed the additional stable spindle speeds presented by Davies *et al.* and that the inclusion of edge forces in the model resulted in both an increase and decrease in the stability limit. In [40] Zhao *et al.* use time domain simulation to verify secondary Hopf bifurcations and period-2 (i.e., period doubling) bifurcations using bifurcations diagrams which plot tool deflections in a single independent coordinate versus chip width.

The semi-discretization, time finite element analysis, and multi-frequency methods were also developed to produce milling stability charts that predicted the two types of instability [24, 25, 41, 42]. In [43] , Govekar *et al.* use the semi-discretization method to predict both quasi-periodic and periodic chatter during low radial immersion milling. They show that secondary Hopf lobes are open curves distributed along the spindle speed axis while flip bifurcations are closed curves within the secondary Hopf lobes as shown in Figure 2.6. More experimental results showing period-2, period-3, period-4, and combined Hopf and period-2 chatter are shown in [9] for a two degree of freedom system.

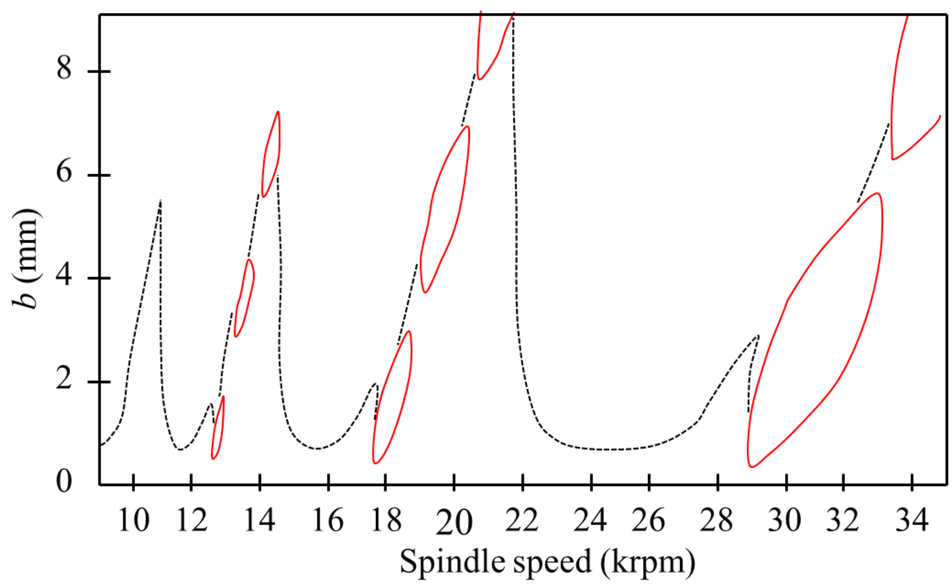

Figure 2.6: Stability lobe diagram with secondary Hopf (dashed) and period-2 (solid) stability boundary redrawn from [43].

The nonlinear aspects of milling behavior at low radial immersion have been investigated extensively in [44-46]. In [47], Zatarain *et al.* show that the closed period-2 curves vary in shape and size depending upon the helix angle of the cutting tool. Additionally, islands of period-2 instability appear that are detached from the secondary Hopf lobes when tool helix angle is considered. This work was extended in [48] to show that horizontal boundary lines along the chip width axis of the stability chart, which are spaced by the axial pitch of the cutter, separate the unstable islands. From the mathematical perspective, these values of chip width (equal to integer multiples of the axis pitch of the cutter) make the equations of motion autonomous, delayed differential equations for which period-2 instability cannot occur. The helix angle effect has also been investigated using time finite element analysis [49].

CHAPTER 3: CUTTING FORCE MODELING

The modeling of machining processes, which has been an important research topic for nearly a century, is motivated by the requirements of machine tool users and builders alike. The machine tool user aims to reliably predict key process outputs, such as cutting forces, which affect workpiece surface quality, geometrical accuracy, and process stability. From the builder's perspective, the cutting forces represent a critical design metric because they dictate the required spindle power and torque as well as the required rigidity of the machine tool's structural loop. In machining process simulations and optimizations, cutting force modeling occurs at an early stage and thereby strongly affects the accuracy of the results.

There are three approaches to cutting force modeling which are prevalent throughout the literature: analytical, numerical, and mechanistic [50, 51]. The analytical models relate cutting forces to a number of process variables (i.e., chip load, cutting speed, and cut geometry) and mechanical aspects such as shear angle, material properties, and friction. Early work using this approach was detailed by Merchant in [52] and by Amarego and Brown in [53]. Increasing computational power has led to advancements in the field of research in numerical modeling where much focus is placed on determination of undeformed chip thickness and tool geometry to study their interaction [54].

The mechanistic force models assume that the instantaneous cutting forces are proportional to the uncut chip area through an empirically-derived coefficient [50]. Early works in mechanistic force modeling for milling operations was reported by Martellotti [55], Koenigsberger et al. [56], and Sabberwal [57]. To date the literature highlights two mechanistic force models. The first relates instantaneous cutting forces and uncut chip areas to a single lumped, empirical coefficient which is commonly referred to as the specific force coefficient and often denoted as K_s. This single coefficient aims to capture the effect of both cutting (i.e. shearing) and ploughing (i.e. friction at the cutting edge) which occurs during chip formation. The ease of implementation and useful predictive capabilities provided by this simple model has resulted in its widespread application in industry and research. The second, published in later works by Budak et al. [58], extends the mechanistic cutting force model to include separate empirical coefficients to capture the chip formation mechanics of shearing and ploughing.

In [59] and [60] a method for the identification of the empirical coefficients, commonly referred to as specific force coefficients, is presented. The procedure proposes that a linear regression of measured cutting forces be performed over a range of feed per tooth values while holding other process parameters such as cutting speed and cut geometry constant. This method, which requires numerous cutting tests to perform the linear regression analysis, has proven to provide accurate results which are specific to the cutting tool geometry and workpiece material combination. However, the regression analysis assumes that cutting forces are linearly dependent upon feed per tooth and independent of other machining parameters such as cutting speed and feed, cut geometry, and cut direction (i.e., up milling/down milling). Other methods, such as those presented in [61, 62], use nonlinear optimization methods to perform a least squares fit of simulated cutting forces to measured cutting forces. This approach requires measurements from a single cutting test and results in specific force coefficients which are specific to the chosen machining parameters. As such, the specific force coefficients may be considered as a function of not only the cutting tool geometry and workpiece material, but machining parameters such as cutting speed and feed, cut geometry, and cut direction (i.e., up milling/down milling). The nonlinear optimization method provides a tool for studying the effects of these machining parameters on dynamic cutting forces.

3.1 The Mechanistic Approach

The mechanistic force models are based on the assumption that the instantaneous cutting force is proportional to the cross sectional area of the uncut chip through a number of empirically determined specific force coefficients. This method of cutting force modeling assumes that the instantaneous cutting forces are independent of other machining parameters such as cutting speed and feed, cut geometry, and cut direction (i.e., up milling/down milling). Although this assumption provides a reasonable degree of accuracy for milling stability prediction through lobe diagrams [59], it has been shown in a number of studies [62] that cutting forces are dependent upon cutting speed and feed. The mechanistic force model used in this study includes six empirically determined specific force coefficients, and the instantaneous cutting forces in the tangential, F_t, normal, F_n, and axial, F_a, directions are given in equations (3.1) - (3.3) as:

$$F_t = k_{tc}bh + k_{te}b \tag{3.1}$$

$$F_n = k_{nc}bh + k_{ne}b \tag{3.2}$$

$$F_a = k_{ac}bh + k_{ae}b \tag{3.3}$$

where b is the chip width (i.e., axial depth of cut) and h is the instantaneous chip thickness, which is based on the circular tooth path approximation; see equation (3.4). It is dependent on the feed per tooth, f_t, as given by:

$$h = f_t \sin(\phi) \tag{3.4}$$

where ϕ is the cutter rotation angle. Each component of the instantaneous cutting force includes two specific force coefficients, each of which is associated with separate aspects of chip formation. The coefficients k_{tc}, k_{nc}, and k_{ac} are correlated with cutting or shearing, and the edge coefficients k_{te}, k_{ne}, and k_{ae} are correlated with rubbing or ploughing. The edge coefficients affect the instantaneous cutting force proportionally through the chip width, but are independent of the instantaneous chip thickness. They provide a non-zero force value even as the chip thickness approaches zero.

3.2 Dynamic Compensation of Measured Cutting Forces

Accurate measurement of cutting forces is crucial for machining process simulation and for evaluation of cutting tool geometries and concepts [63]. The most common method of cutting force measurement found in the literature utilizes commercial piezoelectric dynamometers. Because these dynamometers are not infinitely rigid, they may be considered as a dynamic system with a characteristic frequency response which defines the measurement bandwidth of the instrument. As the tooth passing frequency and harmonics (integer multiples) begin to approach the resonance frequencies of the dynamometer, unwanted frequency content is superimposed on the cutting force signal. The resulting measured forces suffer from poor accuracy, and, therefore, the process of cutting force coefficient determination at high tooth passing frequencies (i.e., high spindle speeds) is complicated.

In this study a compensation technique based on inverse FRF filtering was utilized to truncate the unwanted frequency content in the measured cutting forces. The filter is constructed by inverting the measured force-to-force FRF of the dynamometer [63], also commonly referred to as the transmissibility.

$$H(\omega) = \frac{F_{out}(\omega)}{F_{in}(\omega)} \tag{3.5}$$

The dynamometer force-to-force FRF is a complex-valued ratio of the input force, $F_{in}(\omega)$, and the output force from the dynamometer, $F_{out}(\omega)$, in the frequency domain. Ideally, there would be no unwanted frequency content added to the measured forces. In this case the magnitude of the dynamometer FRF would be equal to unity and the phase would be equal to zero for all frequencies. Because the dynamometer/workpiece system has finite mass, stiffness, and damping, the magnitude and phase of the measured cutting forces depart from their ideal values.

In [64], Castro et al. use a three by three FRF matrix, referred to as the dynamometer's transmissibility matrix, which contains three direct FRFs (i.e., the dynamometer force output is in the same xyz component direction as the applied force) and six cross FRFs (i.e., the dynamometer force output is in the xyz component directions orthogonal to the applied force). The inclusion of the cross FRFs in the inverse filtering technique serves to truncate frequency content from the measured cutting forces due to crosstalk in the dynamometer's xyz component directions. In this study the effect of crosstalk (i.e., cross FRFs) was considered to be negligible.

The success of the inverse filtering method is primarily limited by the accuracy and bandwidth of the measured dynamometer/workpiece system FRF and by the fitting of the measured FRF to compute modal parameters which are used to mathematically reconstruct the compensation filter. Typically, the measurement accuracy is assessed by computing the coherence, which serves as a quality index, between the input force and the dynamometer output. Aside from the cases where coherence is poor in close proximity to anti-resonance frequencies, a coherence value of 0.90 was selected as the threshold value for fitting the measured FRF; see Figure 3.1.

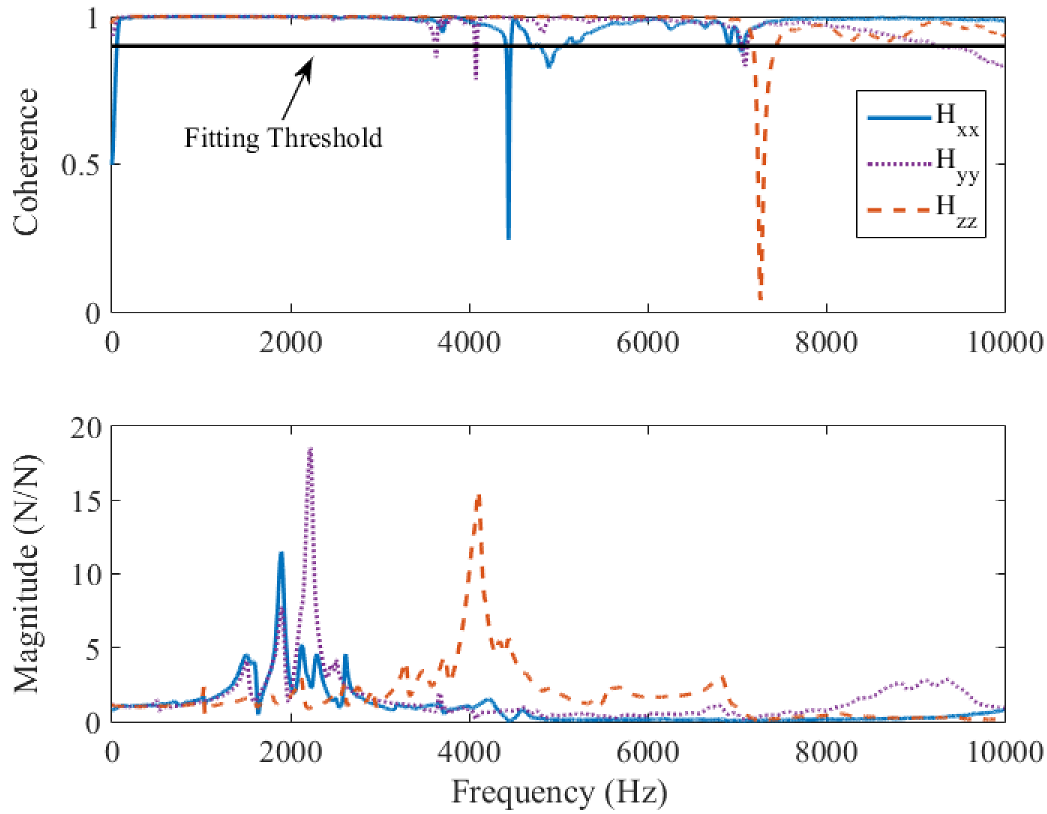

Figure 3.1: Example measurement results of a dynamometer force-to-force FRF in the xyz directions including the coherence and magnitude.

Fitting of the measured FRF, which is used to compute the system's modal parameters, is completed using a two-stage process which includes: (1) the peaking picking method and (2) a nonlinear optimization. The peak picking method, detailed by Schmitz in [59], is used to perform a preliminary fit to the FRF. Because of modal truncation, where modes are present outside of the measurement bandwidth and contribute to the dynamic response of the dynamometer but cannot be included in the fit, the accuracy of the FRF fit suffers. To limit this effect and improve the accuracy of the fit, a nonlinear optimization of the FRF's magnitude is performed. Example results from the FRF fitting process are shown in Figure 3.2. A detailed description of the two-stage fitting process is provided in section 4.2.

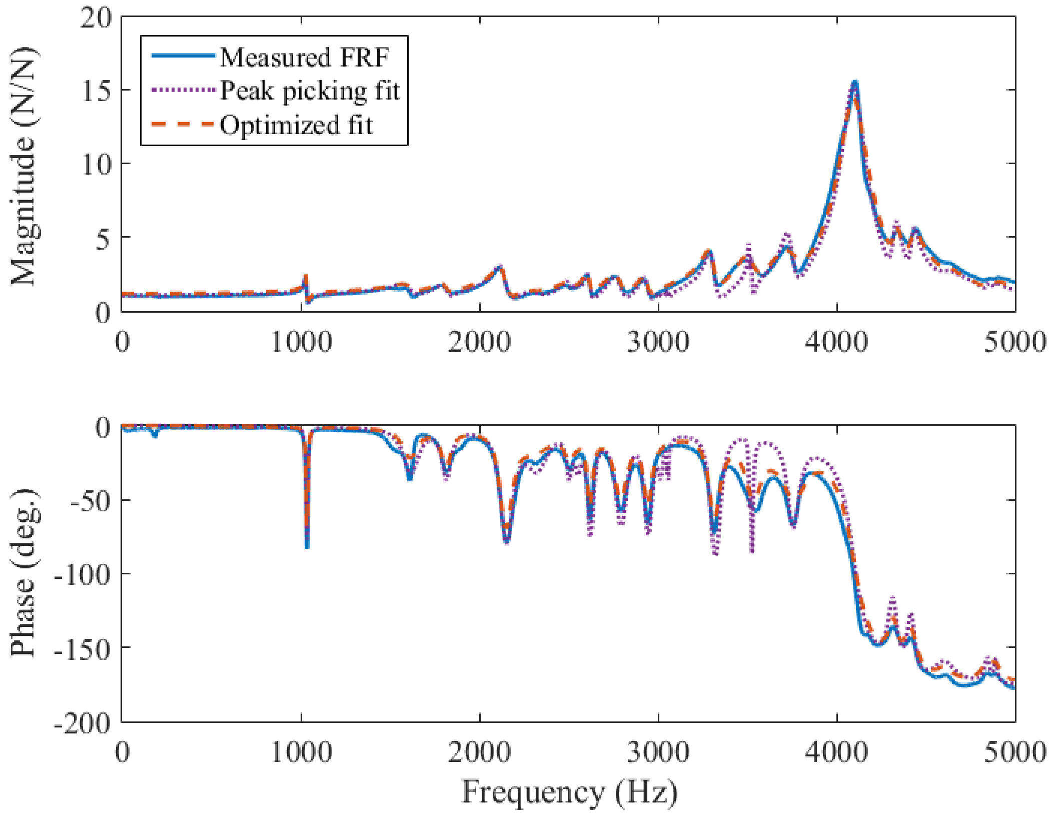

Figure 3.2: Example results from the two-stage modal fit of a measured dynamometer FRF.

The magnitude of the inverted, dynamometer FRF decays to near-zero at high frequencies; see Figure 3.1. Applying a filter that is simply the inversion of the dynamometer FRF will lead to amplification of high frequency measurement noise as shown in Figure 3.3(a). This is avoided by convolving the inverted dynamometer FRF with a fourth-order lowpass filter; see Figure 3.3b. The cutoff frequency of the lowpass filter is selected such that the magnitude response of the final, inverse FRF filter is near unity at high frequencies. The resulting inverse FRF filter, shown in Figure 3.3c, simultaneously amplifies and truncates the relevant frequency components, which are distorted by the dynamic response of the dynamometer, while preserving the high frequency components of the measured cutting forces. Preservation of the high frequency components of the measured cutting forces is crucial for evaluating the stability of milling operations.

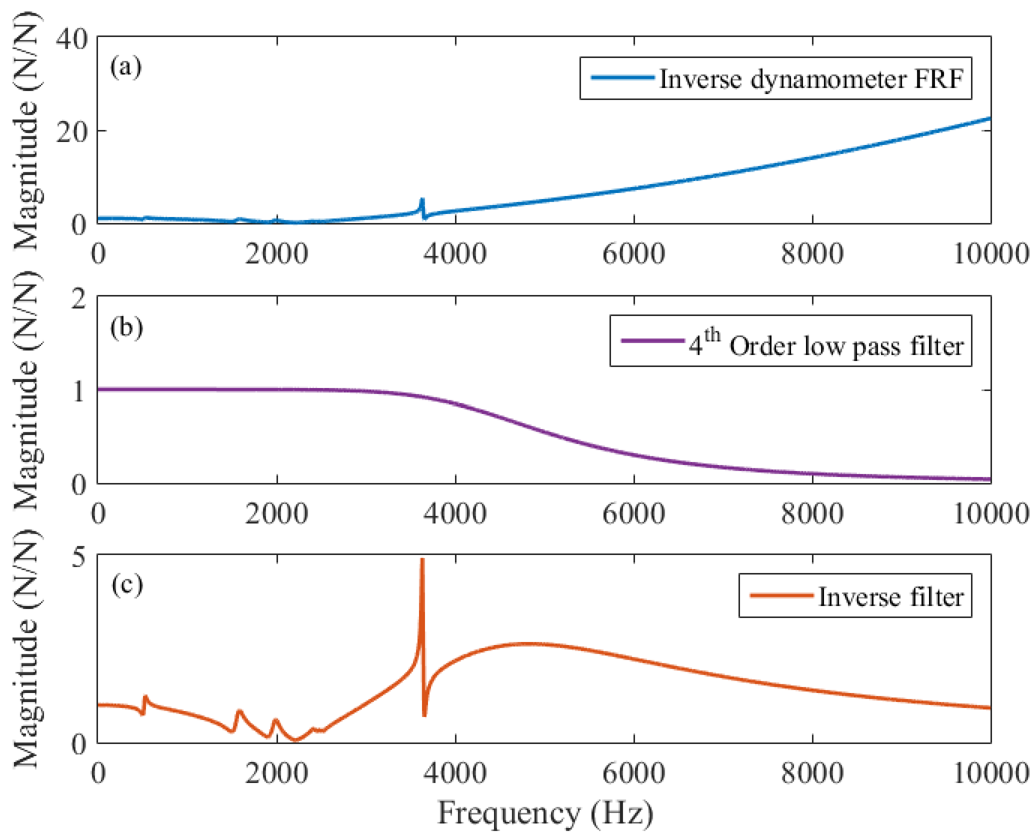

Figure 3.3: Magnitude response of (a) the inverted, measured dynamometer FRF, (b) second order lowpass filter, and (c) inverse FRF filter.

Typical results from the dynamic compensation technique are shown in Figure 3.4. The measured cutting forces contain significant dynamic distortion as evidenced by the amplification of the frequency content in the measured cutting forces near 1866 Hz. This frequency corresponds to the largest magnitude of the x-direction dynamometer force-to-force FRF as shown in Figure 3.1. The compensated cutting forces exhibit frequency content at the tooth passing frequency, f_t, which occurs at $266.5\,Hz$ for the milling operation using a 2 flute endmill with a spindle speed of $8\,krpm$. Frequency content is also observed at harmonics of the tooth passing frequency as well as the runout frequency which occurs at one-half of the tooth passing frequency.

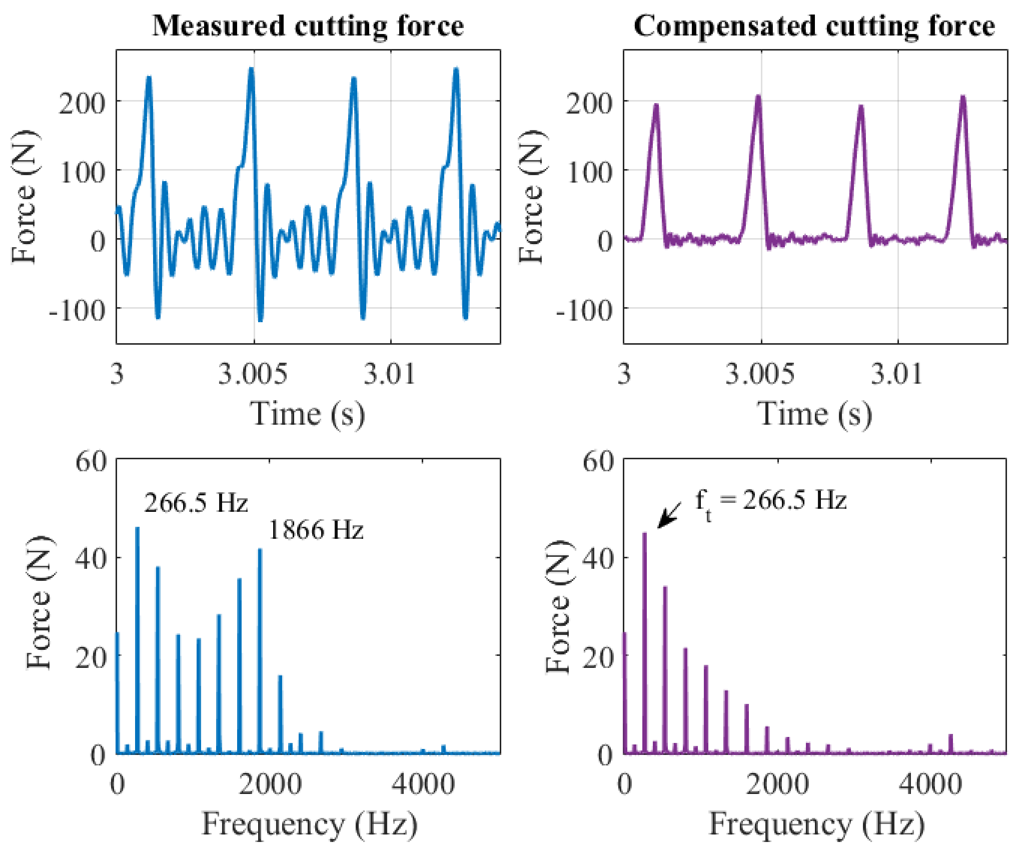

Figure 3.4: Example results of the dynamic compensation on the time domain (top) and frequency domain (bottom) cutting forces.

Because the instantaneous force, nonlinear optimization method simulates cutting forces in the time domain as a function of cutter rotation angle, the x, y, and z component forces have a phase relationship. Introduction of a relative phase shift, due to the response of the inverted dynamometer FRF, to the measured x, y, and z component forces is undesirable as it will lead to errors in the instantaneous force, nonlinear optimization method results. Typical results from the dynamic compensation technique are shown in Figure 3.5 for the x, y, and z component forces in the time domain. No phase shift of the component forces relative to one another is observed.

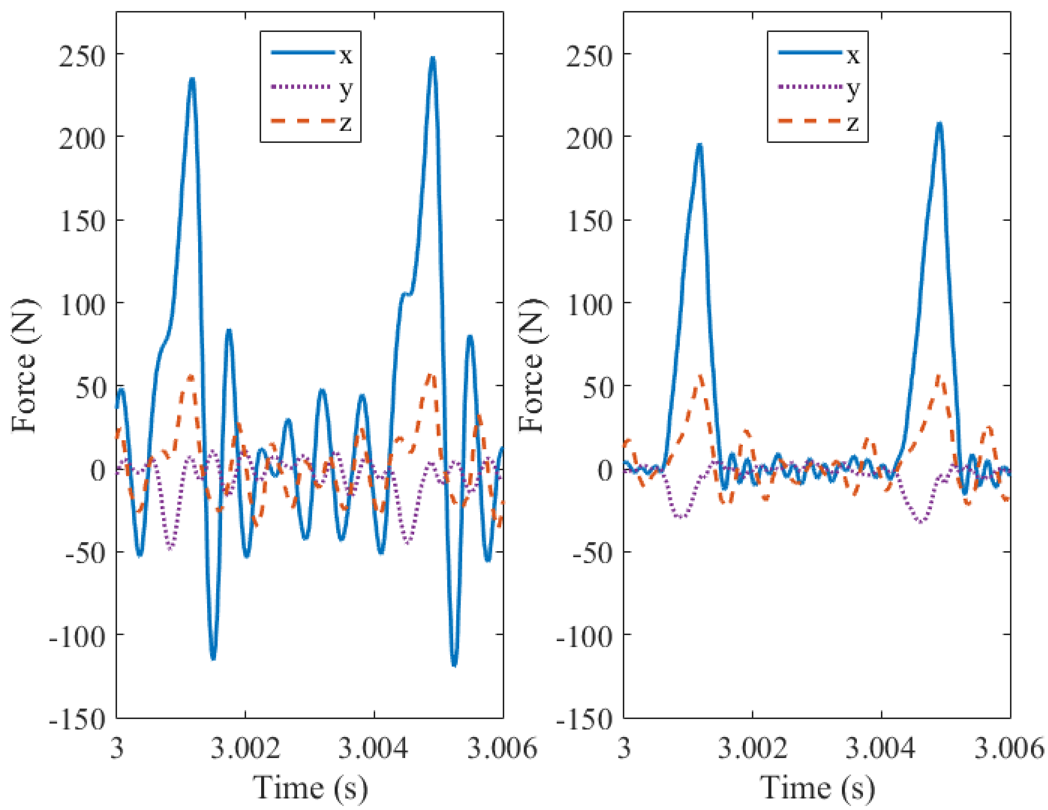

Figure 3.5: Example results of the dynamic compensation on the x,y, and z components of the measured cutting forces.

3.3 Cutting Force Coefficient Determination

The following sections detail the two methods whereby the cutting force coefficients of the mechanistic force model were determined.

3.3.1 Average Force, Linear Regression Method

The six specific force coefficients were determined through linear regression analysis using the average cutting forces measured during a series of cutting tests which were performed over a range of feed per tooth values while holding other milling parameters (i.e., axial depth of cut, spindle speed, and radial immersion) constant. Projecting the tangential, normal, and axial cutting force components into a fixed reference frame (i.e., x, y, and z), shown in Figure 3.6, and averaging over one cutter revolution yields the following expressions for mean cutting force per revolution.

$$\bar{F}_x = \left\{\frac{N_t b f_t}{8\pi}\left[-k_{tc}\cos(2\phi) + k_{nc}(2\phi - \sin(2\phi))\right] + \frac{N_t b}{2\pi}\left[k_{te}\sin(\phi) - k_{ne}\cos(\phi)\right]\right\}_{\phi_s}^{\phi_e} \quad (3.6)$$

$$\bar{F}_y = \left\{\frac{N_t b f_t}{8\pi}\left[k_{tc}(2\phi - \sin(2\phi)) + k_{nc}\cos(2\phi)\right] - \frac{N_t b}{2\pi}\left[k_{te}\cos(\phi) + k_{ne}\sin(\phi)\right]\right\}_{\phi_s}^{\phi_e} \quad (3.7)$$

$$\bar{F}_z = \left\{\frac{N_t b}{2\pi}\left[k_{ac} f_t \cos(\phi) - k_{ae}\phi\right]\right\}_{\phi_s}^{\phi_e} \quad (3.8)$$

where $N_t$is the number of teeth on the cutter, and $\phi_s$and $\phi_e$are the start and exit angles of the cutter teeth, respectively.

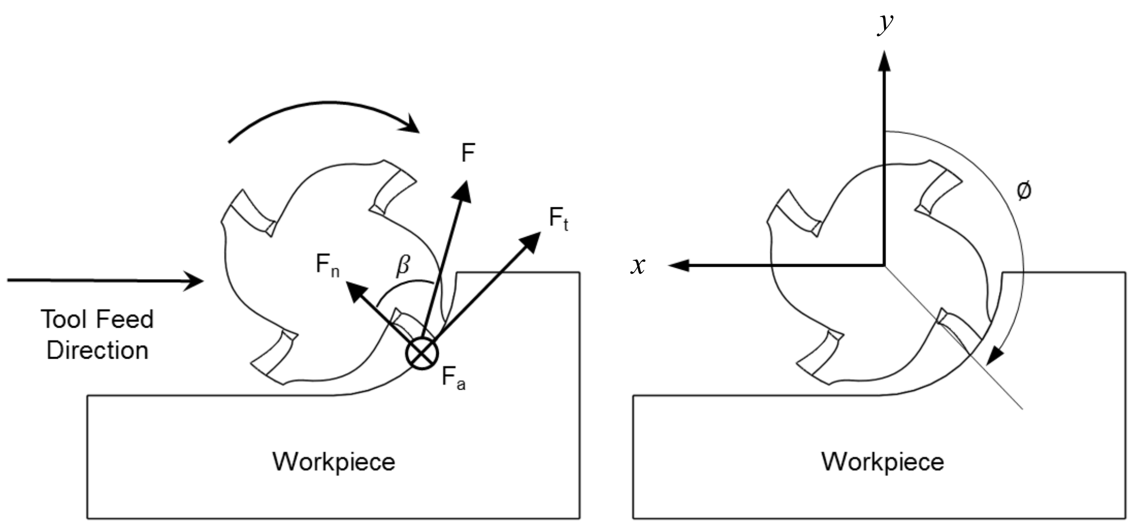

Figure 3.6: Force components and fixed reference frame for the average force, linear regression method. A down milling configuration is shown with a helical endmill.

In most cases, 100% radial immersion (i.e., slotting) cutting tests are selected, where $\phi_s = 0°$ and $\phi_e = 180°$, so that the mean cutting force per revolution expressions reduce to:

$$\bar{F}_x = \frac{N_t b k_{nc}}{4} f_t + \frac{N_t b k_{ne}}{\pi} \tag{3.9}$$

$$\bar{F}_y = \frac{N_t b k_{tc}}{4} f_t + \frac{N_t b k_{te}}{\pi} \tag{3.10}$$

$$\bar{F}_z = -\frac{N_t b k_{ac}}{\pi} f_t - \frac{N_t b k_{ae}}{2} \tag{3.11}$$

These expressions are given in slope-intercept form, and a linear regression over feed per tooth may be performed to determine the cutting force coefficients. The slope, a_{1j}, and intercept, a_{0j}, of the linear regression are given as:

$$a_{1j} = \frac{n\sum_{i=1}^{n} f_{t,i}\bar{F}_{j,i} - \sum_{i=1}^{n} f_{t,i}\sum_{i=1}^{n}\bar{F}_{j,i}}{n\sum_{i=1}^{n} f_{t,i}^{2} - \left(\sum_{i=1}^{n} f_{t,i}\right)^{2}} \tag{3.12}$$

$$a_{0j} = \frac{1}{n}\sum_{i=1}^{n}\bar{F}_{j,i} - a_{1j}\frac{1}{n}\sum_{i=1}^{n} f_{t,i} \tag{3.13}$$

where j indicates the force component direction (i.e., x, y, or z) and n is the number of $(f_{t,i}, \bar{F}_{j,i})$ data pairs. Once the slope and intercept are determined the specific coefficients can be calculated using equations (3.14) - (3.16). Finally, the specific force coefficients are given as:

$$k_{tc} = \frac{4a_{1y}}{N_t b} \quad k_{te} = \frac{\pi \cdot a_{0y}}{N_t b} \tag{3.14}$$

$$k_{nc} = \frac{4a_{1x}}{N_t b} \quad k_{ne} = \frac{\pi \cdot a_{0x}}{N_t b} \tag{3.15}$$

$$k_{ac} = -\frac{\pi \cdot a_{1z}}{N_t b} \quad k_{ae} = -\frac{2a_{0y}}{N_t b} \tag{3.16}$$

It may be observed that the specific force coefficients are functions of the slope and y-intercept of the linear regression over feed per tooth. The derivation of the specific cutting force coefficients for the general case of arbitrary radial immersion is given in APPENDIX A:.

This method of determining the specific cutting force coefficients assumes that the instantaneous cutting forces are linearly related to feed per tooth and independent of other milling parameters such as radial immersion and spindle speed.

3.3.2 Instantaneous Force, Nonlinear Optimization Method

Alternatively, the cutting force coefficients were determined using an instantaneous force, nonlinear optimization method which solves a nonlinear, least squares curve fitting problem and takes into account the user-defined lower and upper bounds on the decision variables (i.e., specific force coefficients and flute-to-flute runout). The optimization routine, which uses a trust-region-reflective least squares algorithm, equates cutting forces simulated in the time domain with experimentally measured cutting forces at each discrete time step.

The time domain simulation calculates the cutting forces at each small time step, dt, which is defined in the simulation as:

$$dt = \frac{1}{f_s} \tag{3.17}$$

where f_s is the sampling frequency of the cutting force measurement. At each incremental time step the instantaneous chip thickness is computed, the cutting force is calculated, the tooth angle, ϕ, is incremented by a small angle, $d\phi$, which is a function of spindle speed and the incremental time step, and the process is repeated for one complete revolution of the cutting tool. The instantaneous chip thickness is determined using the circular tooth path approximation and assuming a rigid tool and workpiece. Additionally, flute-to-flute runout of the cutting tool is incorporated into the instantaneous chip thickness calculation. For a more thorough and robust model, the actual trochoidal tooth path [65, 66], which more accurately models the instantaneous chip thickness at the start and exit of the cut, may be employed. However, in this study the circular tooth path approximation provided adequate accuracy at significantly lower computational cost. Because the instantaneous force, nonlinear optimization method is capable of solving nonlinear curve fitting problems, the mechanistic force model may be modified to include a nonlinear dependence on chip thickness which was presented by Feng et al. [67] for ball endmilling processes.

The tangential, F_t, normal, F_n, and axial, F_a, cutting forces were calculated according to the mechanistic force model defined in section 3.1. In order to represent the simulated forces in the fixed reference frame of the measured cutting forces, a coordinate transformation is performed.

$$\begin{Bmatrix} F_x \\ F_y \\ F_z \end{Bmatrix}_{simulated} = \begin{bmatrix} \cos(\phi) & \sin(\phi) & 0 \\ \sin(\phi) & -\cos(\phi) & 0 \\ 0 & 0 & 1 \end{bmatrix} \begin{Bmatrix} F_t \\ F_n \\ F_a \end{Bmatrix}_{simulated} \tag{3.18}$$

where ϕ is the instantaneous cutter rotation angle. Finally, the objective function is given as:

$$f_i(k) = \begin{Bmatrix} F_x \\ F_y \\ F_z \end{Bmatrix}_i^{simulated} - \begin{Bmatrix} F_x \\ F_y \\ F_z \end{Bmatrix}_i^{measured} \tag{3.19}$$

where k is the vector of decision variables, which includes the six specific force coefficients and the flute-to-flute runout of the cutting tool, and $f_i(k)$ is the difference between the x, y, and z components of the instantaneous simulated and measured cutting forces at the ith time step.

Because the time step between each simulated instantaneous cutting force must coincide with the measured cutting forces, the size of the resulting system of equations depends upon the sampling frequency of the measurement and the number of cutting tool revolutions (i.e., number of time steps) included in the optimization. The nonlinear, least squares curve fitting problem is of the form:

$$\min_k \|f(k)\|_2^2 = \min_k (f_1(k)^2 + f_2(k)^2 + \cdots + f_n(k)^2) \tag{3.20}$$

where n is the number of time steps. The curve fitting problem is solved via a trust region reflective algorithm which is based on an interior-reflective Newton approach that is well suited for solving nonlinear optimization problems where the decision variables are bounded by upper and/or lower limits [68].

For the study presented herein, the measured cutting forces were partitioned into 100 individual revolutions of the cutting tool and averaged; see Figure 3.7. It is notable that measured cutting forces exhibit a high degree of repeatability from one revolution of the cutting tool to the next. The measured cutting forces, averaged over 100 revolutions of the cutting tool, were then supplied to the nonlinear optimization function along with a number of relevant process parameters such as number of teeth on the cutting tool, sampling frequency of the measured cutting forces, and initial conditions for the decision variables (i.e., specific force coefficients and flute-to-flute runout).

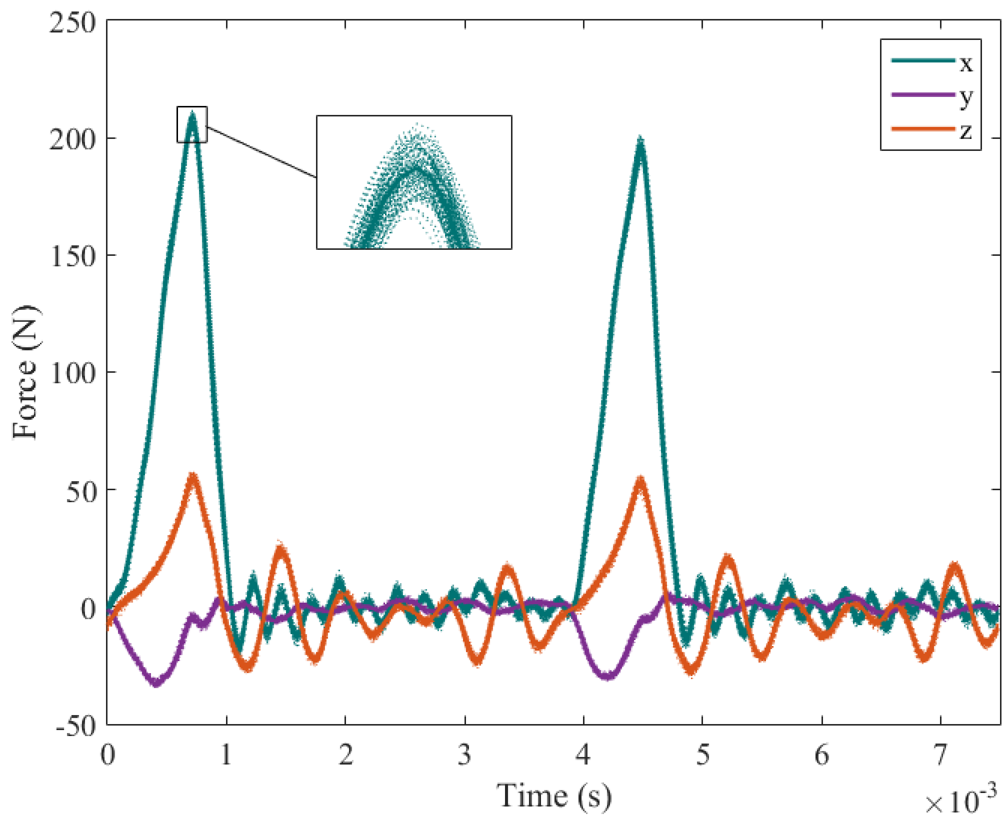

Figure 3.7: Measured cutting forces over 100 revolutions of the cutting tool (dotted line) and their average (solid line) shown for a milling operation using a 2-flute cutting tool.

The optimization function simulates the instantaneous cutting forces in the x, y, and z directions based on the input process parameters. The difference between the simulated and measured cutting forces were then calculated by the objective function given in equation (3.19), and the sum of squares of the differences are evaluated. The evaluation is then scrutinized against an arbitrary, user-defined set of convergence criteria, such as the change in the sum of the squares from one iteration to the next. If it is determined that the convergence criterion are met, the optimization routine ceases; otherwise the decision variables are updated and the process iterates until convergence. Example results of the optimized, simulated cutting forces are shown in Figure 3.8.

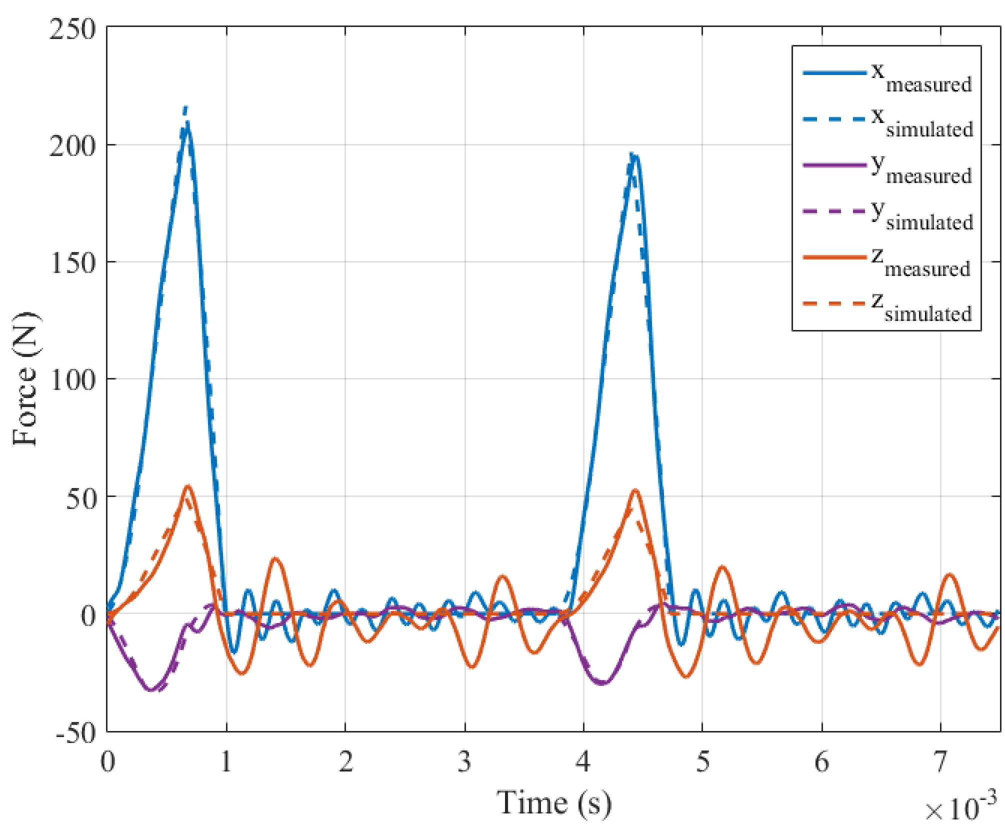

Figure 3.8: Example results from the nonlinear, optimization method including the measured cutting forces and optimized, simulated cutting forces.

3.4 Milling Process Dependent Cutting Force Coefficients

The process parameter dependence of the specific force coefficients was investigated using both the average force, linear regression and instantaneous force, nonlinear optimization methodologies. A series of cutting tests were performed, and the cutting forces were measured. Because the tooth passing frequency was sufficiently high that the measured cutting forces suffered dynamic distortions due to the limited measurement bandwidth of the dynamometer, the measured cutting forces were compensated to truncate the spurious frequency content. The compensated cutting forces were then analyzed using the aforementioned methods and the resulting specific force coefficients were used to make stability predictions based on time domain simulations. A pictorial illustration of the experimental method used in the study is given in Figure 3.9.

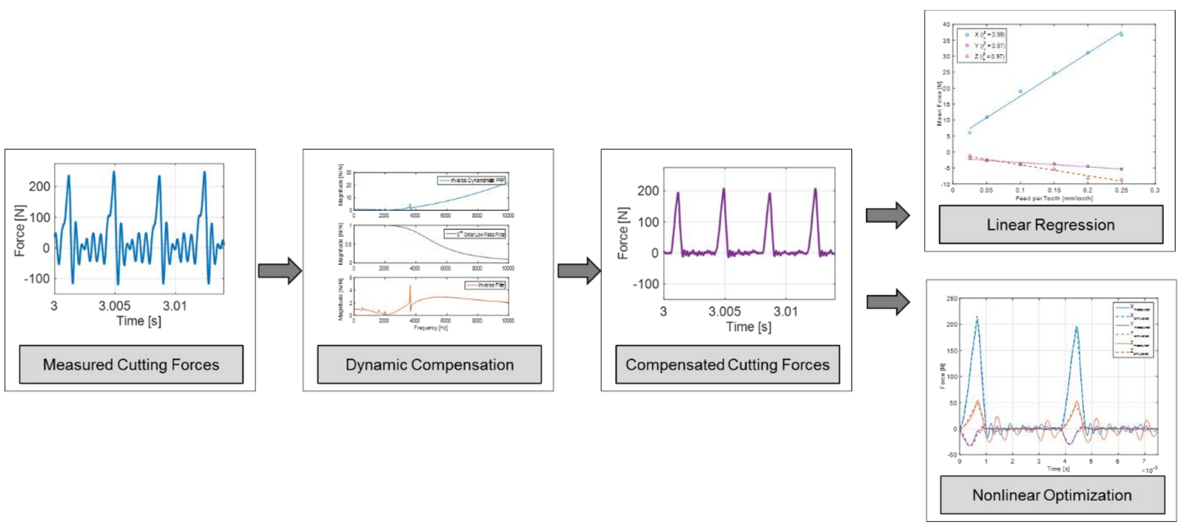

Figure 3.9: Flow diagram detailing the experimental method used in this study.

3.4.1 Experimental Setup

Cutting tests were performed on a LeBlond Makino A55 Plus horizontal milling machine with a maximum spindle speed of 20 $krpm$. The workpiece material, aluminum 6061-T6511 extruded barstock with approximate dimensions of 170 mm × 100mm ×

$38mm$, was rigidly fixed to the three-component cutting force dynamometer (Kistler 9257B) via two M8 socket head cap screws; see Figure 3.10. The dynamometer/workpiece combination was bolted to the machine tool's tombstone via a surface ground steel plate approximately $25\ mm$ in thickness and was carefully aligned to the machine axes using a test indicator. A charge amplifier (Kistler Type 5010), signal analyzer (Data Translation DT9837B), and Spinscope software from Manufacturing Laboratories Incorporated was using for data acquisition.

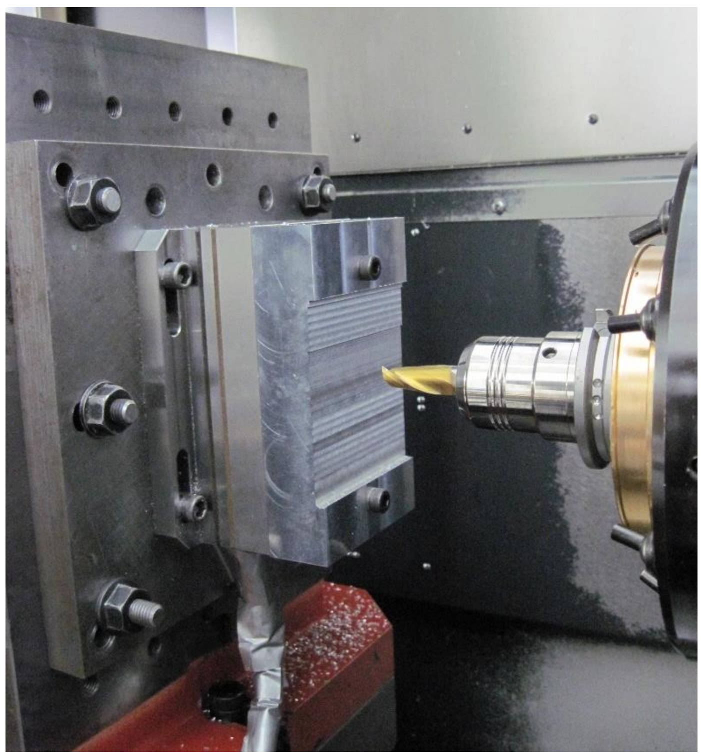

Figure 3.10: Setup for cutting force measurements using a three-axis dynamometer.

The cutting tool used in this study was a 12.7 mm diameter solid carbide endmill (SGS 39363) with a 30° helix angle. It was clamped in a Schunk SINO-R tool holder with approximately 40 mm of overhang. Cutting tests were performed with the aforementioned tool with both two flute and single flute (i.e., one flute removed) geometries.

Cutting tests were performed under stable milling conditions with an axial depth of cut of 3 mm. Other process parameters, such as radial depth of cut (i.e., radial immersion), spindle speed, feed per tooth, and milling configuration (i.e., up/down milling), were varied. Details of the cutting force tests are given in Table 3.1. Each cutting force measurement was repeated three times to allow for a statistical analysis while minimizing the effect of tool wear on the measured cutting forces.

Table 3.1: Milling process parameters selected for cutting force measurements.

Cut Direction	Radial Immersion (%)	Spindle Speed (krpm)	Feed (mm/tooth)
Up Milling	10	8	(0.025, 0.05, 0.10, 0.15, 0.20, 0.25)
Down Milling	10	8	(0.025, 0.05, 0.10, 0.15, 0.20, 0.25)
Down Milling	10	(1, 2, 3, 4, 6, 8, 10, 12.5, 15, 17.5, 20)	0.10
Down Milling	(10, 30, 50)	8	0.10

3.4.2 Feed per Tooth Dependence

The following experimental results compare the specific force coefficients calculated using the average force, linear regression and instantaneous force, nonlinear optimization methods over a range of feed per tooth values. The cutting force measurements were repeated three times for each of the selected feed per tooth values, which are given in Table 3.1.

Figure 3.11 shows the result of the average force, linear regression analysis of the measured cutting forces over the range of feed per tooth values. A satisfactory fit was achieved as indicated by the coefficients of determination, r^2. The reported, measured cutting forces reflect the average forces calculated over the three repeated measurements. The calculated specific force coefficients are given in Table 3.2.

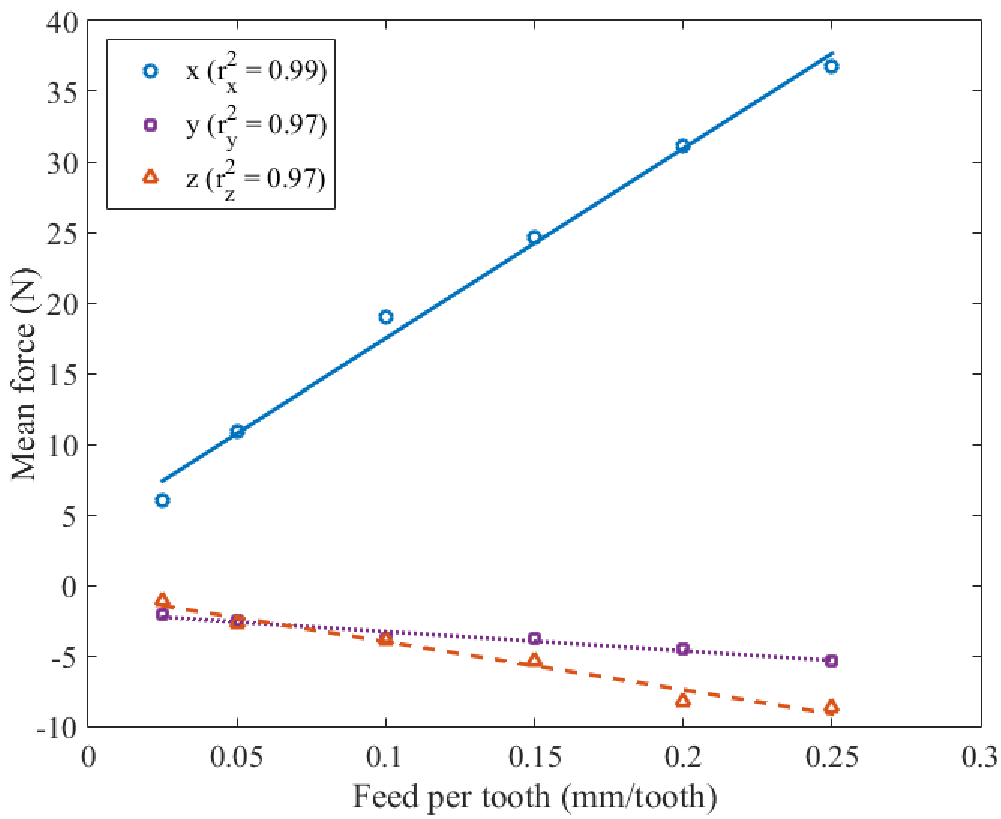

Figure 3.11: Average force, linear regression results from the 10% radial immersion up milling cut conducted at a spindle speed of 8 krpm.

Table 3.2: Specific force coefficients calculated using the average force, linear regression method for the 10% radial immersion up milling cut conducted at a spindle speed of 8 krpm.

Cutting Force Coefficients ($\mathrm{N/mm^2}$)		Edge Force Coefficients ($\mathrm{N/mm}$)	
k_{tc}	805	k_{te}	6
k_{nc}	418	k_{ne}	6
k_{ac}	227	k_{ae}	1

The cutting force coefficients, determined using the instantaneous force, nonlinear optimization method, over the range of selected feed per tooth values are given in Figure 3.12. The mean value of the three repeat measurements are reported along with the 95% confidence interval which was calculated using the t-distribution. It is observed that the tangential and normal cutting force coefficients vary nonlinearly with feed per tooth as was reported by other researchers in [62]. No observable trend was noted in the edge force coefficients.

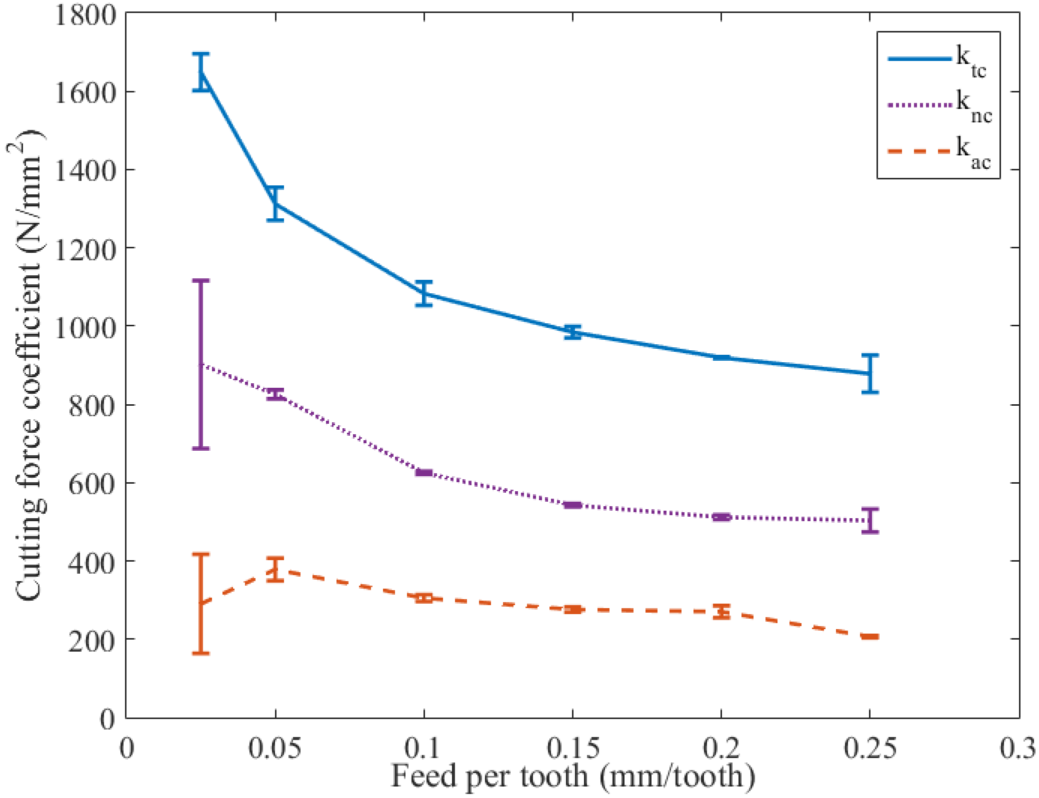

Figure 3.12: Cutting force coefficients calculated using the instantaneous force, nonlinear optimization method for a 10% radial immersion up milling cut conducted at a spindle speed of 8 krpm.

For comparison purposes, a series of cutting tests were performed with identical milling parameters (i.e., spindle speed, axial depth of cut, radial immersion). However, rather than an up milling configuration, a down milling configuration was employed. The resulting specific force coefficients calculated using the average force, linear regression and instantaneous force, nonlinear optimization methods are shown in Table 3.3 and Figure 3.13, respectively. It is observed that the specific force coefficients for the different milling configurations are in good agreement.

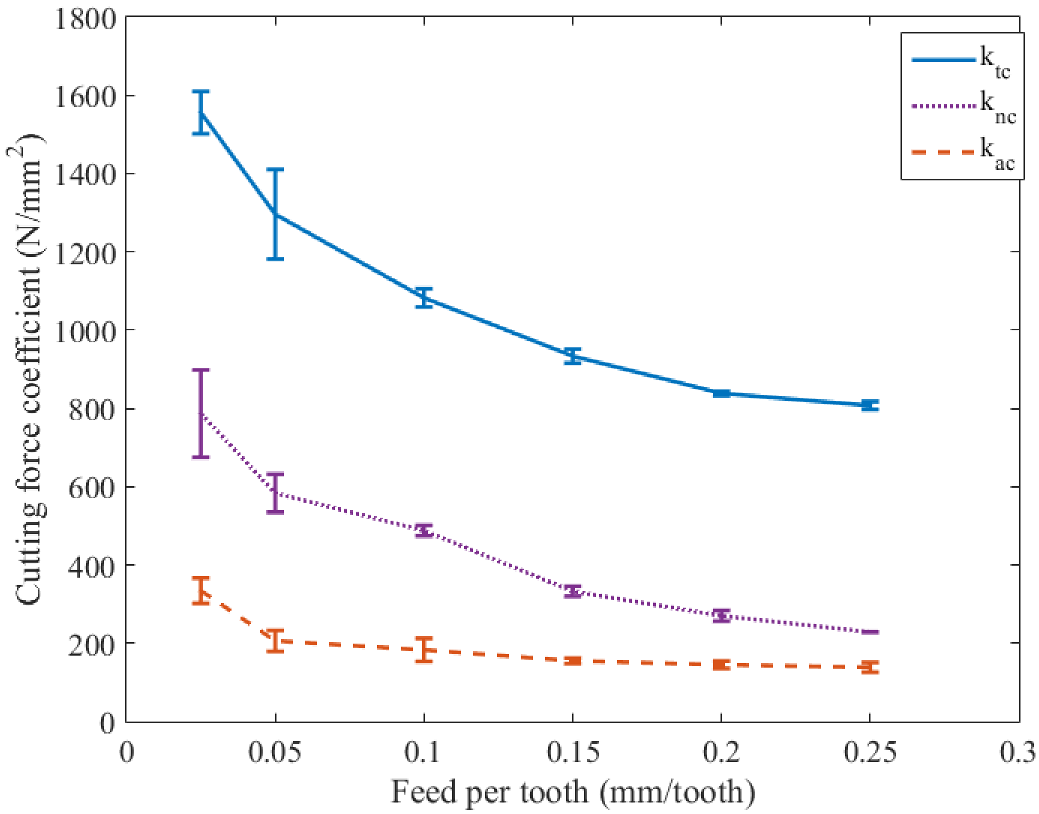

Figure 3.13: Cutting force coefficients calculated using the instantaneous force, nonlinear optimization method for a 10% radial immersion down milling cut conducted at a spindle speed of 8 krpm.

Table 3.3. Specific force coefficients calculated using the average force, linear regression method for the 10% radial immersion down milling cut conducted at a spindle speed of 8 krpm.

Cutting Force Coefficients (N/mm^2)		Edge Force Coefficients (N/mm)	
k_{tc}	786	k_{te}	11
k_{nc}	417	k_{ne}	11
k_{ac}	158	k_{ae}	1

The instantaneous, uncut chip thickness as seen by the cutting tool as each flute engages in the cut is influenced by both the commanded feed per tooth and percent radial immersion. For example, if the commanded feed per tooth is held fixed and percent radial immersion is decreased, the instantaneous, uncut chip thickness also decreases. To study the effects of radial immersion on the specific force coefficients, a series of cutting tests were performed at 10%, 30%, and 50% radial immersion while holding other milling parameters fixed. The resulting tangential cutting force coefficients, calculated using the instantaneous force, nonlinear optimization method, are reported in Figure 3.14 along with the 95% confidence intervals. A statistically significant variation in the tangential cutting force coefficient as a function of radial immersion may be observed. A similar trend in the normal direction coefficient was observed. However, an overlap of the 95% confidence interval precluded a statistically significant result.

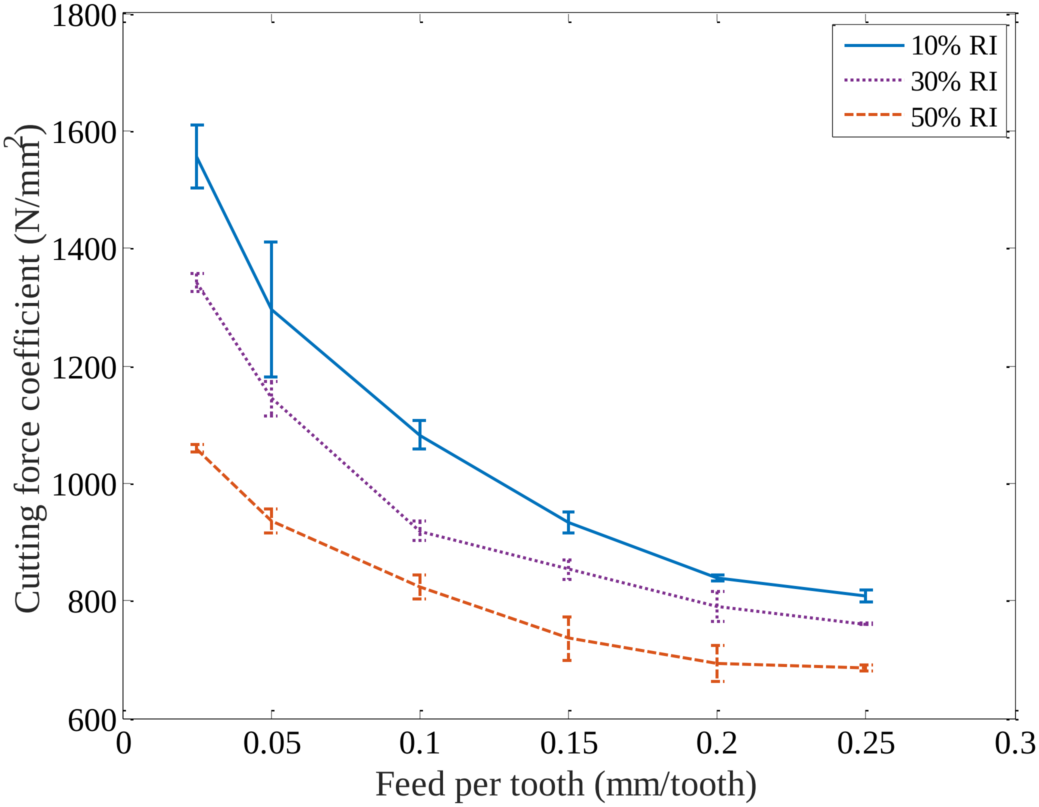

Figure 3.14: The tangential cutting force coefficient, calculated by the instantaneous force, nonlinear optimization method, as a function of radial immersion.

3.4.3 Cutting Speed Dependence

A series of cutting tests were performed over a range of spindle speeds and the force coefficients were calculated using the instantaneous force, nonlinear optimization method. The averaged results and 95% confidence intervals are displayed in Figure 3.15. The resulting trend is in good agreement with results published by Grossi *et al.* [69, 70]. It is noteworthy that there is a general downward trend in the force coefficients until the critical spindle speed of approximately 12500 rpm. Beyond this critical spindle speed, there is a general upward trend. Typically the downward trend is attributed to thermal softening of the workpiece material due to the increased temperature at the tool/chip interface at high cutting speeds.

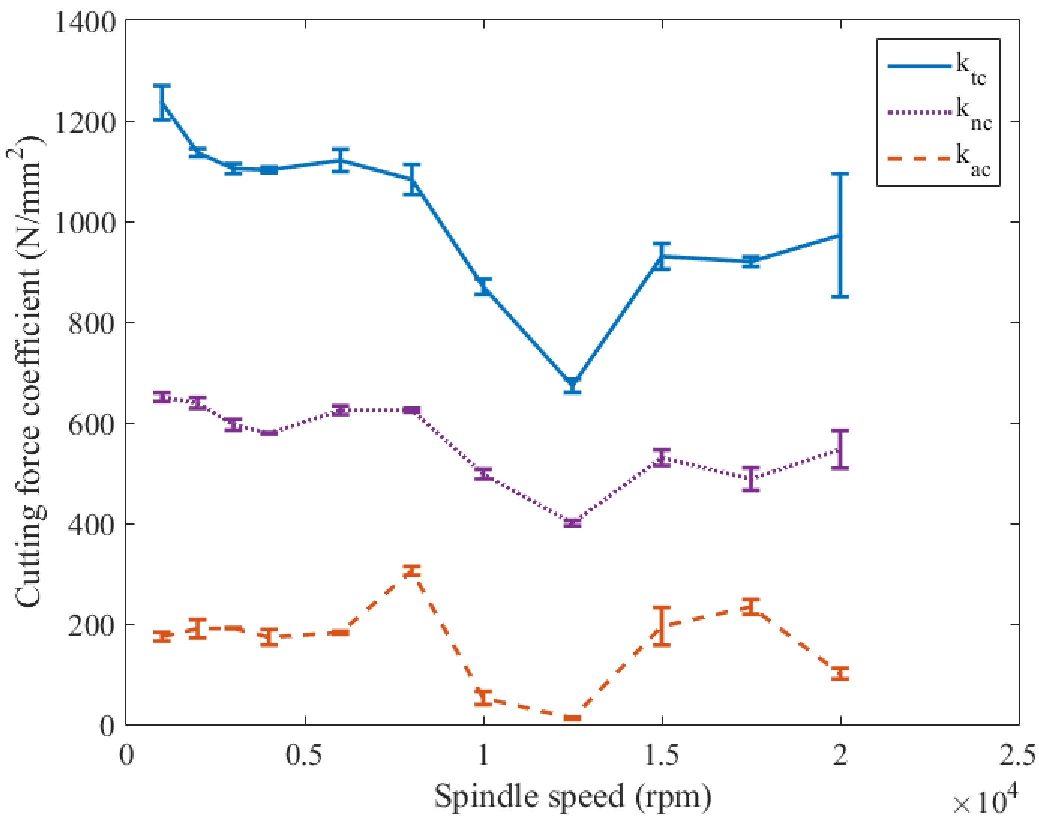

Figure 3.15: Cutting force coefficients calculated using the instantaneous force, nonlinear optimization method over the range of selected spindle speeds for the 10% radial immersion down milling operation.

3.4.4 Validation Testing

Stability testing was conducted at two feed per tooth values, 0.05 mm/tooth and 0.25 mm/tooth, for a 10% radial immersion down milling cut. The cutting force coefficients were calculated using the instantaneous force, nonlinear optimization method. The results are provided in Figure 3.16 and Table 3.4 for a range of feeds. It was determined that the endmill exhibited approximately 30 µm of flute-to-flute runout.

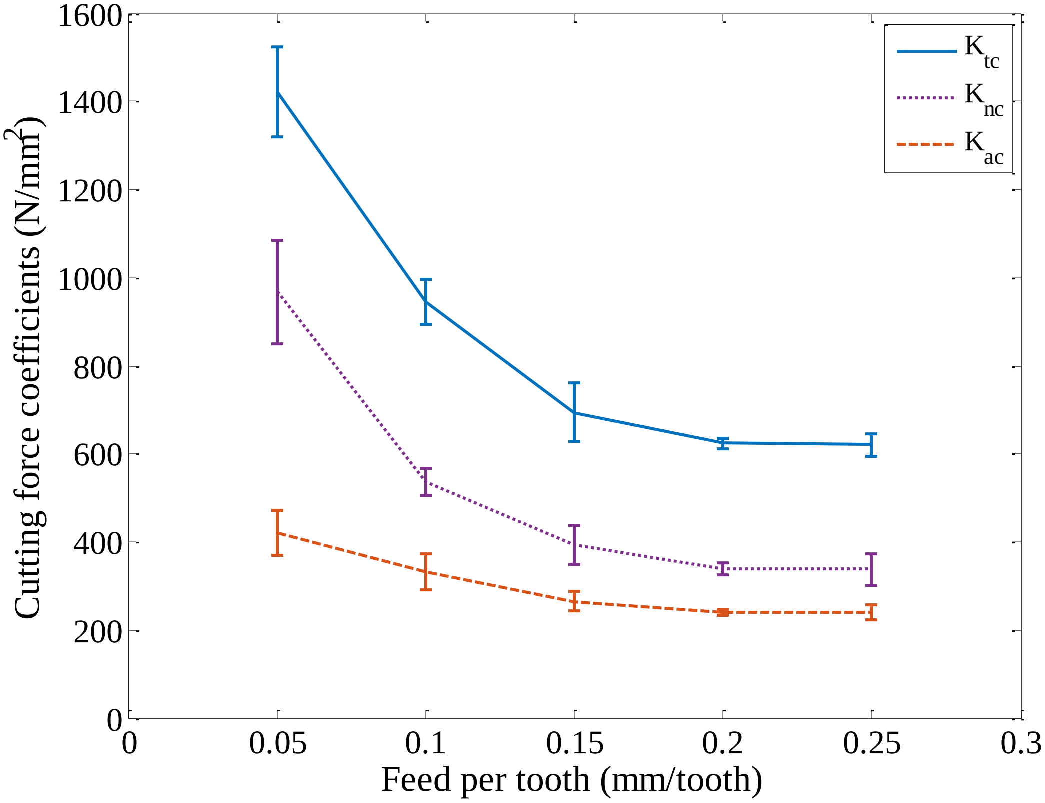

Figure 3.16: Cutting force coefficients calculated using the instantaneous force, nonlinear optimization method for a 10% radial immersion down milling cut conducted at a spindle speed of 8000 rpm.

Table 3.4: Cutting force coefficients used for milling stability predictions using the PTP force diagram.

Feed per tooth ($mm/tooth$)	Cutting force coefficients (N/mm^2)		Edge force coefficients (N/mm)	
0.05	k_{tc}	1422	k_{te}	16
	k_{nc}	967	k_{ne}	13
	k_{ac}	421	k_{ae}	0
Feed per tooth ($mm/tooth$)	Cutting force coefficients (N/mm^2)		Edge force coefficients (N/mm)	
0.25	k_{tc}	620	k_{te}	34
	k_{nc}	337	k_{ne}	20
	k_{ac}	239	k_{ae}	0

The PTP force diagram is conceptually similar to the traditional stability lobe diagram in the sense that it provides a map of stable and unstable axial depth of cut-spindle speed combinations. It conveys this information as a contour map of PTP cutting forces generated from numerous time domain simulations. Because the time domain simulations do not make the simplifying assumptions used to generate analytical stability lobe diagrams for milling and they capture nonlinearities in the milling process, they are particularly well suited for predicting stable milling conditions at low radial immersion. The time domain simulation takes into account the tool and workpiece dynamics in three orthogonal directions as well as various parameters such as flute-to-flute runout and helix angle. The PTP force diagram generated using the specific force coefficients for a feed rate of 0.05 mm/tooth is shown in Figure 3.17. The results of the validation test cuts are included.

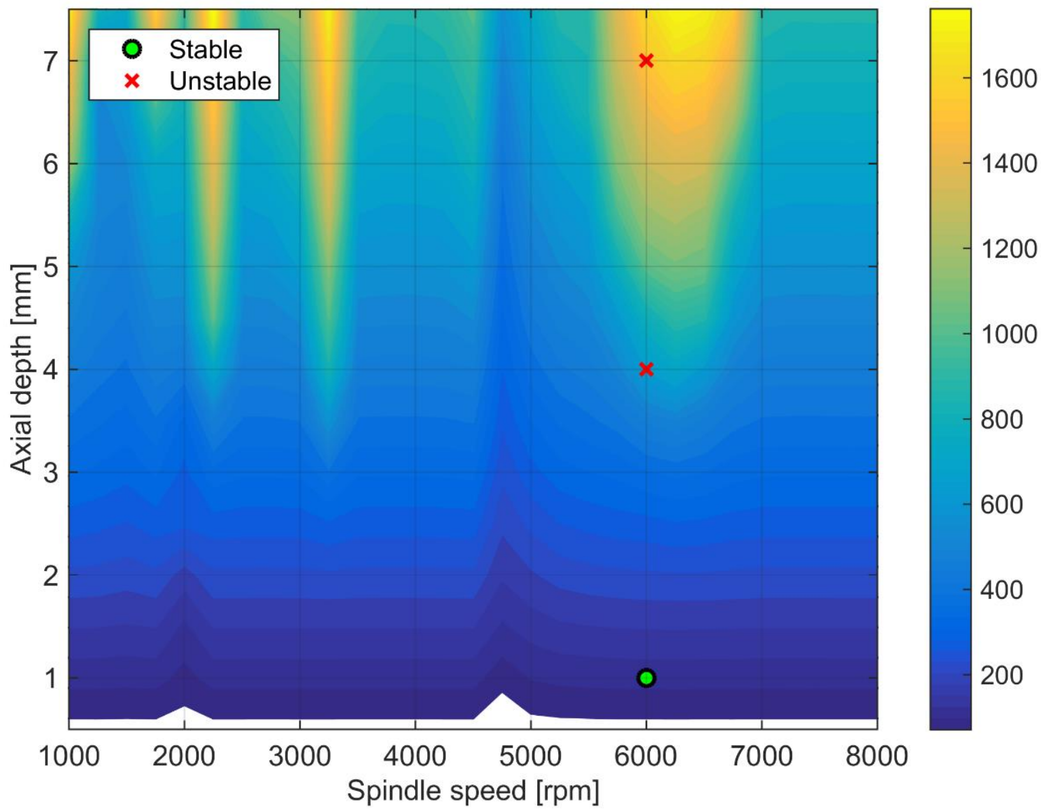

Figure 3.17: PTP force diagram generated using the specific force coefficients calculated for a feed rate of $0.05\ \mathrm{mm/tooth}$. Stable (circle) and unstable (cross) validation test results are shown.

The resulting PTP force diagram generated using the specific force coefficients for a feed rate of $0.25\ \mathrm{mm/tooth}$ is shown in Figure 3.18. The results of the validation test cuts are included. It was observed that in both cases the PTP force diagram accurately predicted stable and unstable axial depth of cut-spindle speed combinations. Furthermore, it is observed that the validation tests conducted at a 4 mm axial depth of cut yielded different results. The lower feed rate cut produced unstable results while the higher feed rate cut was stable.

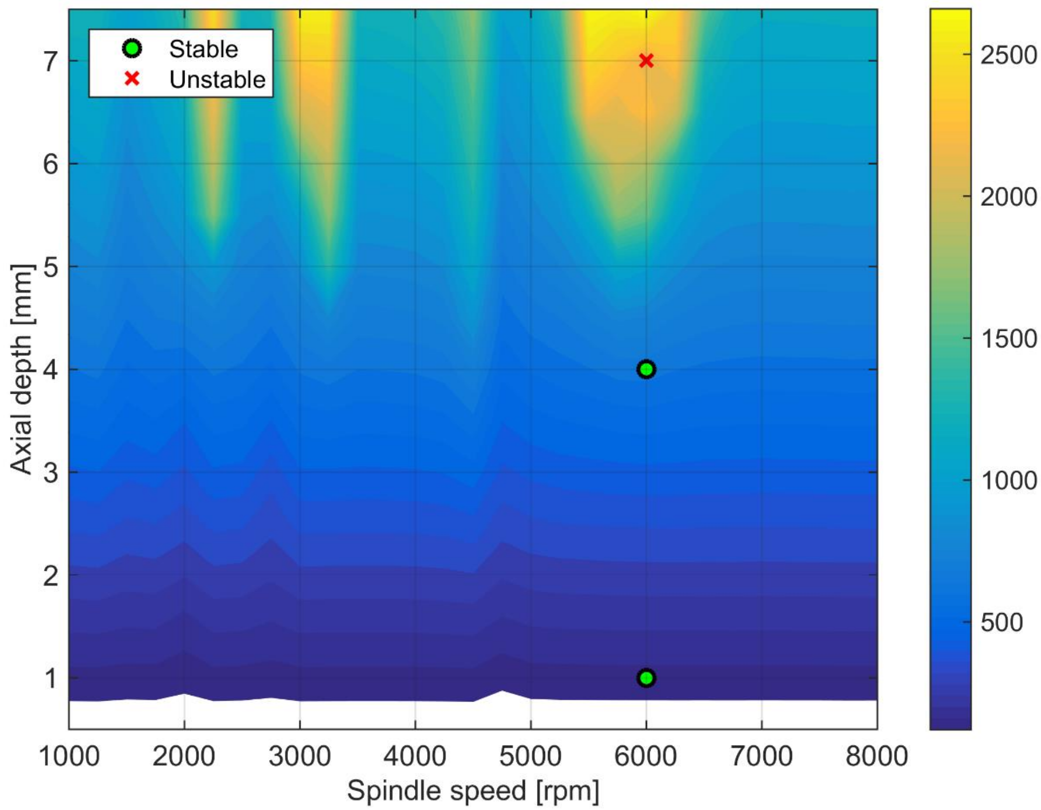

Figure 3.18: PTP force diagram generated using the specific force coefficients calculated for a feed rate of $0.25\ \mathrm{mm/tooth}$. Stable (circle) and unstable (cross) validation test results are shown.

3.4.5 Discussion

It was determined that low feed rates, which are often recommended for hard-to-machine materials, produce disproportionately larger cutting forces per uncut chip area than high feed rates, particularly for low radial immersion milling. From a practical standpoint, this becomes relevant for the finish milling of titanium preforms, which are often encountered in the aerospace industry. The results reported here suggest that high feed rates increase the critical axial depth of cut below which all spindle speeds yield stable milling operations.

With respect to chip formation, the rake angle (i.e., inclination of the cutting edge relative to the surface normal) depends on both the commanded feed per tooth and the radius of the milling tool's cutting edge radius. Although the cutting tool may have a positive rake angle at the macroscopic scale, as the commanded feed per tooth approaches the same order of magnitude as the cutting edge radius of the milling tool, shown in Figure 3.19, the effective rake angle becomes negative. This change in rake angle is accompanied by a change in the mechanism by which the chip is formed. Additionally, the negative rake angle serves to impose compressive stresses on the workpiece surface. These factors contribute to the increase in the cutting force coefficients at low values of feed per tooth. In Figure 3.19, where the cutting tool's rake face is to the right of the cutting edge, it is observed that although the cutting edge radius is on the order of approximately 30 μm, the length of the negative rake angle may be several time larger.

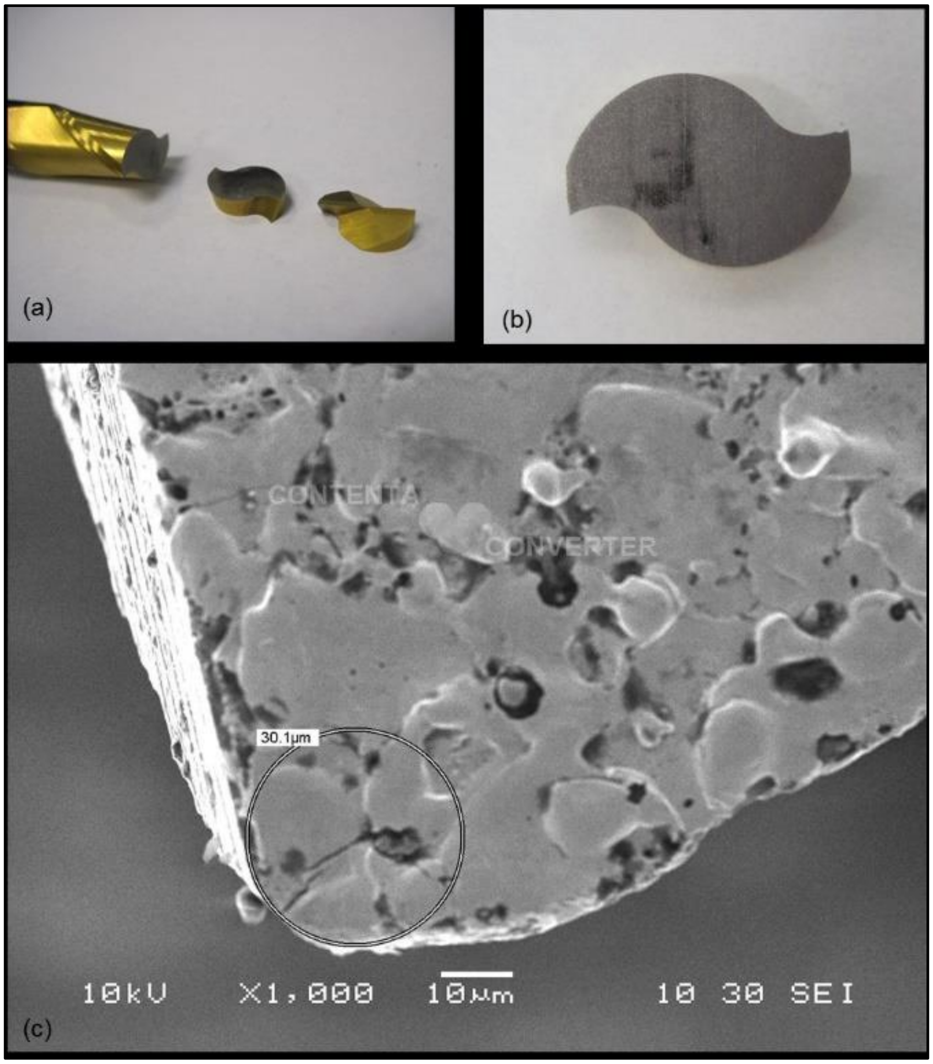

Figure 3.19: A milling tool (a) cut into axial disks (b) to facilitate cutting edge radius measurements with an SEM (c). In (c) the flank face is on the left and the rake race is on the right.

CHAPTER 4: COMPLIANT WORKPIECE MILLING SIMULATION

4.1 Time Domain Model

Based on the "Regenerative Force, Dynamic Deflection Model" described in [10, 22, 71, 72], the time domain simulation determines the instantaneous chip thickness, calculates cutting forces, and uses Euler (fixed time step) numerical integration of the equations of motion to determine tool/workpiece deflections at each incremental time step. It is able to account for the nonlinearity which occurs during the milling process when the deflection of the tool/workpiece become large enough that contact is lost [73]. The underlying assumptions built into the model include the circular tooth path approximation and a mechanistic force model [74].

The instantaneous chip thickness depends on the feed per tooth, the relative vibration of the tool/workpiece in the surface normal direction for the current and previous cutting teeth, and cutter runout. Therefore, instantaneous chip thickness is expressed as:

$$h(t) = f_t \sin(\varphi) + n(t-\tau) - n(t) + r \tag{4.1}$$

where $f_t \sin(\varphi)$ is the nominal, tooth angle dependent chip thickness, $n(t-\tau)$ is the relative vibration of the tool/workpiece in the direction of the surface normal of the previous tooth, $n(t)$ is the current, relative vibration of the tool/workpiece in the surface normal direction, and r is the tooth specific cutter runout. In these expressions, f_t is the feed per tooth, φ is the cutter rotation angle, t is the current time, and τ is the tooth passing period. The vibrations in the direction of the surface normal depend on the relative vibration between the tool and workpiece in the x and y directions as well as the cutter rotation angle and may be expressed as:

$$n(t) = -(x_t - x_w)\sin(\varphi) - (y_t - y_w)\cos(\varphi) \tag{4.2}$$

where x_t and y_t are the vibrations of the tool in the x and y directions, respectively, and x_w and y_w are the vibration of the workpiece in the x and y directions, respectively.

Cutting force calculations are based on the mechanistic force model presented by Budak *et al.* [74] and augmented with a process damping force [19]. At each incremental time step, the chip thickness is evaluated and, in the case where the tool has vibrated out of the cut (i.e., chip thickness is found to be less than or equal to zero), the instantaneous tangential, radial, and axial cutting forces are set to zero. For the case where the instantaneous chip thickness is non-zero, the instantaneous tangential, radial, and axial cutting forces can be expressed, respectively, as:

$$F_t^{i+1} = K_{tc} b h^{i+1} + K_{te} b - C_t b \frac{\dot{r}^i}{V} \tag{4.3}$$

$$F_r^{i+1} = K_{rc} b h^{i+1} + K_{re} b - C_r b \frac{\dot{r}^i}{V} \tag{4.4}$$

$$F_a^{i+1} = K_{ac} b h^{i+1} + K_{ae} b \tag{4.5}$$

where b is the axial depth of cut and h^{i+1} is the instantaneous chip thickness for the current time step. K_{tc}, K_{rc}, and K_{ac} are the tangential, radial, and axial specific cutting force coefficients, respectively, which are associated with "cutting" or shearing. The tangential, radial, and axial edge force coefficients, K_{te}, K_{re}, and K_{ae}, capture the ploughing effect which occurs at small chip thicknesses. The expressions $C_t b\,\dot{r}^i/V$ and $C_r b\,\dot{r}^i/V$ are the process damping forces in the tangential and radial directions, respectively, where C_t and C_r are the tangential and radial process damping coefficients, $\dot{r}^i$ is the velocity in the radial direction calculated in the previous time step, and V is the cutting speed. These instantaneous cutting forces are then transformed into the coordinate system shown in Figure 4.1.

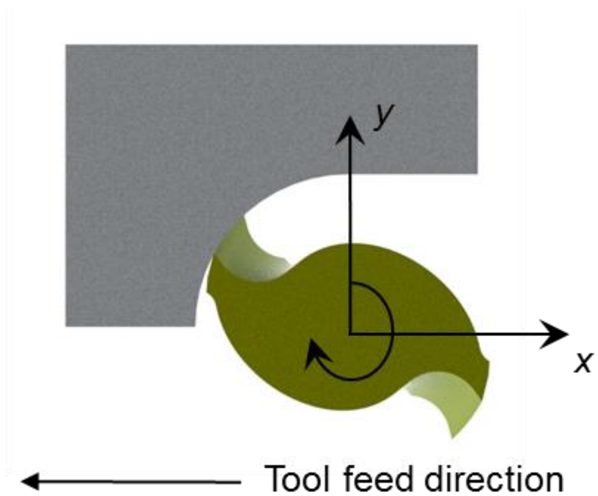

Figure 4.1: Coordinate system definition for the time domain simulation model. A down milling configuration is shown.

The equations of motion are solved in modal coordinates using Euler integration.

The dynamics of the tool and workpiece are represented using modal parameters for an arbitrary number of degrees of freedom. The tool dynamics are considered in two orthogonal directions in the plane of the cut and the workpiece dynamics are considered in all three orthogonal directions. In modal coordinates the dynamic equations of motion may be expressed as:

$$F_q^i = m_q \ddot{q}^i + c_q \dot{q}^i + k_q q^i \tag{4.6}$$

Then, as an approximated solution for velocity, $\dot{q}^{i+1}$, and displacement, q^{i+1}, via Euler integration:

$$\ddot{q}^{i+1} = \frac{\left(F_q^i - c_q \dot{q}^i - k_q q^i\right)}{m_q} \tag{4.7}$$

$$\dot{q}^{i+1} = \dot{q}_i + \ddot{q}^{i+1} \Delta t \tag{4.8}$$

$$q^{i+1} = q^i + \dot{q}^{i+1} \Delta t \tag{4.9}$$

where m_q, c_q, and k_q are the mass, damping, and stiffness values, respectively, expressed in modal coordinates, and Δt is the time step.

Additionally, the simulation model allows for a variety of tool geometries including an arbitrary number of cutting teeth, variable teeth spacing, different helix angles for each tooth, and cutter teeth runout. As a practical consideration it is important to select a time step which is sufficiently small that the Euler integration method provides a numerically stable solution. A rule of thumb is that the time step should be at least ten times smaller than the period associated with the highest oscillation frequency present in the system being modeled. Also, the number of time steps (i.e., cutting tool revolutions) should be sufficiently high for the initial transient behavior to decay.

4.1.1 Peak-to-Peak Force Diagram

As previously mentioned, the outcome of individual time domain simulations contains information specific to the individual spindle speed-axial depth of cut combinations. This includes the instantaneous cutting forces and tool/workpiece deflections, velocities, and accelerations. The PTP force diagrams represent numerous time domain simulations performed over a range of spindle speed-axial depth of cut combinations. The range and step size of the spindle speed and axial depth of cut is specified, and the time domain simulation is performed for each combination. At the conclusion of each simulation the steady state portion of the time domain cutting forces are examined for the maximum peak-to-peak (PTP) force difference. Figure 4.2 illustrates the process of truncating the initial transients of the cutting force signal and extracting the PTP force for a single combination of spindle speed and axial depth of cut. The PTP force for each combination of spindle speed and axial depth of cut is used to generate a contour map over the range of spindle speeds and axial depth of cuts. The result is analogous to the traditional stability lobe diagram in the sense that it conveys a global representation of stable and unstable spindle speed and axial depth of cut combinations while retaining the specific, local information of the individual combinations; see Figure 4.3.

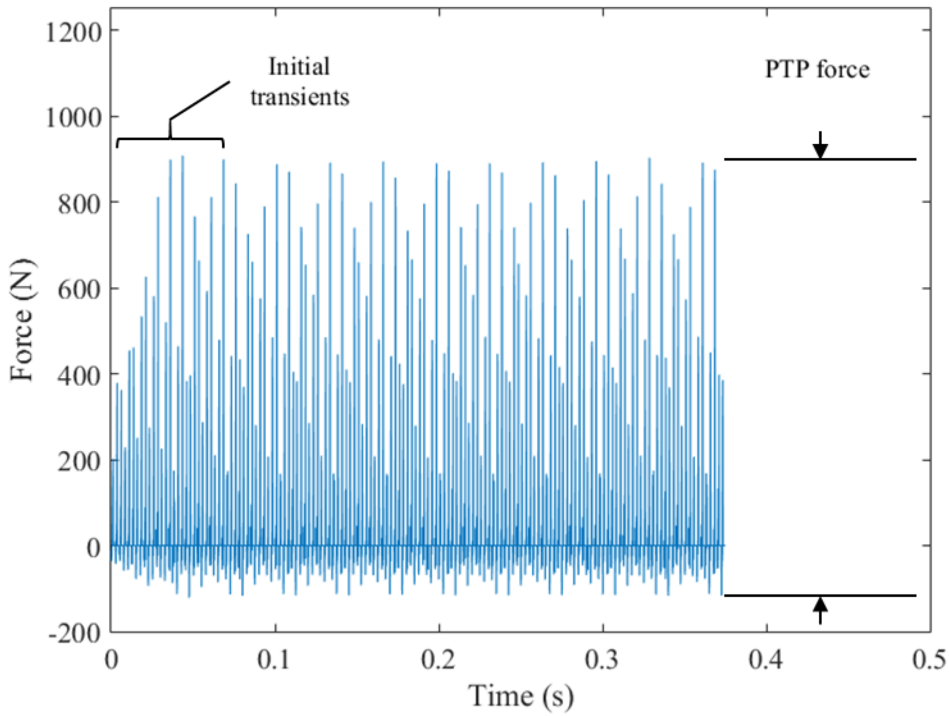

Figure 4.2: Time domain cutting force signal resulting from a simulation conducted at a single spindle speed-axial depth of cut combination with the initial transients and PTP forces denoted.

Example results, given in Figure 4.3, illustrate the stability regions and the stabilizing effects of process damping which occurs at low spindle speeds. The magnitude of the PTP force for an individual combination of spindle speed and axial depth of cut is inconsequential as stable milling conditions may generate large cutting forces. In determining milling stability based on the PTP force diagram, the primary metric is the rate of change of the PTP cutting forces as a function of spindle speed and axial depth of cut. In terms of finishing milling of compliant workpieces, cutting forces may be low due to the restricted radial and axial depths of cut (i.e. due to constraints imposed by chatter).

However, rapidly changing PTP forces over a range of spindle speeds and axial depths of cut are still indicative of instability.

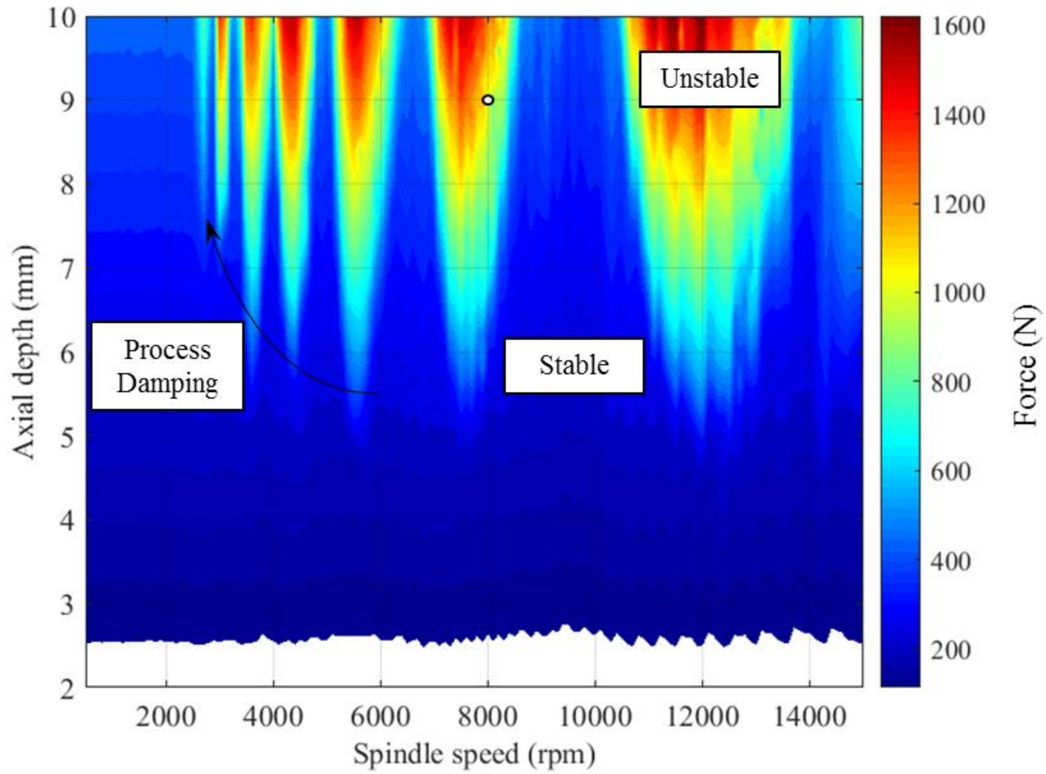

Figure 4.3: Example PTP force diagram with process damping region.

4.1.2 Amplitude Ratio Diagrams

Although the PTP force diagram is a powerful tool that provides a prediction of global stability behavior over a range of spindle speeds and axial depths of cut, it does not provide a distinct boundary between stable and unstable behavior as with traditional stability lobe diagrams. This lack of distinction between stable and unstable behavior implies that the interpretation of these diagrams is largely qualitative. In an effort to eliminate qualitative interpretation and establish a distinct boundary between stable and unstable machining behavior a new stability metric has been developed. The new metric, which will be referred to as the “amplitude ratio”, provides a quantitative measure of the existence and severity of chatter.

As previously mentioned, the outcome of individual time domain simulations contains information specific to the individual spindle speed-axial depth of cut combinations. This includes the instantaneous cutting forces and tool/workpiece deflections, velocities, and accelerations which can be represented in the frequency domain. For an individual time domain simulation of a stable machining operation, the frequency content of the milling signals contains the tooth passing frequency, runout frequency, and multiples (harmonics) of these. Because of this fact, stable cuts are typically described as having a “clean” sound. Unstable cuts also contain these frequency components, however, they also emit a chatter frequency which results in a “harsh, unappealing” sound on the shop floor. Since chatter can be recognized by the manifestation of a chatter frequency, the severity of chatter can be established by the amplitude of the chatter frequency component relative to the tooth passing frequency amplitude.

Amplitude ratio diagrams are generated through multiple iterations of a time domain simulation over a range of spindle speed and axial depth of cut combinations. At the conclusion of each simulation the steady state portion of a frequency domain milling signal is examined for the maximum amplitude of the tooth passing frequency (and harmonics) component and, if present, the chatter frequency component. Figure 4.4 provides an illustrative example where the selected milling signal is the relative displacement between the tool and workpiece. For the purposes of experimental validation, a measurable quantity, such as workpiece velocity (laser vibrometer) or acceleration (accelerometer), may be selected.

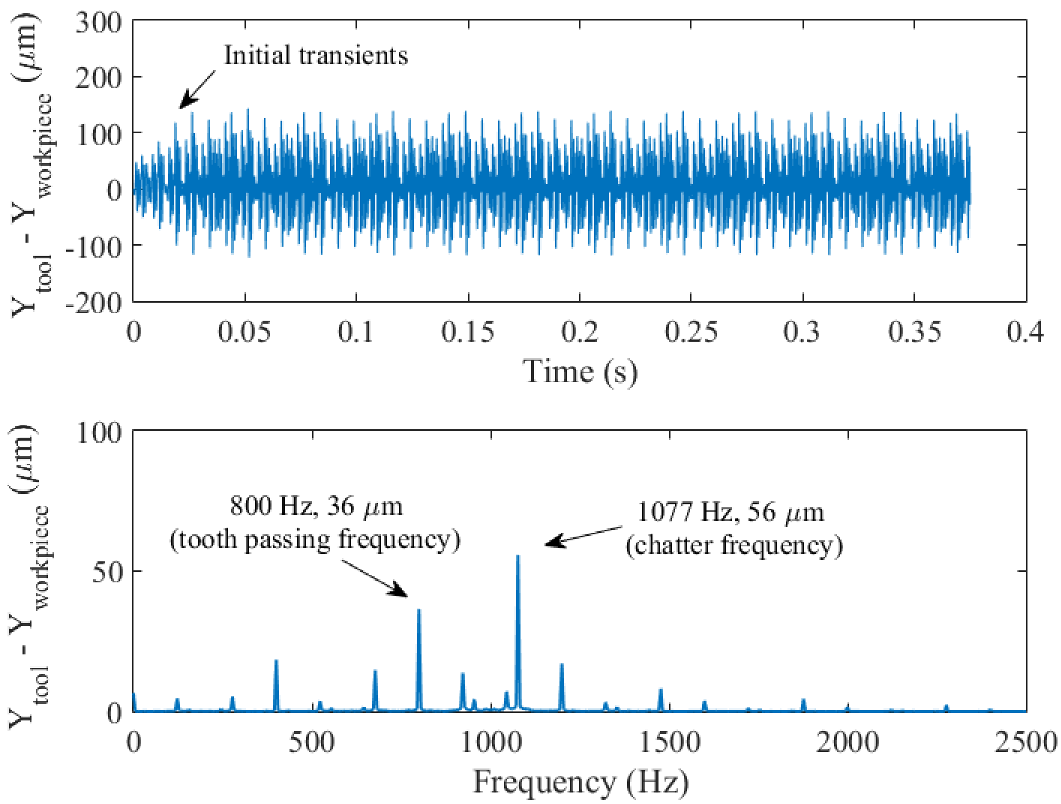

Figure 4.4: The relative displacement of the tool and workpiece given in the time and frequency domains. The tooth passing frequency component and chatter frequency component are indicated, and the amplitude ratio is calculated as 1.56.

Finally the amplitude ratios for each combination of spindle speed and axial depth of cut are plotted as a contour map. The amplitude ratio, r_{amp}, is calculated as:

$$r_{amp} = \frac{A_{cf}}{A_{tpf}} \tag{4.10}$$

where A_{cf} is the amplitude of the chatter frequency component and A_{tpf} is the maximum amplitude of the tooth passing frequency (and harmonics) component in a given milling signal. An illustrative example, which was generated for the same machining operation as the PTP force diagram given in Figure 4.3, is shown in Figure 4.5. These diagrams provide similar global stability information. Large stable regions (white) are evident that are predicted to contain no chatter frequency component. Further, the severity of chatter is evident by value of the amplitude ratio. It may be the case that a small chatter frequency component ($r_{amp} \ll 1$) is acceptable for most machine shop applications. However, as the amplitude ratio becomes larger chatter becomes increasingly severe.

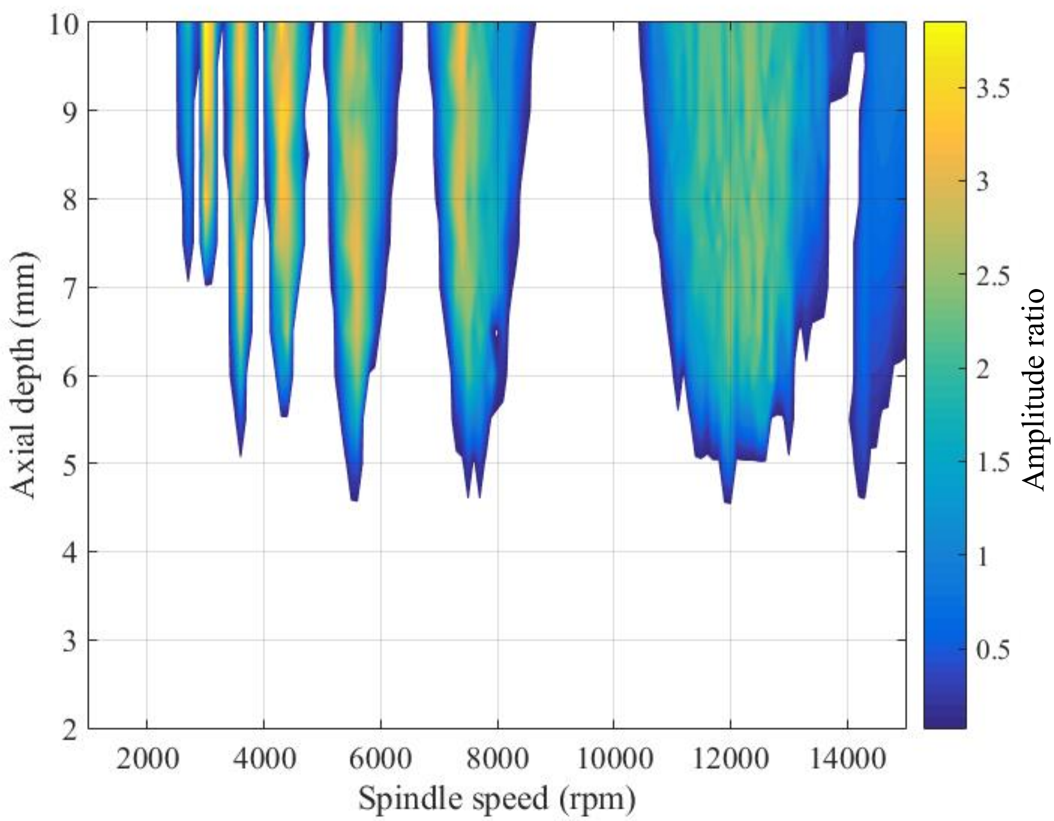

Figure 4.5: Example amplitude ratio diagram.

4.1.3 Spatially Dependent Workpiece Dynamics

Two of the factors that complicate stable machining of near net shape preforms are:

1) the spatial dependence of workpiece dynamics
2) the continuous variation of workpiece dynamics as material is removed

For machining stability analyses, using both analytical and numerical techniques, the dynamic response of the tool and/or workpiece dictate the stability limit for each machining process. Typically the tool and/or workpiece dynamics are measured or modeled at their most flexible location because it represents a critical limitation in terms of stability. This method is well-suited for machining processes where the cutting tool flexibility (rather than the workpiece flexibility) limits the stable axial depth of cut because the tool point dynamics remain constant throughout the cut (i.e., assuming that spindle dynamics are unaffected by centrifugal, thermal, or gyroscopic effects and/or changes in preload [75, 76]). This scenario presents in cases where the machine-toolholder-tool system is considerably more flexible than the quasi-rigid workpiece. However, in cases where the workpiece flexibility limits the stable axial depth of cut, the material removal rate can be increased by using sophisticated toolpath strategies to leverage the spatial dependence of the workpiece dynamics.

A methodology to incorporate the spatial variation of workpiece dynamics into the time domain simulation is presented. The dynamics, represented by the frequency response function, over a grid of discrete positions on the workpiece are modeled and predicted using the finite element method following the analysis outlined in [77]. Modal parameters were extracted using the peak picking technique, and the simulated modal stiffnesses were normalized to the minimum stiffness value thereby constituting a lookup table of multiplication factors. The FRF of the workpiece was experimentally measured at the location of minimum stiffness, and the lookup table of multiplication factors is used to extrapolate the measured stiffness to the simulation locations. Linear interpolation was used to calculate the unknown modal stiffnesses at coordinates adjacent to the simulation coordinates. In the time domain simulation, the tool position at each discrete time step is monitored, and the modal parameters for that position are used to solve the dynamic equations of motion in modal coordinates.

In this research the workpiece dynamics were modeled and predicted using the commercial finite element package Abaqus®. The two-stage analysis procedure consists of: (1) eigenvalue extraction to determine the workpiece natural frequencies and mode shapes and (2) a steady-state dynamic analysis to calculate the linearized system response (i.e., frequency response function). To provide an example of the dynamic analysis procedure, a representative flexible workpiece with clamped-clamped-clamped-free boundary conditions was chosen; see Figure 4.6(a).

After modeling and/or importing the workpiece geometry into Abaqus® CAE, the material properties were defined. In this representative case the workpiece material was Ti6Al4V (i.e., titanium alloyed with aluminum and vanadium) for which the relevant material properties are given in Table 4.1. The refined mesh, shown in Figure 4.6(b), has a fine density in regions of interest (i.e., the flexible, thin wall) and a coarse density otherwise. Using the Abaqus® vernacular, an encastrè boundary condition (i.e., all translations and rotations are set equal to zero) was defined at the workpiece base. This boundary condition does not perfectly model the true, bolted connection, but the resulting analysis provides sufficiently accurate results.

Table 4.1: Material properties for Ti6Al4V

Density	$4430\ kg/m^3$
Young's modulus	$113.8\ GPa$
Poisson's ratio	0.342

Eiegenvalues (i.e., natural frequencies) and eigenvectors (i.e., mode shapes) were extracted using the default method (i.e., Lanczos) by solving the characteristic equation for undamped, free vibration which is given by:

$$(-\omega^2 M^{mn} + K^{mn})\phi^n = 0 \tag{4.11}$$

where M is the mass matrix, K is the stiffness matrix, ϕ is the eigenvector, and mn are the degrees of freedom.

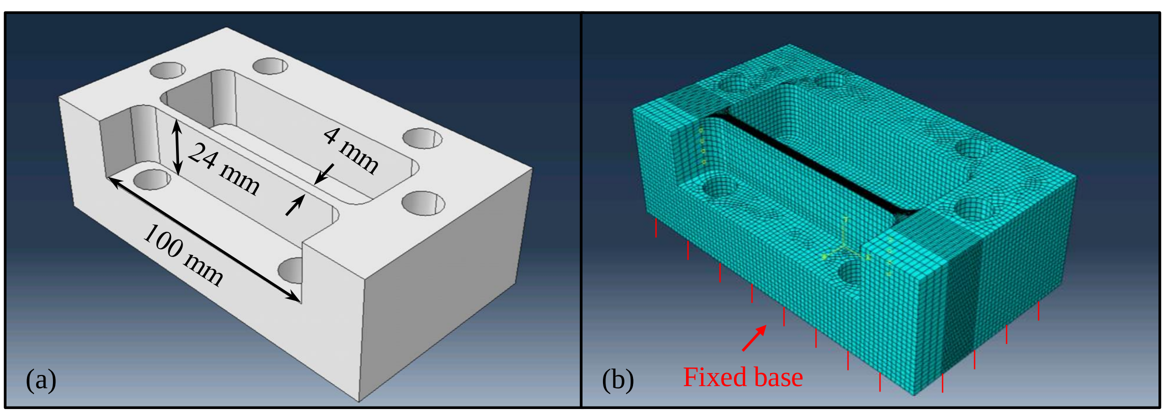

Figure 4.6: Representative flexible workpiece with clamped-clamped-clamped-free boundary conditions (a) with refined mesh (b).

The eigenvalue extraction was performed over a frequency range of $0 - 20\ kHz$, and the first three mode shapes of the flexible, thin wall, which occur at $6596\ Hz$, $10293\ Hz$, and $16305\ Hz$ are shown in Figure 4.7. As expected, for each mode of vibration ($n = 1, 2, 3$) there are $n - 1$ nodes with zero theoretical displacement.

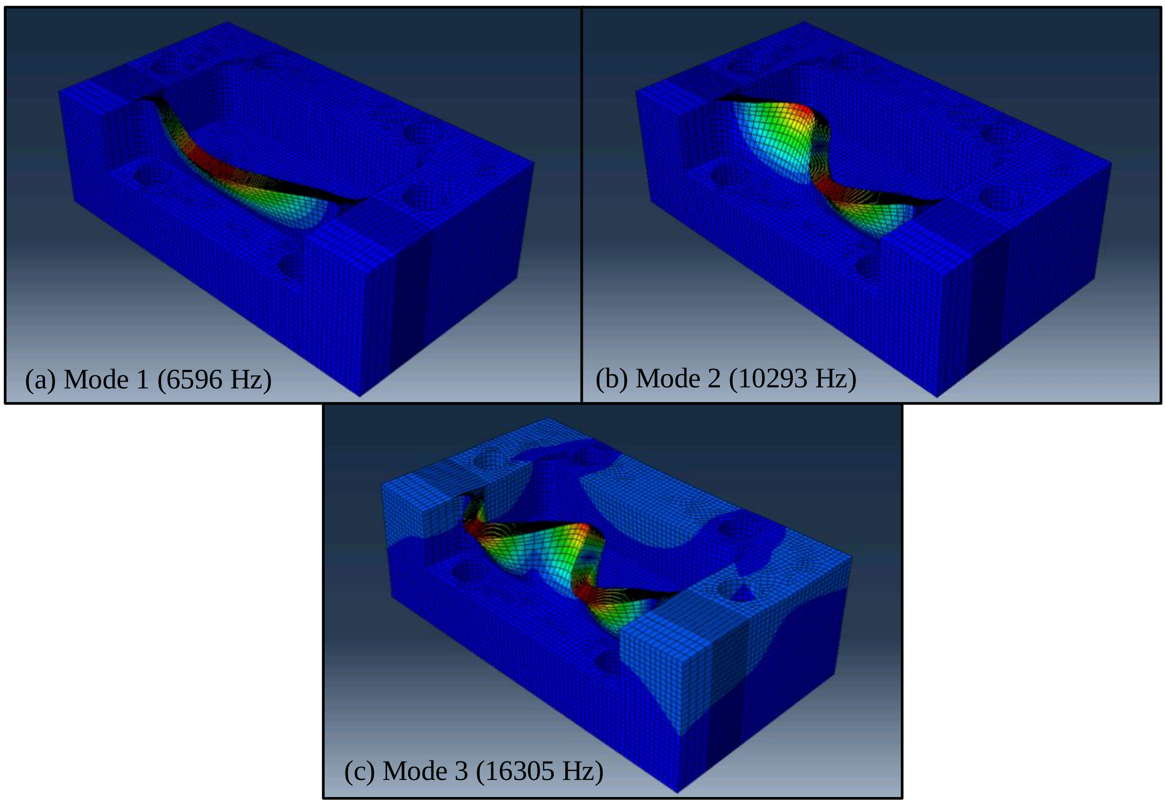

Figure 4.7: First three bending mode shapes for the flexible, thin wall.

Once the eigenvalues (i.e., natural frequencies) and eigenvectors (i.e., mode shapes) were determined, the second stage of the procedure determines the linearized system response (i.e., frequency response function) subject to a continuous harmonic excitation using a steady-state dynamic analysis. Abaqus® uses the eigenvalues extraction in the first stage to calculate the steady state solution of the equations of motion as a function of the applied frequency. In practice, the user defines a frequency range of interest over which to perform the dynamic analysis. The range is discretized into frequency steps. Because the information of interest in the system response is localized to bandwidths in the vicinity of the system's natural frequency, frequency step size in these regions should be small enough to provide adequate resolution. This is particularly important for systems with low damping because the frequency response function is defined by sharp peaks over narrow bandwidths.

In order to determine the coordinate dependent stiffness of the flexible, thin wall, the steady-state dynamic analysis was completed over a grid of discrete points as shown in Figure 4.8. The workpiece geometry was subdivided into five 4.8 mm "elements" in the vertical direction and ten 10 mm elements in the horizontal directions.

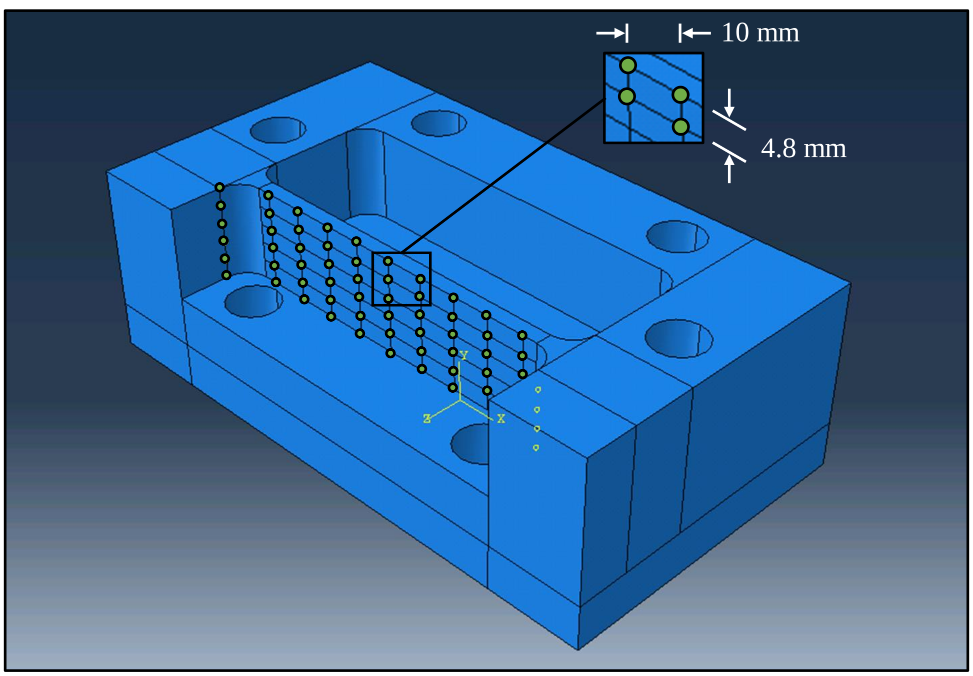

Figure 4.8: Grid of discrete points (green circles) where steady-state dynamic analysis were completed.

A concentrated nodal force is applied to the displacement degree of freedom at the location of interest in the structure's response (i.e., the grid of discrete points). These loads vary sinusoidally with time over the user-defined frequency range. The user-defined, viscous damping ratios for all modes of vibration were defined as 0.0015. Once the steady-state dynamic analysis was completed, the frequency response function for the coordinate of interest was calculated. As shown in Figure 4.9, the FRF, which contains information about the stiffness of the workpiece, varies as a function of workpiece position. It is noteworthy that the FRF at the center, free edge of the workpiece does not contain vibration mode two because it is a node location. The modal parameters (i.e., mass, stiffness, and damping) were extracted from the simulated FRF at each simulation point using the peak picking method.

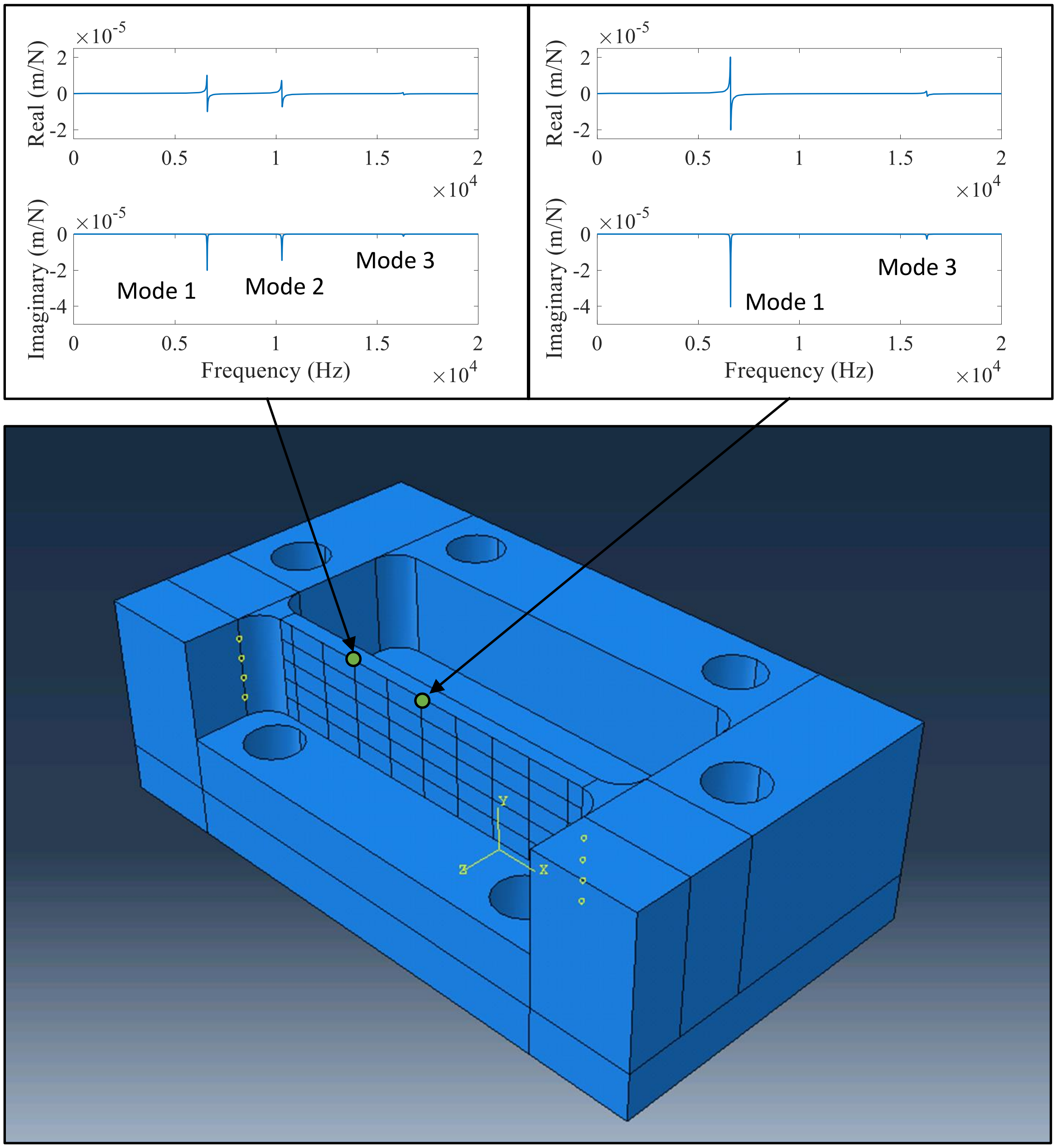

Figure 4.9: Representative frequency response function for two locations at the free edge of the flexible, thin wall.

For each mode of vibration, the modal stiffnesses calculated from the simulated FRFs were normalized to the minimum stiffness value thereby constituting a lookup table of multiplication values. The FRF of the workpiece was experimentally measured at the center of the free edge of the flexible, thin wall which is the location of minimum stiffness for vibration modes one and three. Figure 4.10 shows the measured and simulated FRFs at the center of the free edge. Because of differences in the boundary conditions and damping ratio, the simulated and measured FRFs are frequency shifted and vary in dynamic stiffness. The lookup table of multiplication factors (i.e., from the simulated FRFs) was used to extrapolate the measured modal stiffness to the simulation coordinates.

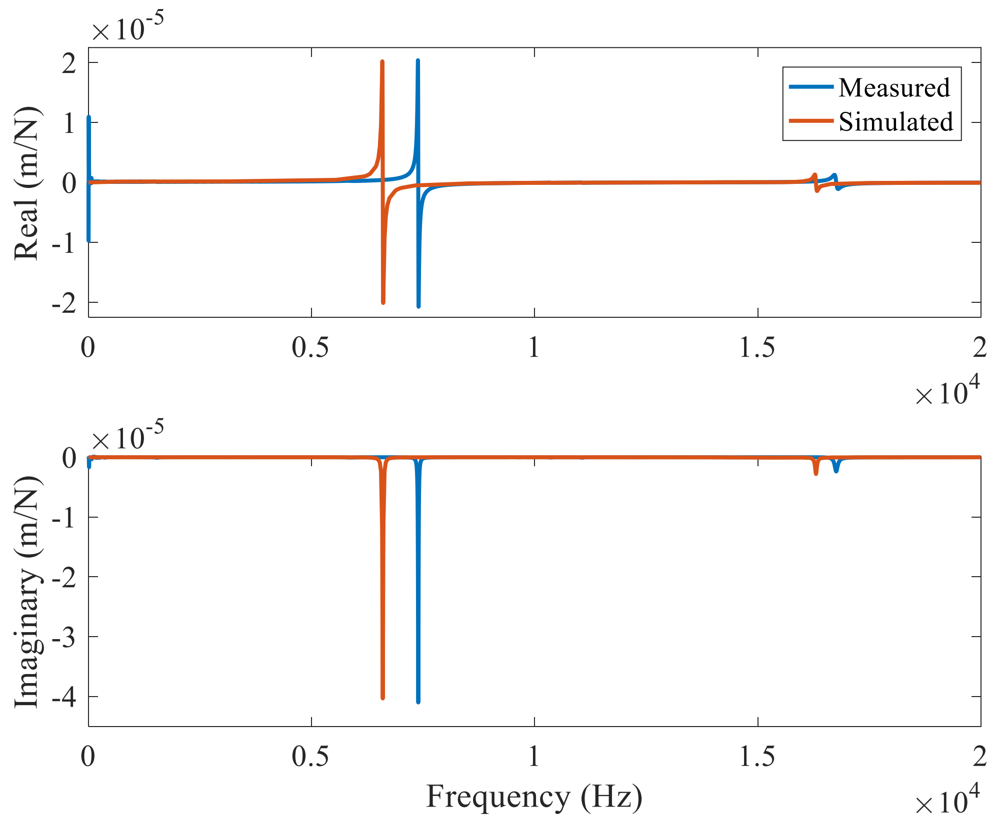

Figure 4.10: Measured and simulated workpiece FRF at the location of minimum stiffness for vibration mode one and three (i.e., center of the free edge).

A linear interpolation of the measured, extrapolated modal stiffnesses was performed to calculate the unknown stiffness values between adjacent coordinates. The interpolated modal stiffness for vibration mode one is shown as a continuous surface in Figure 4.11(b) and at the free edge in Figure 4.11(c). As expected, the maximum stiffness occurs near the fixed edges, and the minimum stiffness occurs at the center of the free edge.

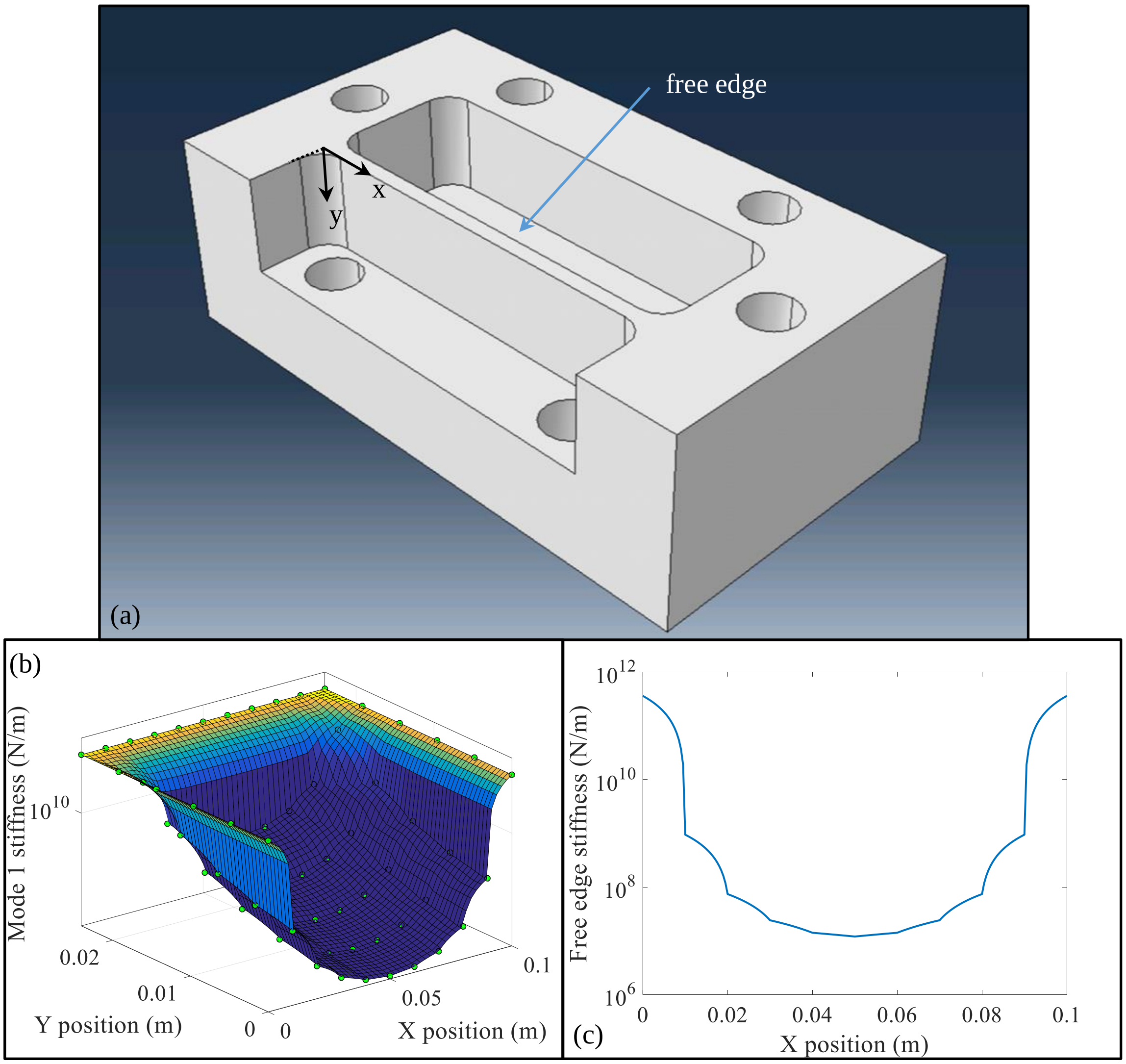

Figure 4.11: Linearly interpolated mode one stiffness for the flexible, thin wall (a) over the entire *xy* surface (b) and at the free edge (c).

The spatially dependent stiffness is incorporated into the time domain simulation by tracking the position of the cutting tool relative to the flexible workpiece and evaluating the workpiece dynamics at that position. The position of the cutting tool relative to the workpiece is a function of the spindle speed, feed per tooth (i.e., chip load), the simulation time step, and the start/end position of the tool relative to the flexible workpiece. The dynamic equation of motion for the workpiece in the *y* direction (i.e., the direction of principal flexibility) is solved in modal coordinates and includes spatially dependent mass, stiffness, and damping. The equation of motion for the workpiece in the y direction can be given as:

$$F_q^i = m_q\left(p_{tw}, {}^{b}\!/_{2}\right)\ddot{q}^i + c_q\left(p_{tw}, {}^{b}\!/_{2}\right)\dot{q}^i + k_q\left(p_{tw}, {}^{b}\!/_{2}\right)q^i \qquad (4.12)$$

where p_{tw} is the position of the cutting tool relative to the workpiece in the *x* direction, b is the axial depth of cut. The spatially dependent modal mass, damping, and stiffness are $m_q\left(p_{tw}, {}^{b}\!/_{2}\right)$, $c_q\left(p_{tw}, {}^{b}\!/_{2}\right)$, and $k_q\left(p_{tw}, {}^{b}\!/_{2}\right)$. At each incremental time step the modal parameters are evaluated at the tool position relative to the workpiece in the x direction and half the axial depth of cut in the *y* direction as defined in Figure 4.11(a).

As an illustrative example, Figure 4.12 shows a solid model representation of a peripheral, down milling cut of a flexible, thin wall where the tool enters the cut near a fixed edge (1), feeds continuously along the workpiece past the point of minimum stiffness (2), and exits the cut near the other fixed edge (3). Figure 4.13 shows the simulated cutting forces in the xyz directions and workpiece velocity in the y direction. In the simulation the cutting tool enters the cut near a fixed edge (1) where the workpiece stiffness is at a maximum, and subsequently, the cutting forces are at a maximum and workpiece velocity is at a minimum. As the cutting tool feeds along the workpiece, the stiffness decreases to a minimum (2), and similarly, the cutting forces reach a minimum and workpiece velocity reaches a maximum. Finally, the cutting tools exits the cut near a fixed edge (3).

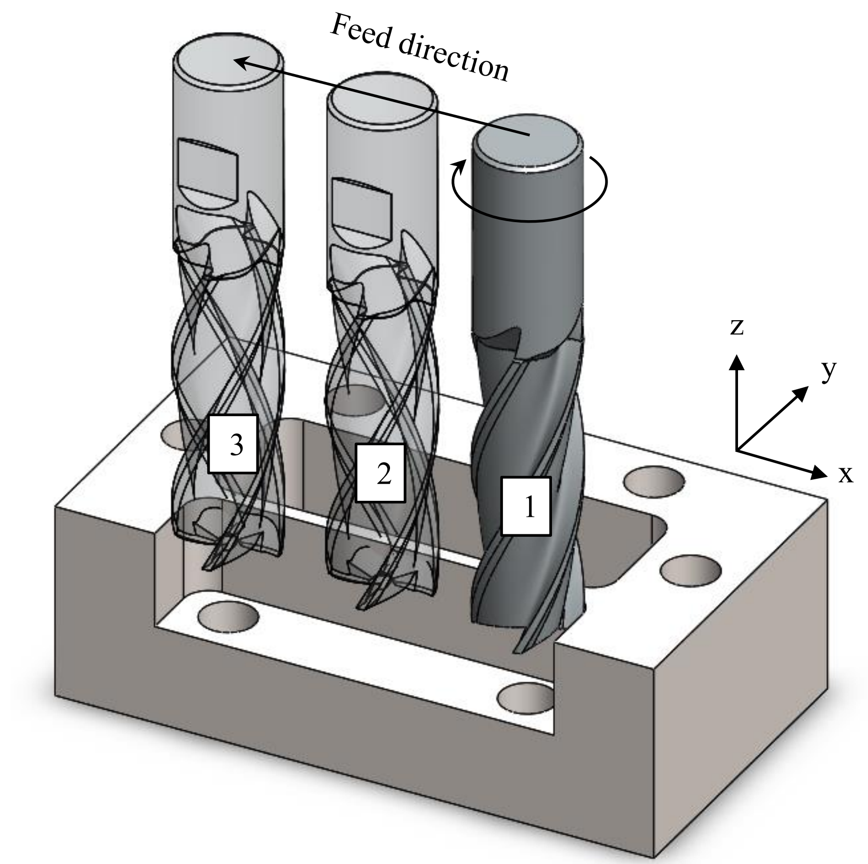

Figure 4.12: Solid model representation of a peripheral, down milling cut of a flexible, thin wall.

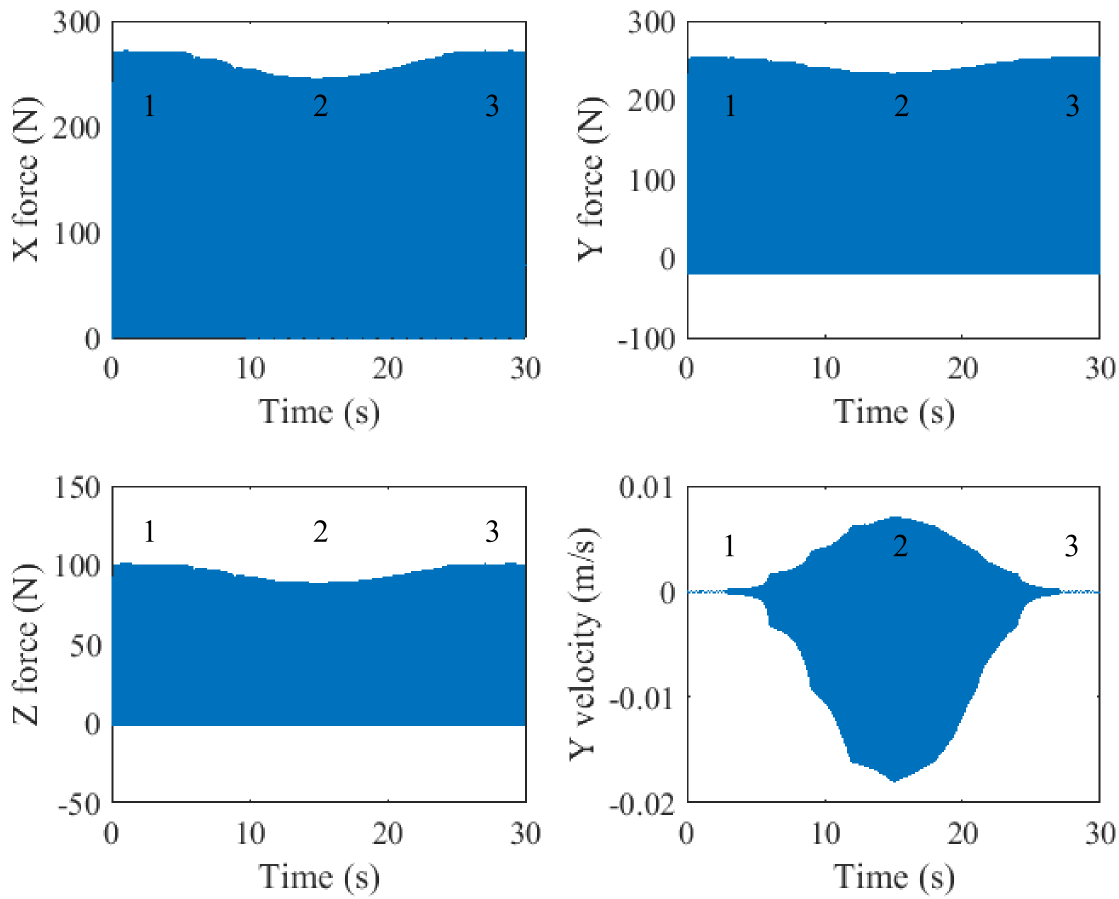

Figure 4.13: Representative example of time domain simulation outputs including spatially dependent workpiece dynamics.

4.2 Modal Parameter Identification

For modeling purposes, modal parameters must be identified to describe the dynamic response of the system (i.e., tool/workpiece). An automated modal parameter identification method has been developed that utilizes a two-stage process including: (1) individual mode identification using the peaking picking method and (2) a nonlinear optimization for all modes. The peak picking method, detailed in [59], is used to perform a preliminary fit to the FRF. Because of modal truncation, where modes are present outside of the measurement bandwidth and contribute to the dynamic response of the dynamometer but cannot be included in the fit, the accuracy of the FRF fit suffers. To reduce this effect and improve the accuracy of the fit, a nonlinear optimization of the FRFs real and imaginary components is performed.

4.2.1 Individual Mode Identification

In this step, the individual modes within the frequency bandwidth of interest are identified. For example, at high frequencies the measurement coherence, which serves as quality index for determining measurement accuracy, may be poor. Therefore, these frequency ranges are truncated. Because the imaginary part of a direct FRF is purely negative, the individual modes of the response can be identified by scanning for the negative peaks. The mode identification algorithm compares each element within a vector with its neighboring elements and recognizes those which are less than both its neighboring elements. For this reason, the method is susceptible to noisy measurement data. A number of strategies are used to minimize this effect. A symmetric moving average filter, whose filtering properties are defined by weighting coefficients and windowing length, is applied to smooth the (potentially) noisy data. The weighting coefficients and windowing length are user-defined variables. It is of practical note that the output of the moving average filter is frequency shifted. The magnitude of the frequency shift is dependent upon the user defined windowing length.

Figure 4.14 shows the real and imaginary parts of a measured force-to-force FRF (dynamometer FRF) where the individual modes within the selected frequency range have been identified (red circles) and numbered. By examination of Figure 4.14, it is shown that

18 modes have been identified. To further downselect the number of identified modes, the user is prompted to select the individual modes to be included in the fitting algorithm. For the example provided here a total of 11 modes have been designated.

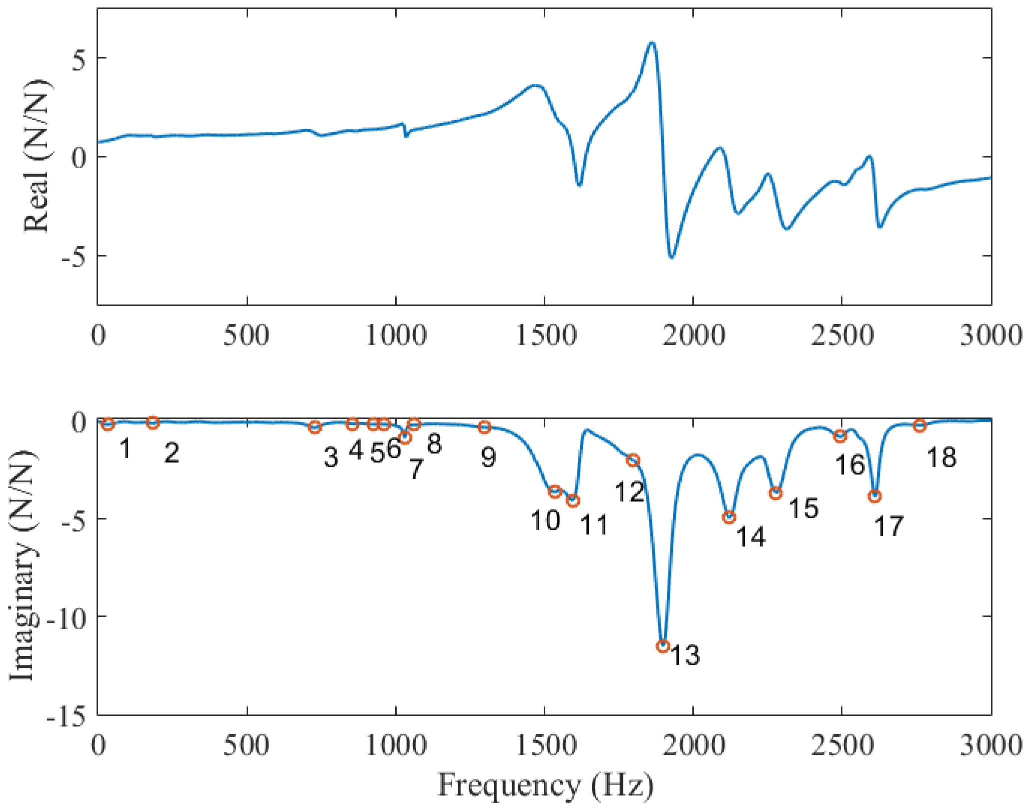

Figure 4.14: An illustrative force-to-force FRF with individual modes identified (red circles) and numbered.

Before optimizing for the combined response of all the modes together, the peak picking method was executed over small frequency ranges to identify the modal mass, damping ratio, and natural frequency for each mode independently. These parameters were used to provide an initial estimate of the solution before optimizing for the combined response of all the modes together. This ensured faster convergence towards the solution when optimizing for the combined FRF.

To identify the modal parameters for each selected mode, the imaginary part of the FRF is scanned for the most negative peak (most flexible). Once the peak has been identified, a frequency range is defined within which the peak picking method is applied. The defined frequency range depends on the location of the individual mode within the total response, and its proximity to the neighboring modes. Within this range the peak picking method is employed and the modal parameters for that individual mode are identified. The identified mode is then deleted from the overall response and the process is repeated for the next most negative peak. Figure 4.15 shows the measured FRF from Figure 4.14 with mode 13 deleted and the removed mode which was fit using the peak picking method. This process is completed iteratively until all of the selected modes have been fit using the peak picking method. The measured FRF and corresponding individual modes identified using the peak picking method are shown in Figure 4.16.

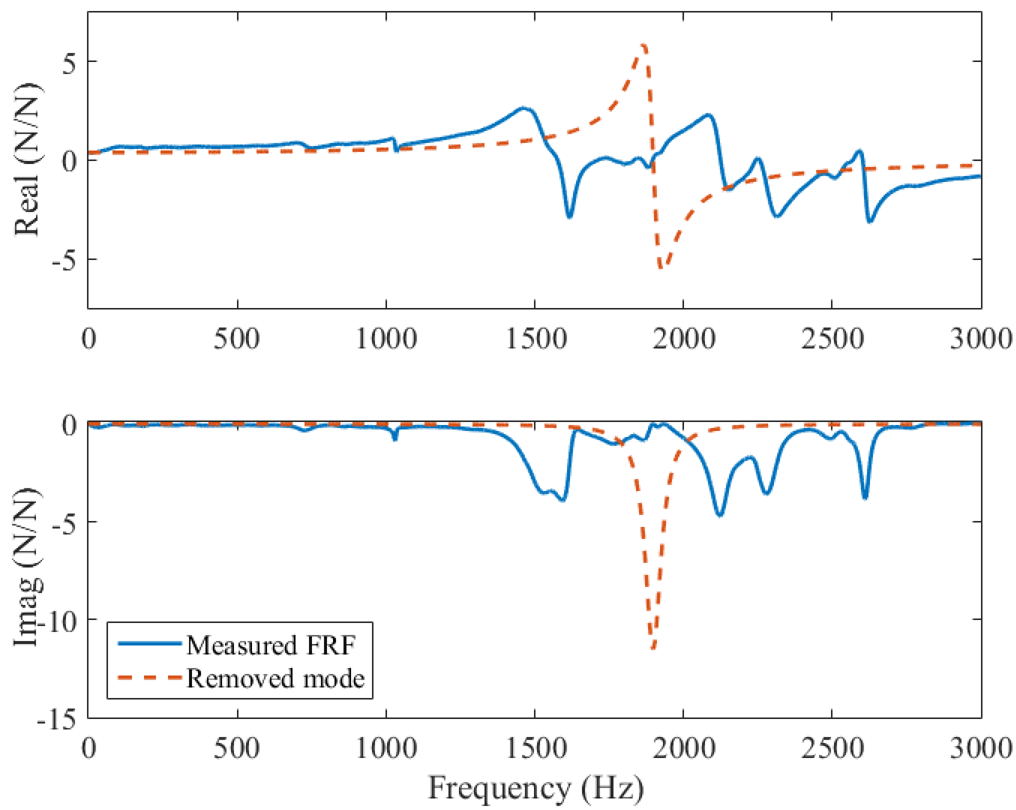

Figure 4.15: The measured force-to-force FRF with the most flexible mode deleted from the response and the removed mode identified by the peak picking method.

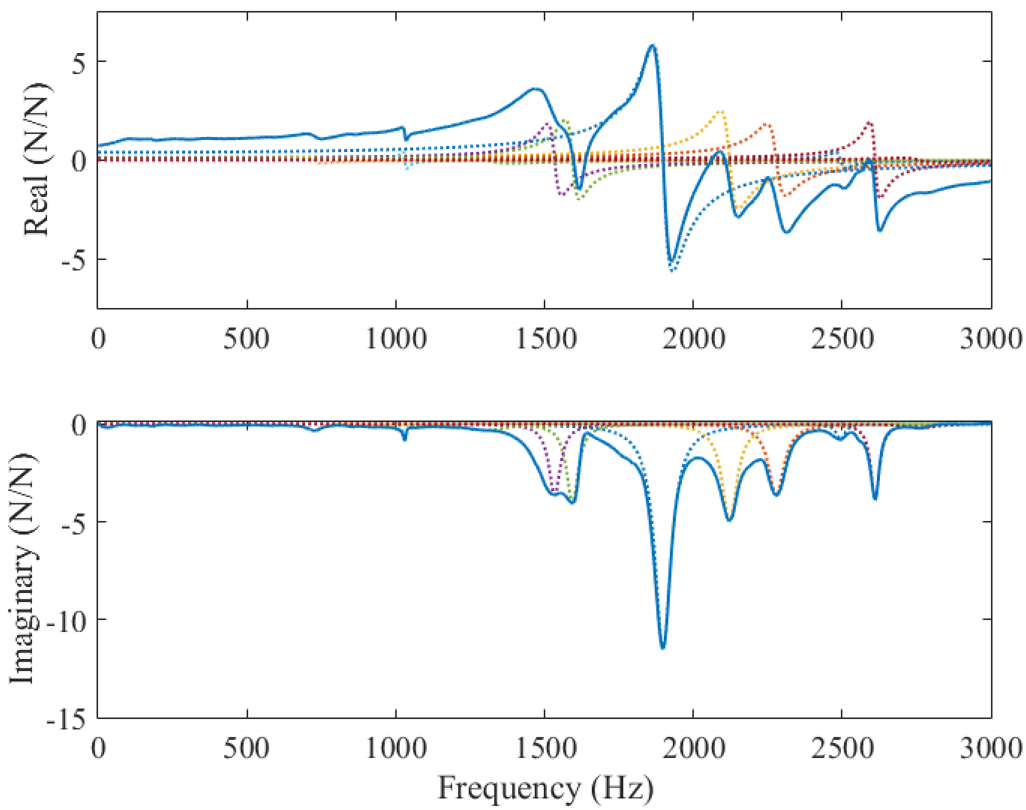

Figure 4.16: The measured FRF and corresponding individual modes identified using the peak picking method.

4.2.2 Optimization for All Modes

Once the modal mass, damping ratio, and natural frequency were identified for all the individual modes as described in the previous step, these values were used to provide an initial estimate for optimizing for the combined effects of all modes simultaneously. The measured and fit FRFs are passed into a nonlinear optimization function. The function builds the combined FRF using the individual modes (which were fit using the peak picking method) and compares it to the measured FRF. An objective function quantifies the difference in the two nonlinear functions and the optimization routine iteratively updates the decision variables (modal parameters) until a set of user-defined convergence criteria are met. The objective function to be minimized is given as:

$$f_i(x) = \begin{Bmatrix} real(FRF) \\ imag(FRF) \end{Bmatrix}_i^{fit} - \begin{Bmatrix} real(FRF) \\ imag(FRF) \end{Bmatrix}_i^{measured} \tag{4.13}$$

where x is the vector of decision variables (modal parameters), and $f_i(x)$ is the difference between the real and imaginary components of the fit and measured FRFs at the ith frequency step. Figure 4.17 shows a comparison between the measured FRF and the fits resulting from the peak picking method and nonlinear optimization.

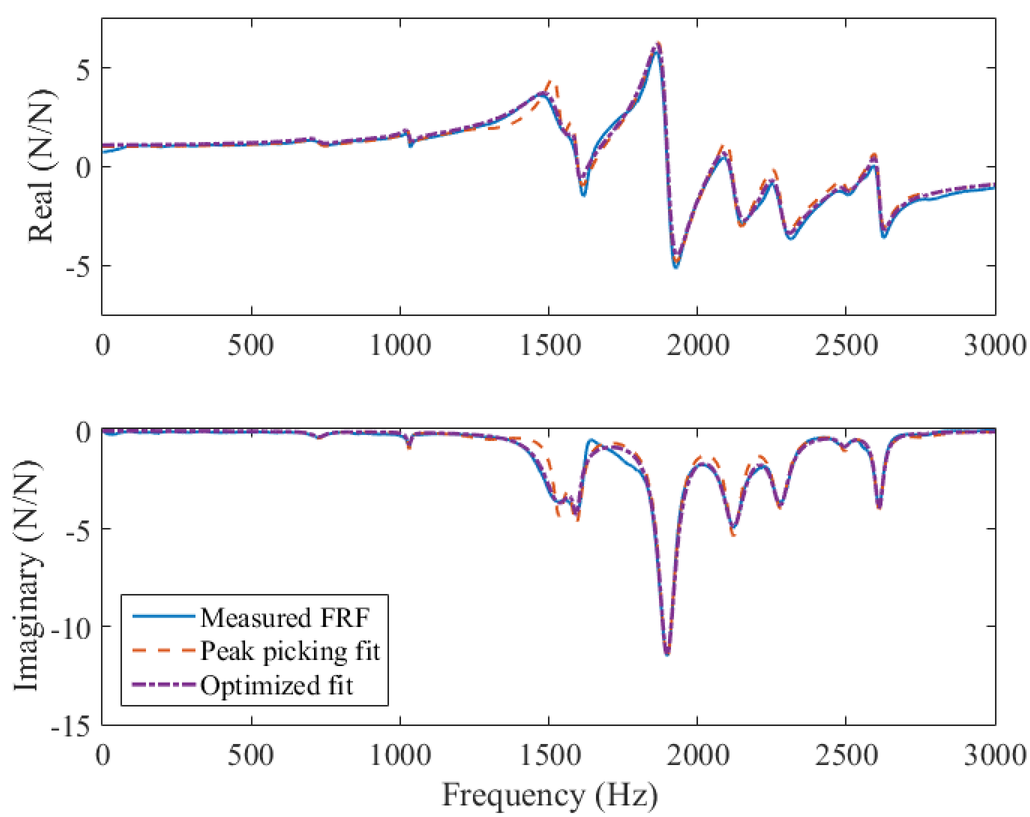

Figure 4.17: A comparison of the measured FRF to the fits resulting from the peak picking method and nonlinear optimization.

CHAPTER 5: NUMERICAL MILLING SIMULATION COMPARISON

To evaluate the amplitude ratio diagrams, comparison to results found in the literature were performed. Two cases of interest in milling have been selected for the study: (1) period-*n* flip instability and (2) helix angle induced islands of instability. Both cases occur during low radial immersion milling.

5.1 Low Radial Immersion Milling

In [43] Govekar *et al.* use the numerical semi-discretization method to identify Hopf and period-2 instabilities during low radial immersion milling. The stability diagram, shown in Figure 5.1, was experimentally verified. A single flute, $8\ mm$ diameter endmill mounted in an HSK40E shrink fit holder with a $96\ mm$ overhang and $45\ °$ helix angle was used for the up milling tests. The $5\ \%$ radial immersion (i.e., $0.4\ mm$ radial depth of cut) provided highly interrupted (i.e., low radial immersion) cutting conditions. The specific cutting force and force angle for the aluminum workpiece-tool combination was determined mechanistically to be $644\ MPa$ and $69.7°$, respectively.

The large length-to-diameter ratio of the cutting tool resulted in a single, dominant vibration mode for which the modal parameters in the x (feed) and y directions are given in Table 5.1. The stability diagram obtained using the semi-discretization method is given in Figure 5.1. It shows that the Hopf instabilities are open curves distributed along the spindle speed axis and period-2 flip instabilities manifest as close curves.

Table 5.1: Cutting tool modal parameters obtained from impact testing.

x (feed) direction		
f_n (Hz)	k (N/m)	ζ
721	4.1×10^5	0.009
y direction		
f_n (Hz)	k (N/m)	ζ
721	4.1×10^5	0.009

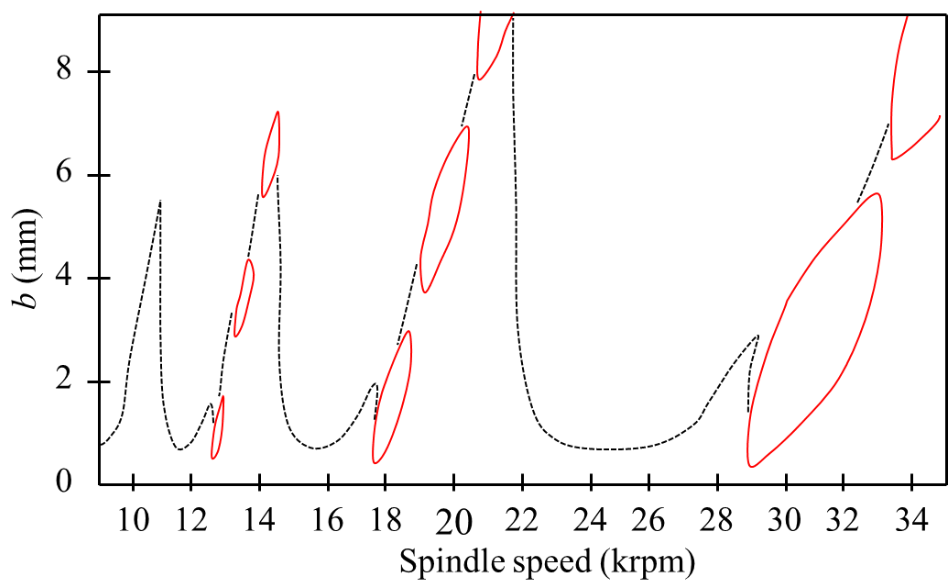

Figure 5.1: Stability lobe diagram with secondary Hopf (dashed) and period-2 (solid) stability boundary redrawn from [43] obtained using the semi-discretization method.

The stability diagram obtained using the amplitude ratio stability metric is given in Figure 5.2. The agreement between the stability diagrams is evident. It is observed that the amplitude ratio diagrams predicts a similar stability boundary between stable and unstable spindle speed-axial depth of cut combinations. Additionally, the regions of period-2 instability are visible.

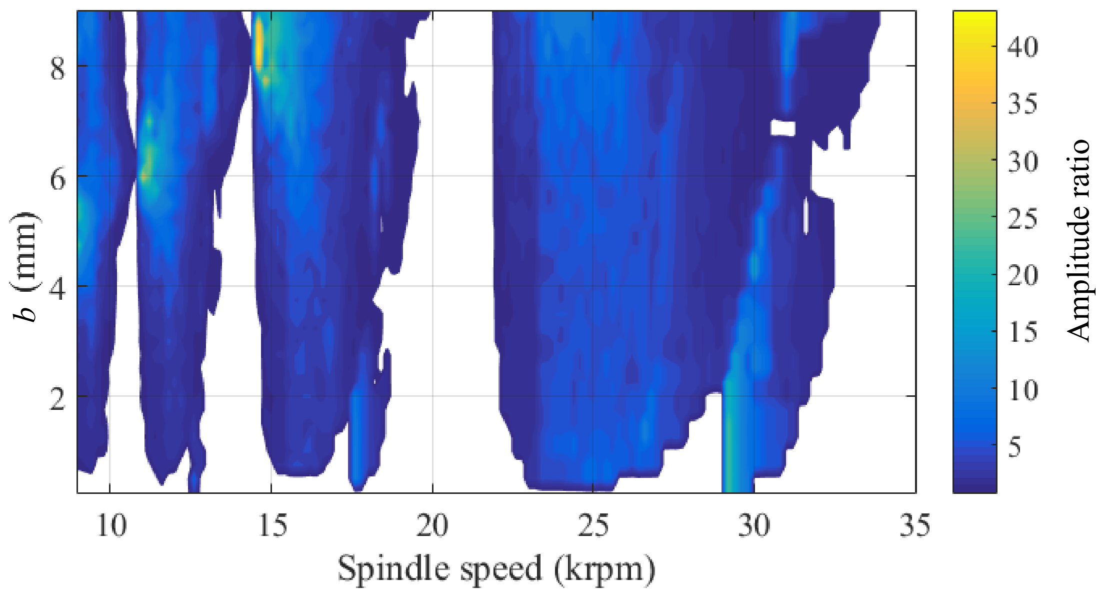

Figure 5.2: Stability lobe diagram with secondary Hopf and period-2 stability boundary using the amplitude ratio method.

5.2 Helix Angle Induced Islands of Instability

In [48] Insperger *et al.* uses the numerical semi-discretization method to show that unstable flip (i.e., period doubling) islands manifest on the milling stability diagram due to the helix angle of the cutting tool. In this numerical study a four flute, 20 mm endmill with various helix angles was used in a down milling configuration. Flexibility in the milling system occurs on the workpiece side in the y direction using a flexure for which modal parameters are given in Table 5.2. The tool is considered quasi-rigid, relative to the flexure, in both the x (feed) and y directions. The radial immersion is 5 % (i.e., 1 mm) and the cutting force coefficients in the tangential and radial directions are 804.3 N/mm^2 and 331 N/mm^2, respectively.

Table 5.2: Modal parameters for the workpiece (flexure) measured using impact testing.

y (feed) direction		
f_n (Hz)	k (N/m)	ζ
319.375	2.16×10^7	0.0196

Milling stability diagrams are generated using the semi-discretization method for tools of different helix angle. Insperger *et al.* define the helical pitch, p, as:

$$p = \frac{D\pi}{N \tan \eta} \tag{5.1}$$

where D is the tool diameter, N is the number of cutting teeth, and η is the helix angle. Milling stability diagrams, generated using the semi-discretization method, for helical pitches of $100\,mm$, $50\,mm$, and $25\,mm$ are given in Figure 5.3. Rather than spindle speed, the horizontal axis is expressed as the ratio of the tooth passing frequency to the natural frequency of the system providing a "normalized spindle speed." As noted by Insperger *et al.* the stability islands are separated by lines where the axial depth of cut is equal to the multiples of the helical pitch.

Figure 5.4 shows the amplitude ratio diagram obtained using the time domain simulation. The agreement of the stability diagrams is evident. The amplitude ratio diagram predicts a similar stability limit between stable and unstable combinations of spindle speed and axial depth of cut. Additionally, the unstable islands of instability due to cutting tool helix angle are apparent.

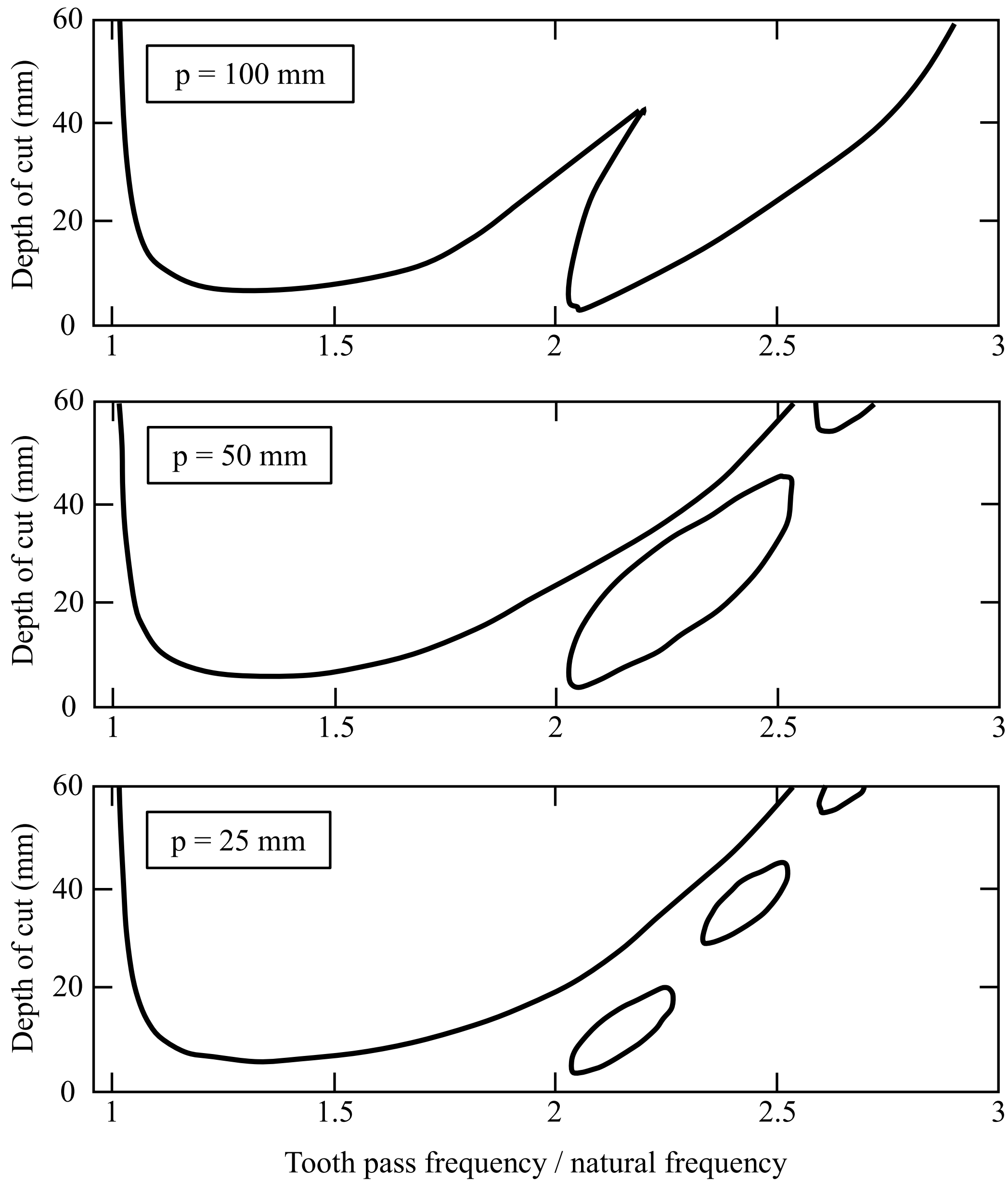

Figure 5.3: Milling stability diagrams for different helical pitches using the semi-discretization method.

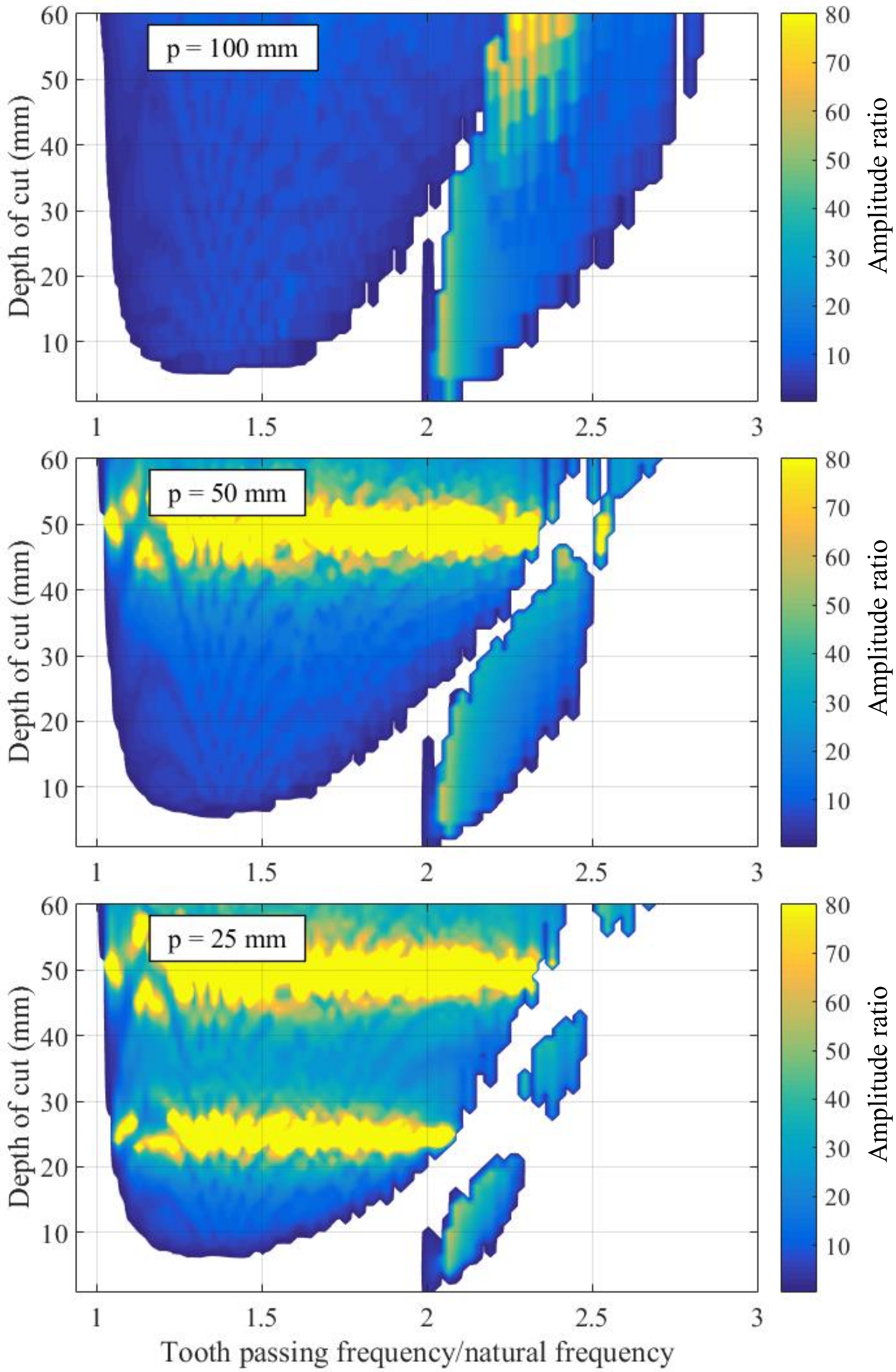

Figure 5.4: Amplitude ratio diagram for different helical pitches using time domain simulation.

CHAPTER 6: EXPERIMENTAL MILLING SIMULATION VALIDATION

The following sections provide a representative example from the experimental validation of the time domain simulation. Predictions and measurements are presented.

6.1 Aluminum Milling Stability Validation

To validate the time domain simulation model, experiments were conducted. The cutting tests were performed on compliant workpieces, shown in Figure 6.1, which simulate near net shape preforms. These compliant workpieces were machined from 6061-T651 aluminum and are composed of two thin-walled structures (ribs) with clamped-clamped-clamped-free (CCCF) boundary conditions. The nominal geometric dimensions of the thin-walled structures, or ribs, are given in Table 6.1.

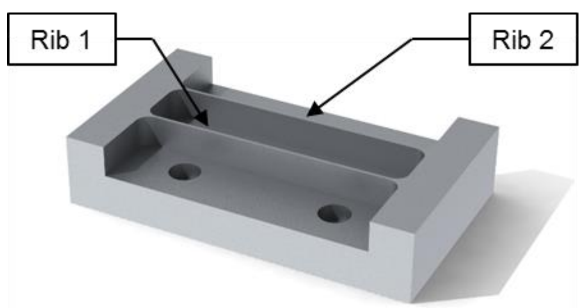

Figure 6.1: Solid model of the flexible workpiece (simulated preform) used for validation testing.

Validation tests were performed on a LeBlond Makino A55 horizontal machining center with a maximum spindle speed of 20 krpm. Cutting forces, measured by a dynamometer (Kistler 9257B), were the primary metric for validating the simulation outputs. The cutting tool used for the validation experiments was a 12.7 mm carbide end mill with two flutes, evenly spaced, and a 30º helix angle. Modal parameters for the tool were obtained via impact testing using an instrumented hammer (PCB 086C04) to provide the excitation force and a low mass accelerometer (PCB 352C23) to record the response. Table 6.2 lists the natural frequency, f_n, modal stiffness, k, and damping ratio, ζ, for the dominant modes in the plane of the cut (i.e., *x*-*y*).

Table 6.1: Nominal geometric dimensions of the flexible ribs.

Length	Height	Thickness
130 mm	15 mm	1.5 mm

Since cutting forces were used as the primary metric by which the simulation model was validated, the workpiece was bolted to a cutting force dynamometer (Kistler 9257B) during impact testing, as shown in Figure 6.2, to properly represent the workpiece dynamics during the validation tests. An instrumented hammer (PCB 084A17) was used to provide the excitation force and the workpiece response was measured using a non-contact laser vibrometer (Polytec OFV-534). Table 6.3 lists the natural frequency, f_n, modal stiffness, k, and damping ratio, ζ, for the two modes in the direction of greatest compliance (i.e., *y* direction).

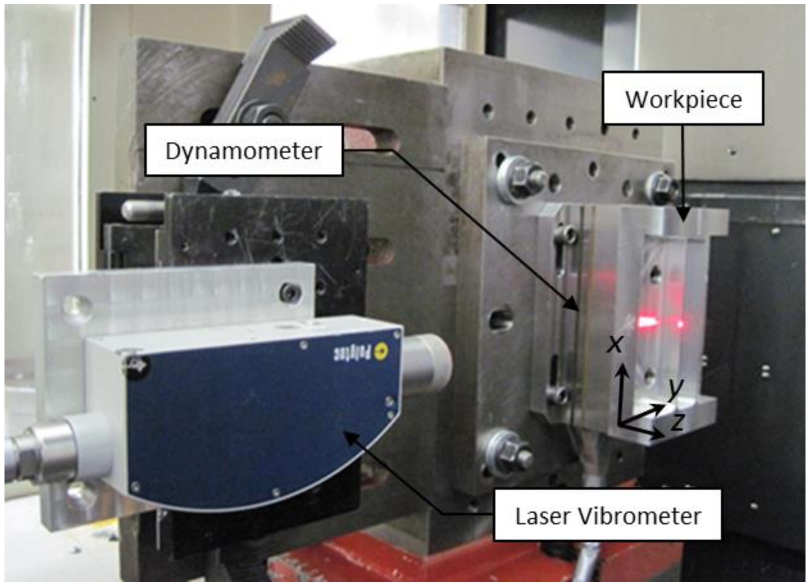

Figure 6.2: Impact testing setup for the compliant workpiece.

Table 6.2: Modal parameters for the cutting tool.

	x direction	
f_n (Hz)	k (N/m)	ζ
2265	3.11×10^7	0.034
	y direction	
f_n (Hz)	k (N/m)	ζ
2254	3.09×10^7	0.027

The specific force coefficients used to calibrate the mechanistic force model applied in the time domain simulation were calculated using a nonlinear optimization method similar to the technique described in [78]. This method fits a set of simulated, instantaneous cutting forces to a set of measured, instantaneous cutting forces by iteratively updating the specific force coefficients until the convergence criteria is met. The cutting force coefficients may be considered to be a function of not only the cutting tool geometry and workpiece material, but also machining parameters. Cutting tests, for determining the specific force coefficients, were performed at 8% radial immersion, 3 mm axial depth of cut, 8000 rpm spindle speed, and a commanded feed rate of 0.1 mm/tooth. Table 6.4 lists the six specific force coefficients used in the simulation.

Table 6.3: Modal parameters for ribs 1 and 2.

	Mode	$f_n\ (Hz)$	$k\ (N/m)$	ζ
Rib1	1	5837	1.59×10^6	0.0007
	2	7787	4.17×10^6	0.0008
	Mode	$f_n\ (Hz)$	$k\ (N/m)$	ζ
Rib 2	1	5832	1.39×10^6	0.0007
	2	7789	2.12×10^6	0.0024

Table 6.4: Cutting force coefficients used in the time domain simulation.

Cutting force coefficients		
$k_{tc}\ (N/mm^2)$	$k_{rc}\ (N/mm^2)$	$k_{ac}(N/mm^2)$
1119	322	305
Edge force coefficients		
$k_{te}\ (N/mm)$	$k_{re}\ (N/mm)$	$k_{ae}\ (N/mm)$
2	0	0

The simulations were performed at 2% radial immersion in a down milling configuration with a commanded feed rate of 0.1 mm/tooth. Flute-to-flute runout was specified as 3 µm.

The PTP force diagrams for validation testing were generated over a spindle speed range from 7000 rpm to 9000 rpm at increments of 50 rpm and the axial depth of cut ranged from 0 mm to 0.6 mm in increments of 0.1 mm. Computation time was approximately 5 minutes for each simulation. The PTP force diagram for rib 1, shown in Figure 6.3, was used to select a spindle speed-axial depth of cut combination at which to perform a validation test. A stable cut, as predicted by the simulation, was chosen. Similarly, an unstable test cut was chosen for rib 2; see Figure 6.4. A comparison of the simulated and measured, instantaneous cutting forces are provided in the following section.

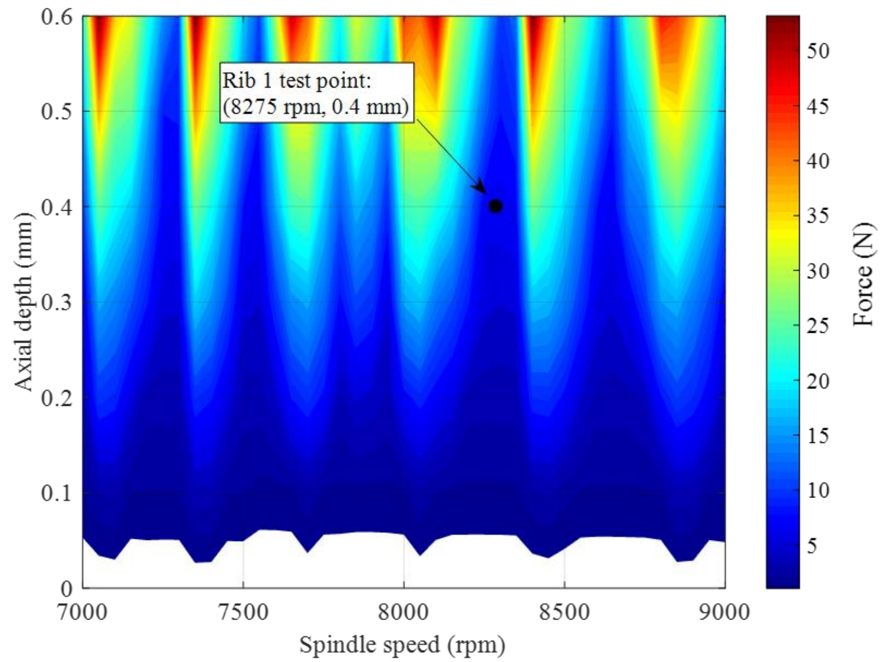

Figure 6.3: PTP force diagram indicating the selected stable test point for rib 1.

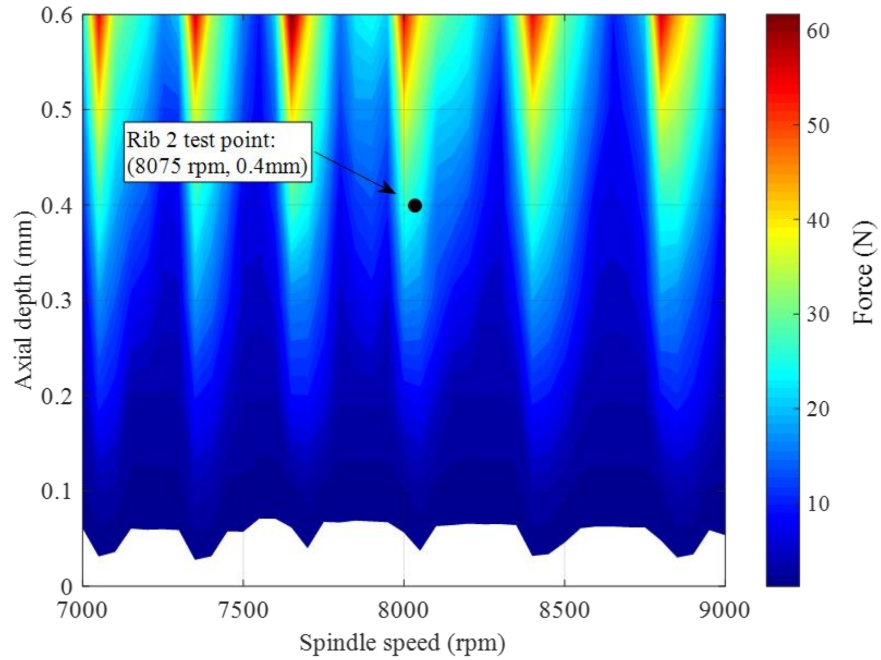

Figure 6.4. PTP force diagram indicating the selected unstable test point for rib 2.

6.1.1 Experiment Results

In this section, the simulated and measured cutting forces (*x* and *y* directions) for the stable and unstable validation tests are presented. The experimental results are shown in both the time and frequency domains. A restatement of the coordinate system definition is provided in Figure 6.5.

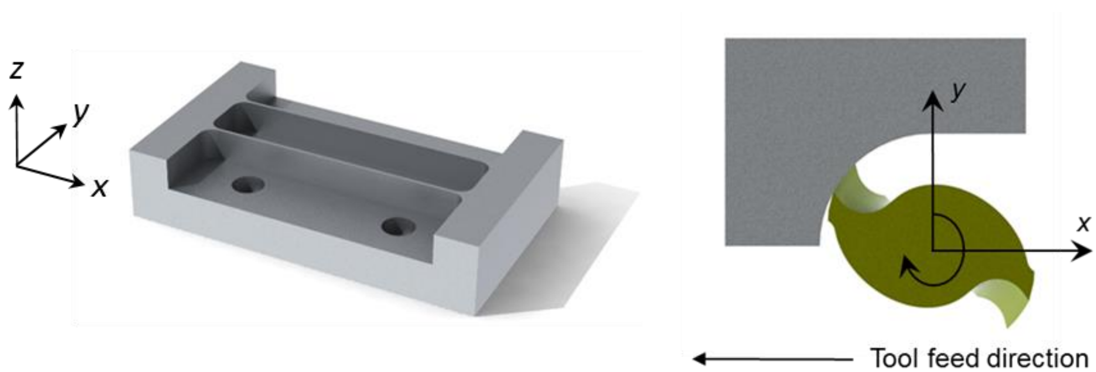

Figure 6.5: Coordinate system definition.

The simulated and measured *x*-direction cutting forces for the stable validation test, which was performed at a spindle speed of 8275 rpm and an axial depth of cut of 0.4 mm, are shown in Figure 6.6. It is observed that the measured and simulated cutting forces are in good agreement and that the variation in the cutting force from one tooth engagement to the next, due to flute-to-flute runout, is also captured by the time domain simulation.

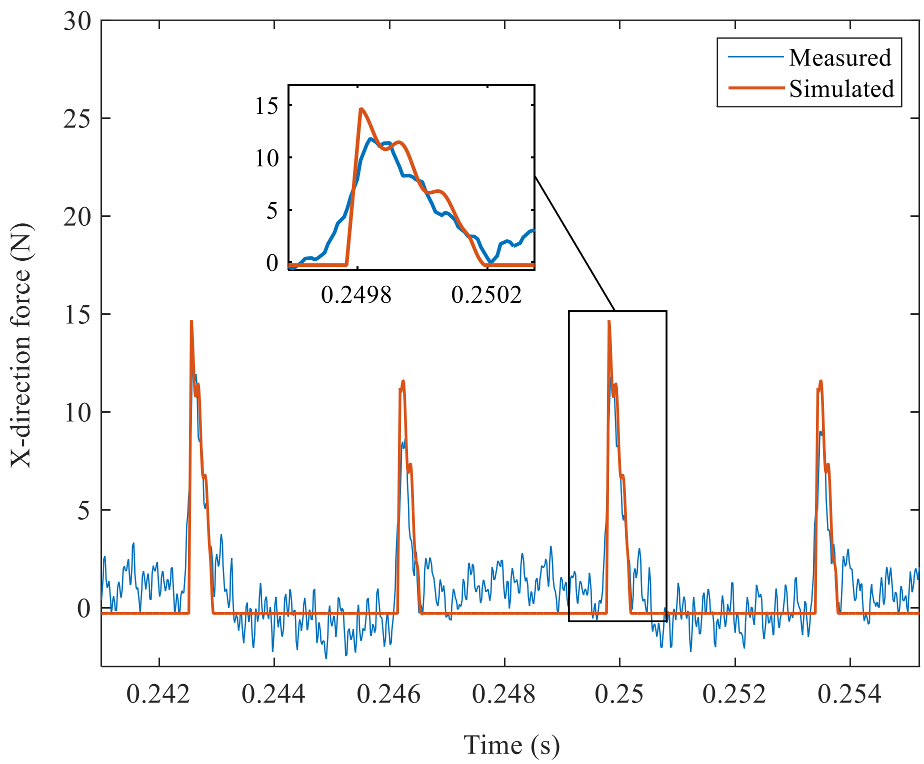

Figure 6.6: Measured and simulated *x*-direction cutting forces for the rib 1 test point (stable case) shown for two cutter revolutions.

The frequency content of the *x*-direction cutting force, computed using the fast Fourier transform (FFT) of the data in Figure 6.6, is displayed in Figure 6.7. It is observed that the dominant frequencies are the tooth passing frequency, 276 Hz, and the runout frequency, 138 Hz, as well as their integer multiples (i.e., harmonics). Some amplification of the frequency content near the rib's natural frequencies is also evident.

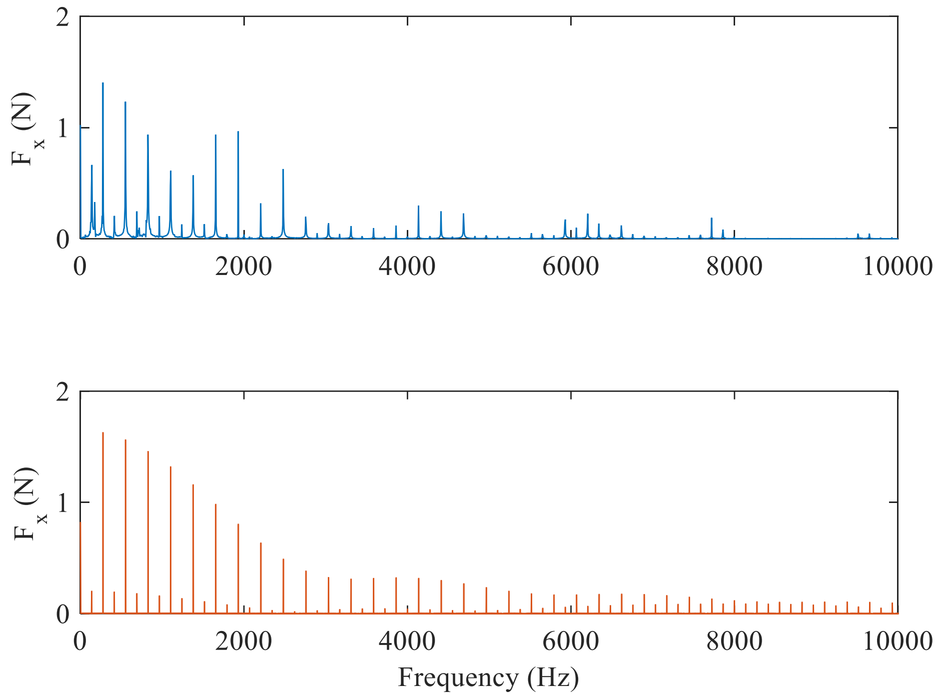

Figure 6.7. Frequency content of the measured (top) and simulated (bottom) *x*-direction cutting forces for the rib 1 test point (stable case).

The measured and simulated *y*-direction cutting forces, shown in Figure 6.8, also exhibit good agreement. The frequency content matches as well; see Figure 6.9. A magnified image of the stable milling cut is provided in Figure 6.10. The tool feed marks are clearly visible and chatter is not observed.

Discrepancies between the measured and simulated cutting forces are primarily due to the limited bandwidth of the dynamometer. Because the dynamometer is a dynamic system with its own characteristic frequency response, the measured cutting forces become distorted as the frequency content of the signal approaches the dynamometer's natural frequency. Higher frequency content is attenuated due to the limited bandwidth and as a result the dynamometer is unable to resolve the sharp peaks in the cutting force. Additionally, the non-zero forces between the individual cutting flute engagements is due to "ringing" or free vibration of the dynamometer-workpiece system.

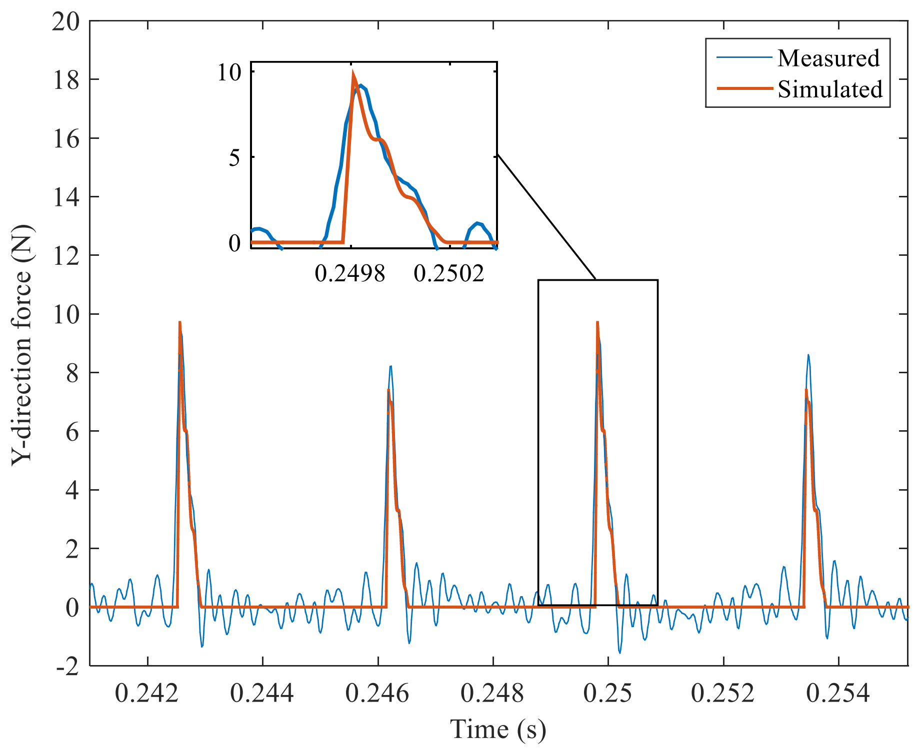

Figure 6.8. Measured and simulated *y*-direction cutting forces for the rib 1 test point (stable case) shown for two cutter revolutions.

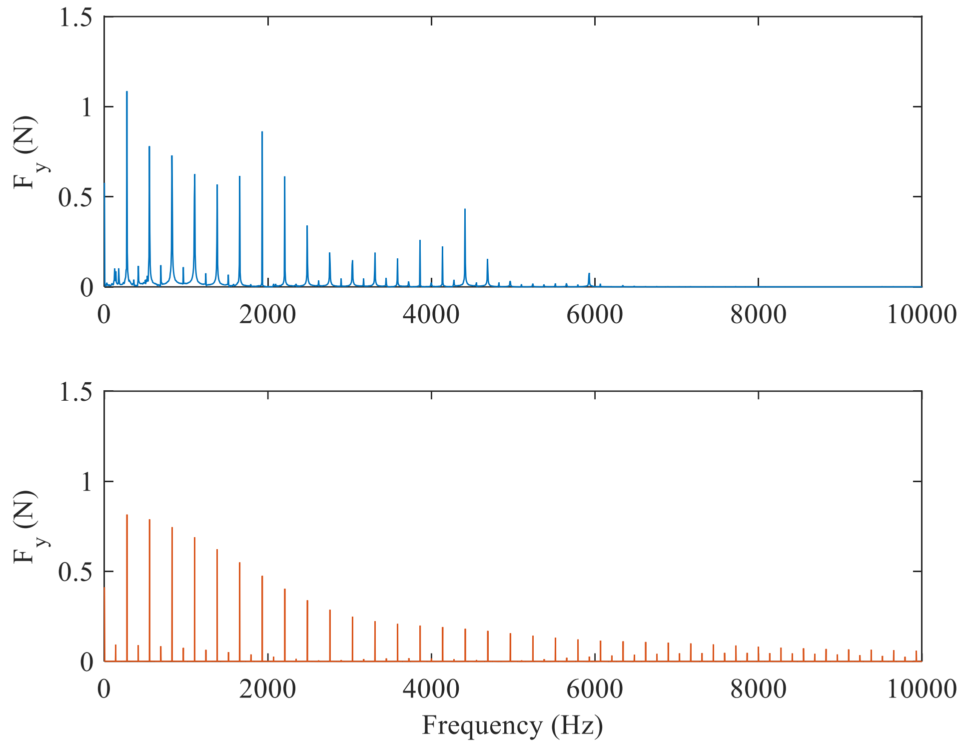

Figure 6.9. Frequency content of the measured (top) and simulated (bottom) *y*-direction cutting forces for the rib 1 test point (stable case).

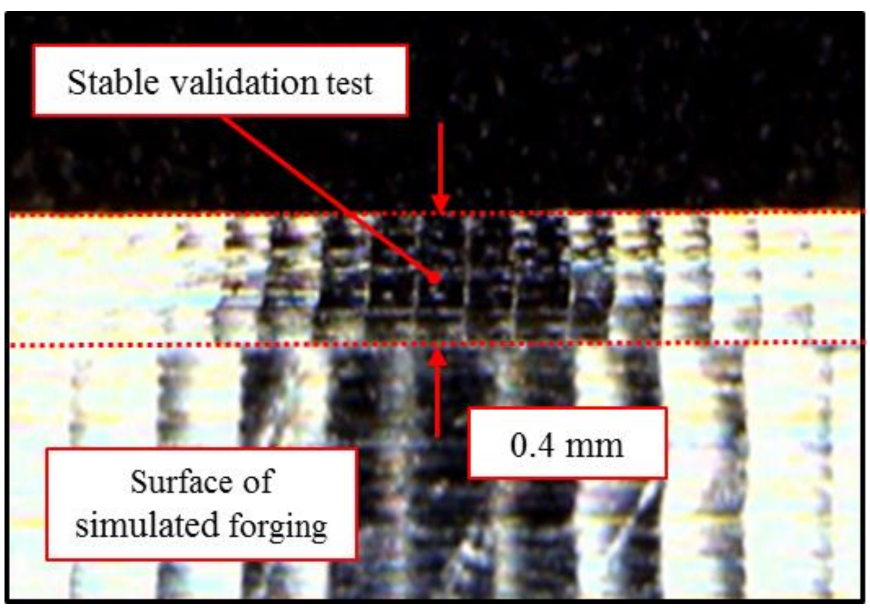

Figure 6.10. Surface finish of the rib 1 test point (stable case).

The simulated and measured *y*-direction cutting forces for the unstable validation test, which was performed at a spindle speed of 8075 rpm and an axial depth of cut of 0.4 mm, are presented in Figure 6.11. As with the stable case, good agreement in the peak force is observed. However, the measured forces exhibit a high frequency component when the tool is not engaged in the cut which is not found in the simulated force signal. As discussed previously, the high frequency component between the individual cutting flute engagements is due to “ringing” or free vibration of the dynamometer-workpiece system.

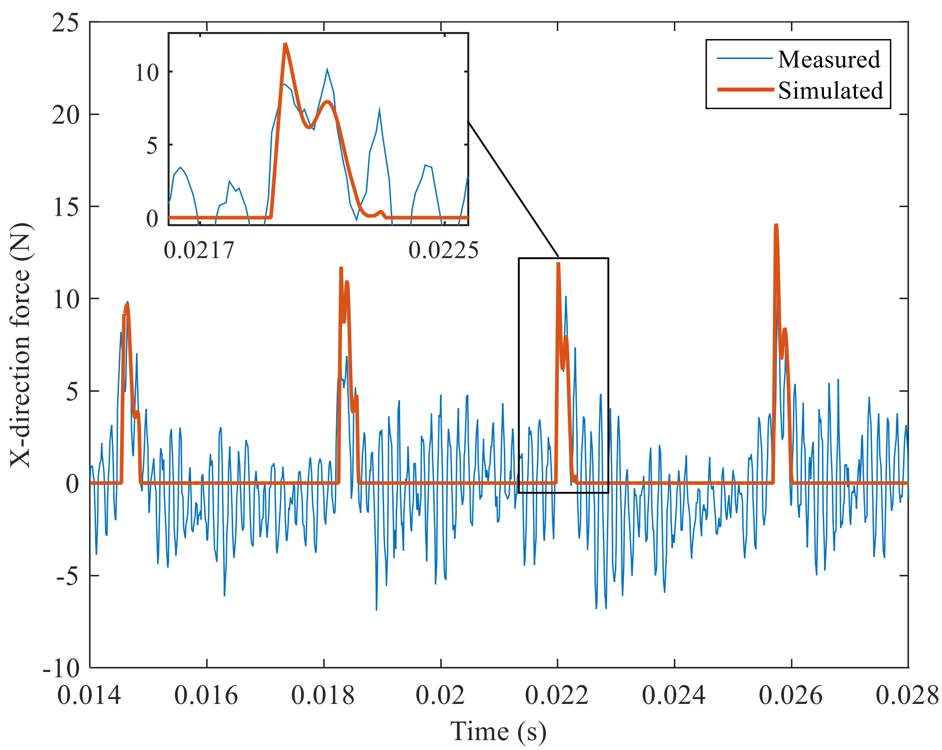

Figure 6.11. Measured and simulated *x*-direction cutting forces for the rib 2 test point (unstable case) shown for two cutter revolutions.

The frequency content of the *x*-direction cutting forces is provided in Figure 6.12. Both the measured and simulated forces exhibit frequency content at the tooth passing frequency (269 Hz), runout frequency (134.5 Hz), and harmonics as well as a chatter frequency of 6935 Hz. Larger amplitudes for the experimental content in this frequency range explains the difference in the time-domain signals.

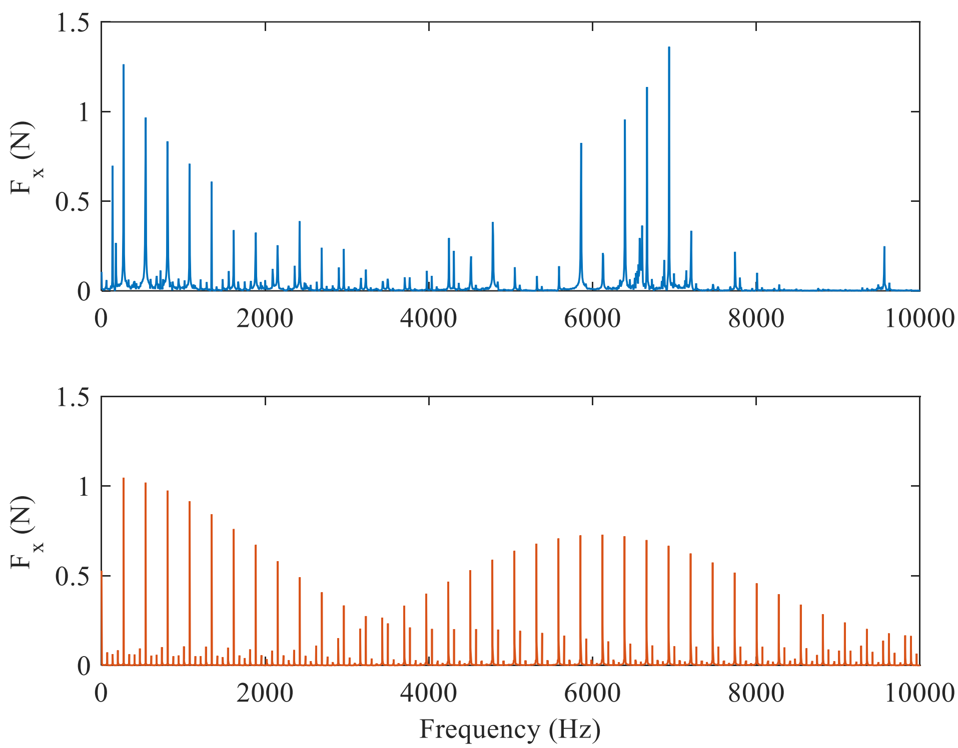

Figure 6.12. Frequency content of the measured (top) and simulated (bottom) *x*-direction cutting forces for the rib 2 test point (unstable case).

The measured and simulated *y*-direction cutting forces, shown in Figure 6.13 and Figure 6.14, present similar results. A magnified image of the surface finish is provided in Figure 6.15. Chatter marks, which have a high spatial frequency, are observed.

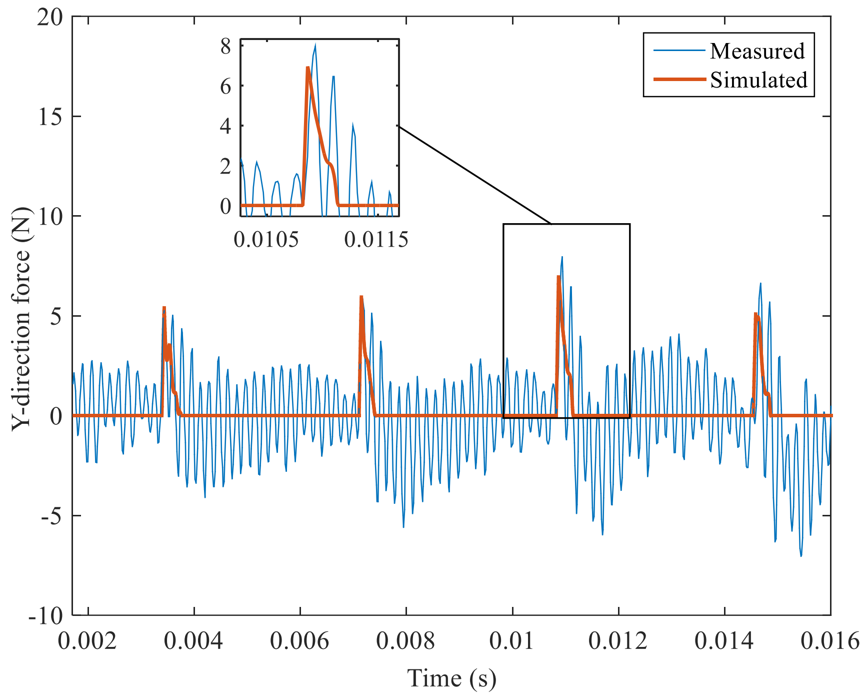

Figure 6.13. Measured and simulated *y*-direction cutting forces for the rib 2 test point (unstable case) shown for two cutter revolutions.

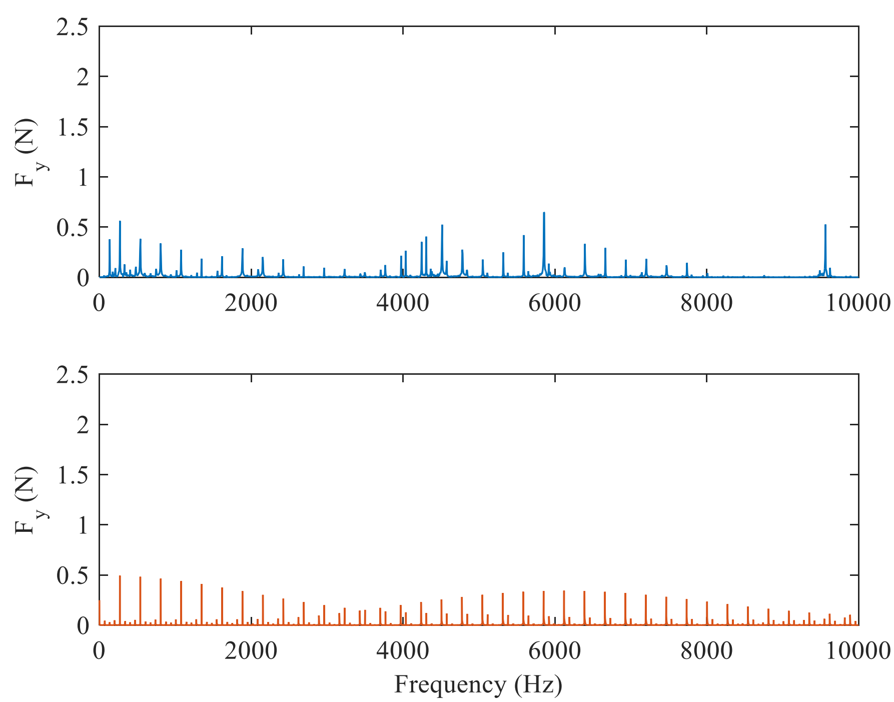

Figure 6.14. Frequency content of the measured (top) and simulated (bottom) *y*-direction cutting forces for the rib 2 test point (unstable case).

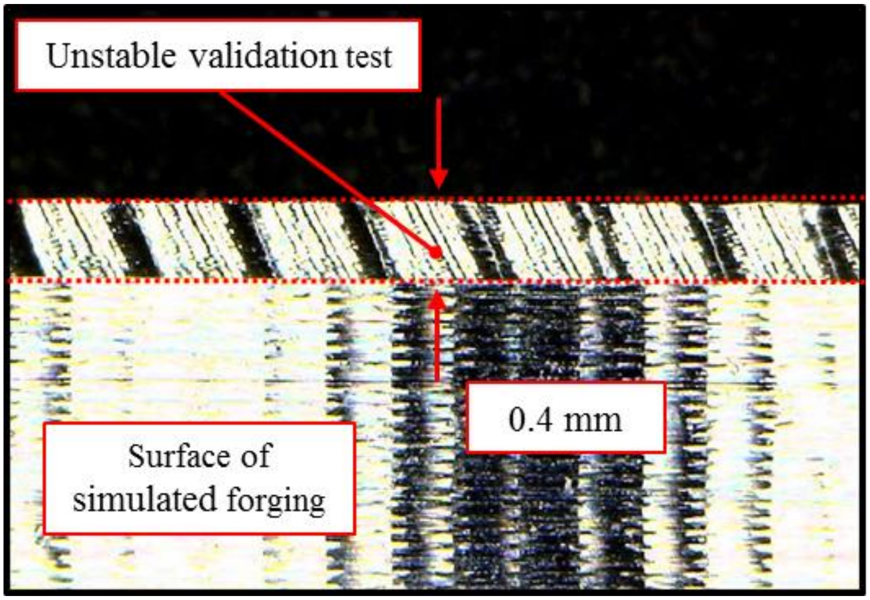

Figure 6.15. Surface finish of the rib 2 test point (unstable case).

6.2 Titanium Milling Stability Validation

Cutting tests were also performed on compliant titanium alloy (i.e., Ti6Al4V) workpieces; see Figure 6.16. These compliant workpieces, which simulate near net shape preforms, are composed of two thin wall structures with clamped-clamped-clamped-free (CCCF) boundary conditions. The nominal geometric dimensions of the thin-walled structures, or ribs, are given in Table 6.5. During the cutting tests, the nominal rib thickness was reduced from 4 mm to 2 mm in 0.5 mm increments by a series of peripheral milling operations.

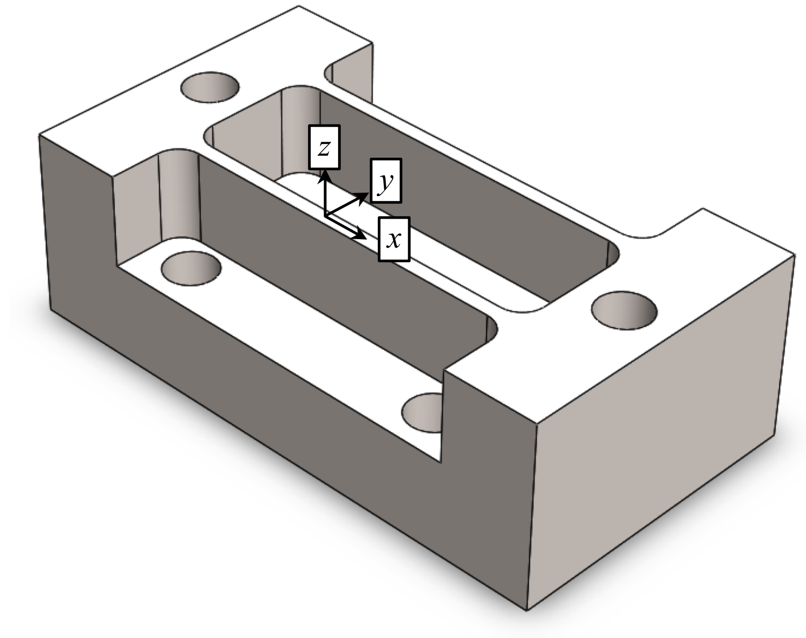

Figure 6.16: Solid model of the flexible workpiece (simulated preform) used for validation testing.

Validation tests were performed on a Haas TM1 vertical machining center with a maximum spindle speed of 4000 rpm. Cutting forces, measured by a dynamometer (Kistler 9257B), and workpiece velocity, measured by a laser vibrometer (Polytec OFV-534), were the primary metrics for validating the simulation outputs. Minimum quantity lubrication (MQL) (i.e., mist coolant) was used during the test cuts. The cutting tool used for the validation experiments was a 19.05 mm carbide end mill with two flutes, evenly spaced, and a 30° helix angle. Modal parameters for the tool were obtained via impact testing using an instrumented hammer (PCB 086C04) to provide the excitation force and a low mass accelerometer (PCB 352C23) to record the response. Table 6.10 lists the natural frequency, f_n, modal stiffness, k, and damping ratio, ζ, for the dominant modes in the plane of the cut (i.e., x-y).

Table 6.5: Nominal geometric dimensions of the flexible ribs.

Length	Height	Thickness
100 mm	24 mm	2 - 4 mm

The workpiece was bolted to a cutting force dynamometer (Kistler 9257B) during impact testing, as shown in Figure 6.17, to properly represent the workpiece dynamics during the validation tests. An instrumented hammer (PCB 084A17) was used to provide the excitation force and the workpiece response was measured using a non-contact laser vibrometer (Polytec OFV-534). The measurement was performed at the top, center (i.e., the location of minimum stiffness) of the flexible, thin wall. Table 6.7 lists the natural frequency, f_n, modal stiffness, k, and damping ratio, ζ, for the first two bending modes in the direction of greatest compliance (i.e., y direction) for each rib thickness.

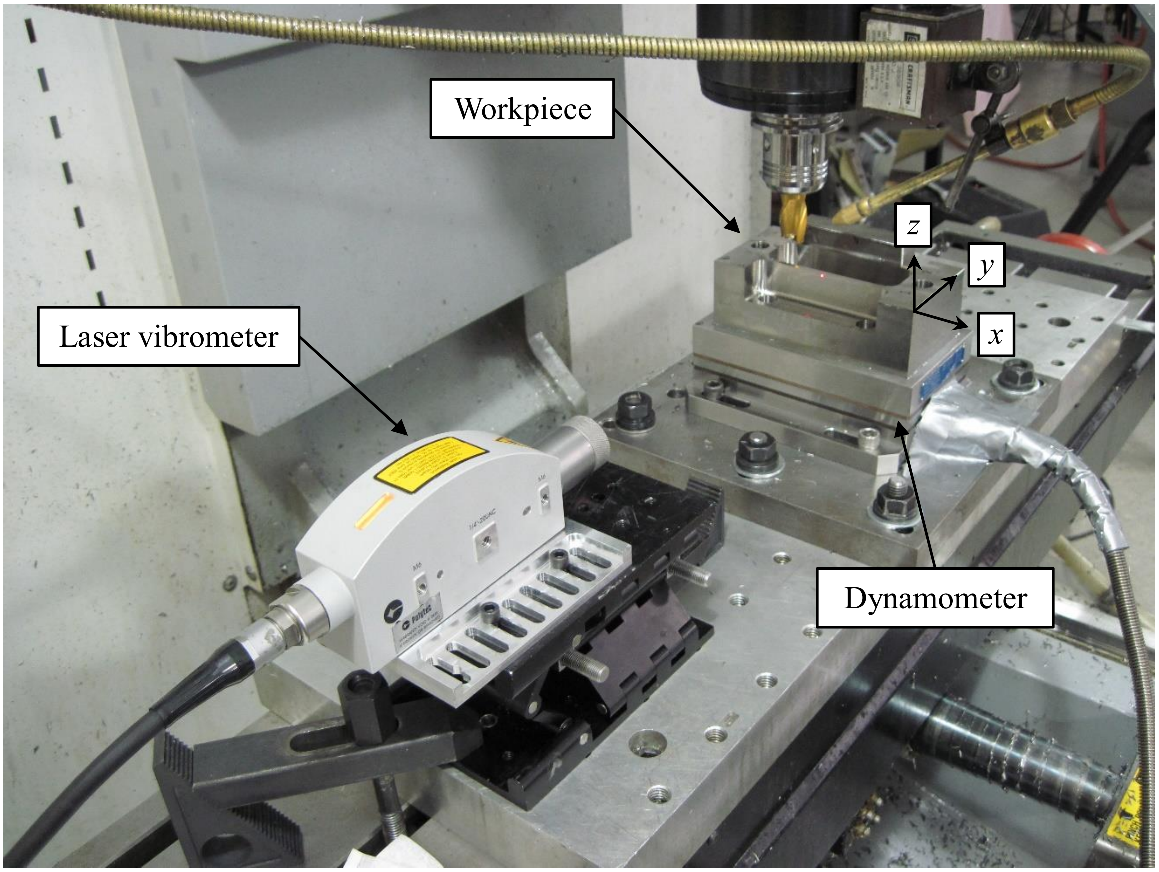

Figure 6.17: Experimental setup for the compliant workpiece.

Table 6.6: Modal parameters for the cutting tool.

	x direction	
f_n (Hz)	k (N/m)	ζ
1029	4.3×10^7	0.0685
	y direction	
f_n (Hz)	k (N/m)	ζ
1161	6.6×10^7	0.0483

The specific force coefficients used to calibrate the mechanistic force model applied in the time domain simulation were calculated using a nonlinear optimization method similar to the technique described in [78]. This method fits a set of simulated, instantaneous cutting forces to a set of measured, instantaneous cutting forces by iteratively updating the specific force coefficients until the convergence criteria is met. The cutting force coefficients may be considered to be a function of not only the cutting tool geometry and workpiece material, but also machining parameters. Cutting tests, for determining the specific force coefficients, were performed at 2.6% radial immersion, 5 mm axial depth of cut, 1000 rpm spindle speed, and a commanded feed rate of $0.1\ \mathrm{mm/tooth}$. Table 6.8 lists the six specific force coefficients used in the simulation.

Table 6.7: Modal parameters of the compliant workpiece's first bending mode for different rib thicknesses.

Rib thickness (mm)	Mode number	f_n (Hz)	k (N/m)	ζ
4.0	1	7391	1.2×10^7	0.0010
	2	16758	8.6×10^7	0.0024
3.5	1	6628	7.9×10^6	0.0088
	2	14637	4.4×10^7	0.0080
3.0	1	5787	4.8×10^6	0.0020
	2	13002	3.0×10^7	0.0019
2.5	1	4956	2.8×10^6	0.0012
	2	11125	2.1×10^7	0.0012
2.0	1	4071	1.4×10^6	0.0011
	2	9164	9.7×10^6	0.0006

Table 6.8: Cutting force coefficients used in the time domain simulation.

Cutting force coefficients		
$k_{tc}\ (N/mm^2)$	$k_{rc}\ (N/mm^2)$	$k_{ac}(N/mm^2)$
2076	918	895
Edge force coefficients		
$k_{te}\ (N/mm)$	$k_{re}\ (N/mm)$	$k_{ae}\ (N/mm)$
8	18	-4

The time domain simulations were performed at 2.6% radial immersion (i.e., 0.5 mm radial depth of cut) in a down milling configuration with a commanded feed rate of 0.1 mm/tooth, a spindle speed of 1000 rpm, and an axial depth of cut of 5 mm. Flute-to-flute runout was specified as 17.5 μm.

6.2.1 Experiment Results

In this section, the simulated and measured cutting forces (x and y directions) for the validation tests are presented. The experimental results are shown in both the time and frequency domains. For brevity, only the results (i.e., cutting forces and workpiece velocity) for the 4 mm and 2 mm thick ribs are shown. The results for the 3.5 mm, 3 mm, and 2.5 mm thick ribs are provided as supplementary evidence in APPENDIX B.1.

The simulated and measured cutting forces in the x, y, and z directions are given in both time and frequency domains for the 4 mm thick rib in Figure 6.18, Figure 6.19, and Figure 6.20, respectively. The variation in cutting forces between adjacent flute engagements is due to flute-to-flute runout. The maximum difference in peak cutting force for all three directions was approximately 7.3 %. The tooth passing frequency (33.3 Hz), runout frequency (16.7 Hz), and their harmonics are evident in the signal. No chatter frequency is observed.

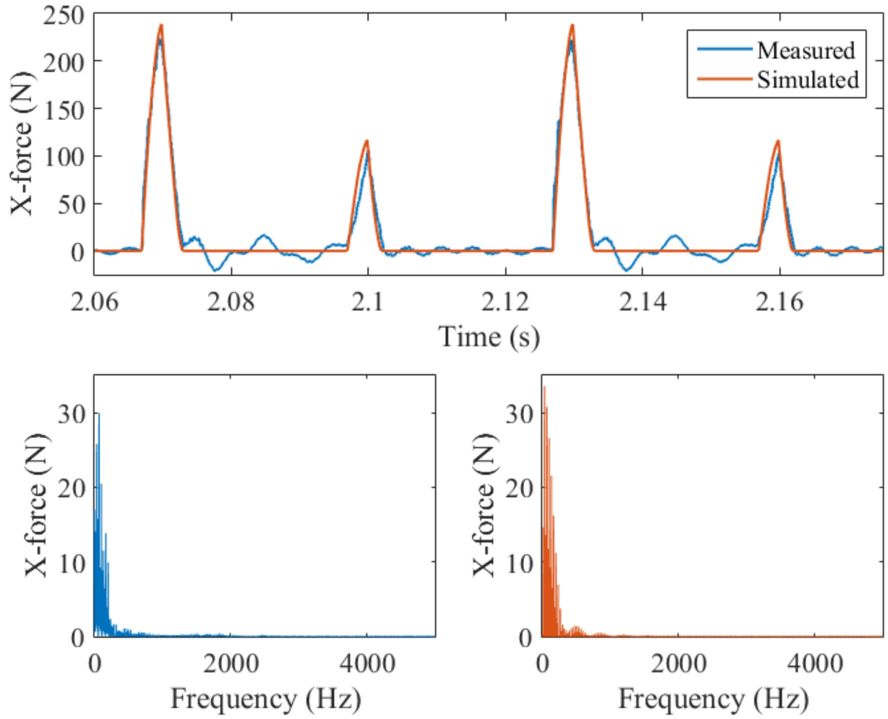

Figure 6.18: Measured and simulated x direction cutting force shown in the time and frequency domains for the 4 mm thick rib.

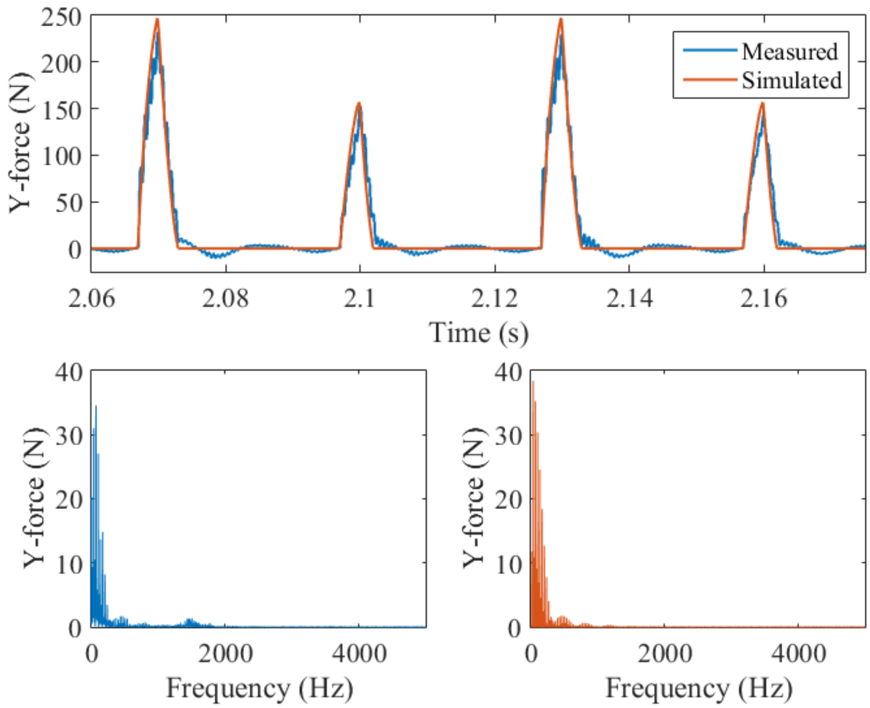

Figure 6.19: Measured and simulated y direction cutting force shown in the time and frequency domains for the 4 mm thick rib.

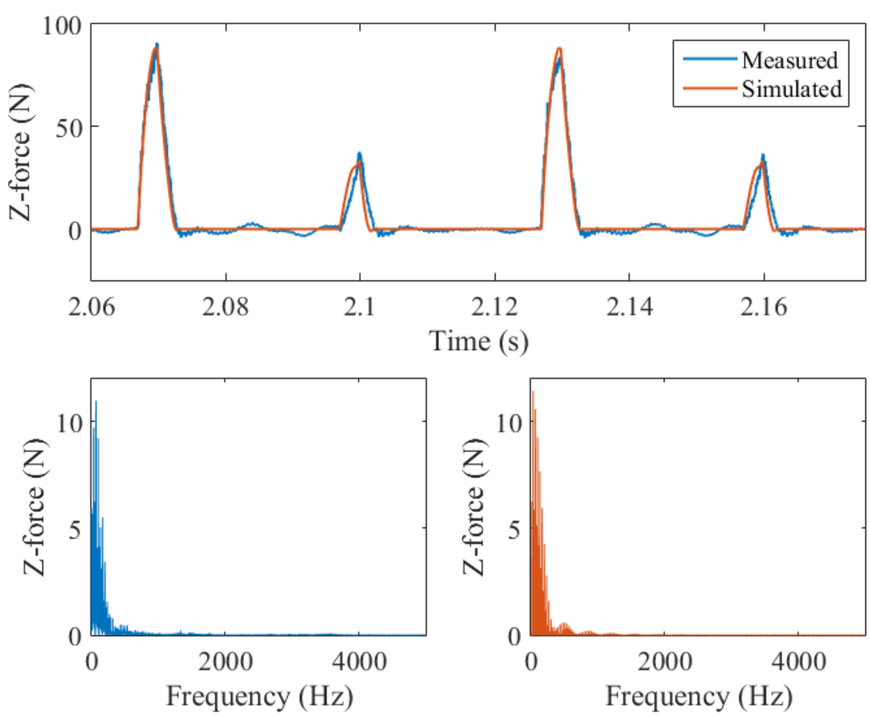

Figure 6.20: Measured and simulated z direction cutting force shown in the time and frequency domains for the 4 mm thick rib.

The measured and simulated workpiece velocity in the y direction are given in Figure 6.21. The time domain signal is shown for one rotation of the cutting tool. The engagement of each cutting tooth is evident as well as the free vibration response occurring between the cutting tooth engagements. Aside from the tooth passing frequency, runout frequency, and their harmonics, the frequency domain signal also reveals a quasi-chatter frequency of $7417\ Hz$ which corresponds to the first vibration mode of the workpiece ($7391\ Hz$).

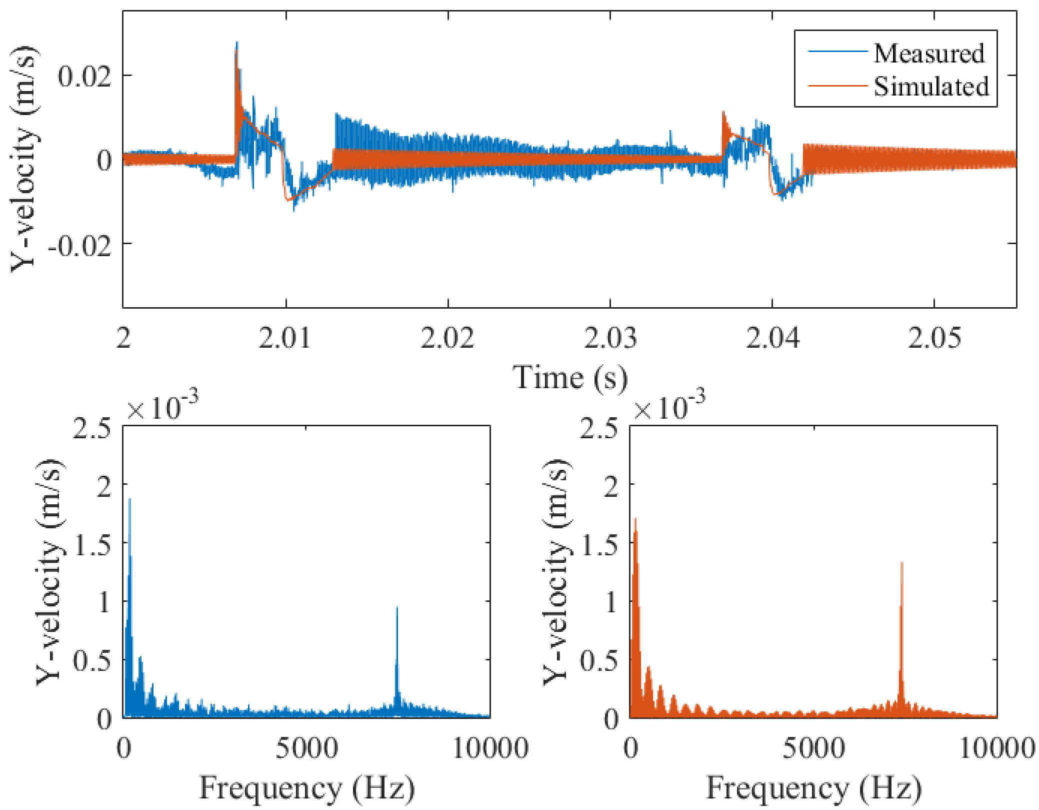

Figure 6.21: Measured and simulated y direction workpiece velocity shown in the time and frequency domains for the 4 mm thick rib.

The simulated and measured cutting forces in the x, y, and z directions are given in both time and frequency domains for the $2\ mm$ thick rib in Figure 6.22, Figure 6.23, and Figure 6.24, respectively. The variation in cutting forces between adjacent flute engagements is due to flute-to-flute runout. The maximum difference in peak cutting force for all three directions was approximately $27.1\ \%$. The tooth passing frequency ($33.3\ Hz$), runout frequency ($16.7\ Hz$), and their harmonics are evident in the signal. No chatter frequency is observed.

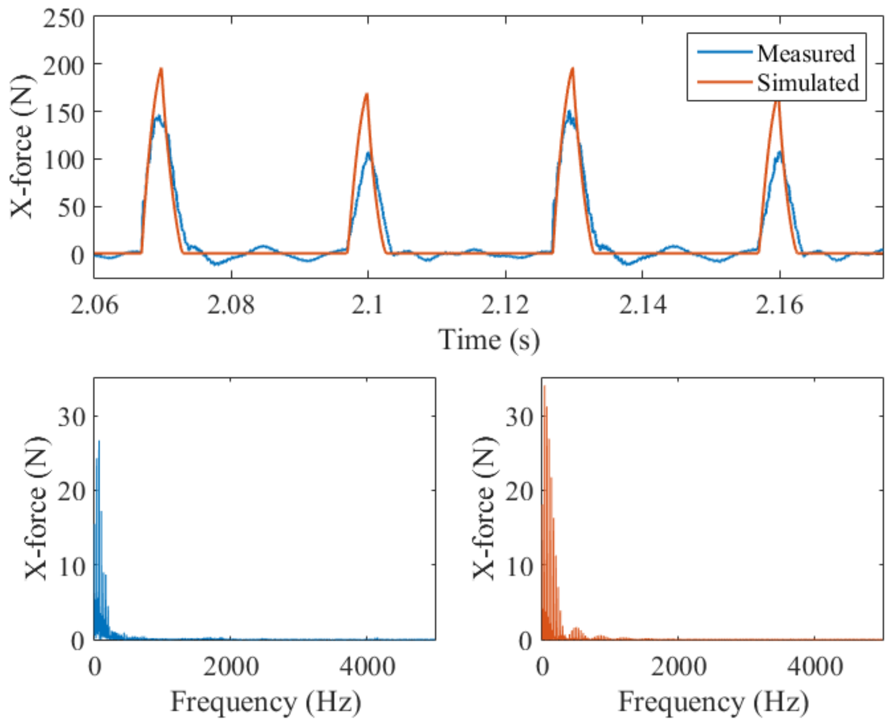

Figure 6.22: Measured and simulated x direction cutting force shown in the time and frequency domains for the $2\ mm$ thick rib.

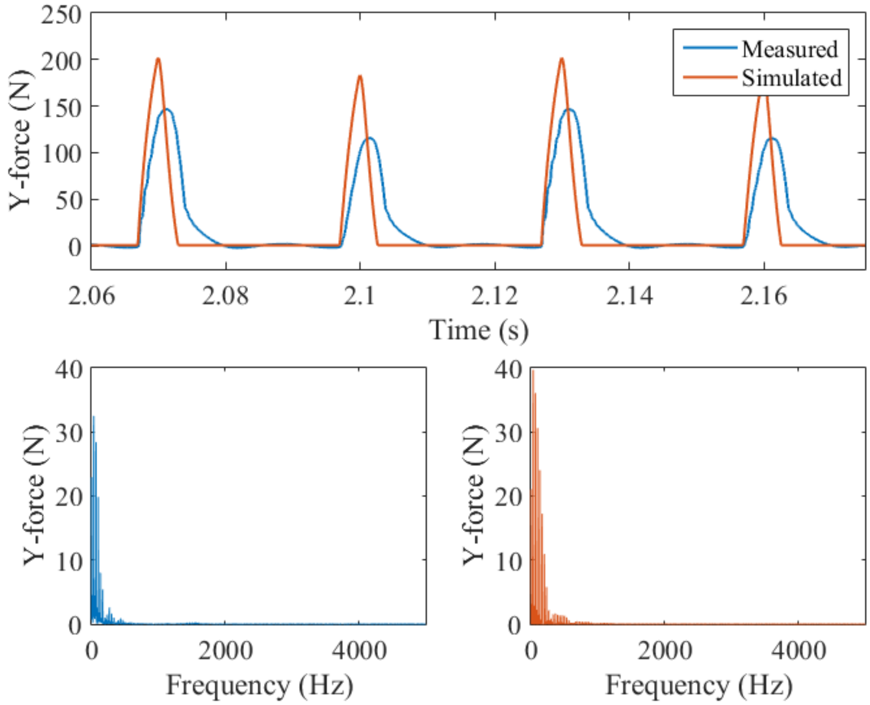

Figure 6.23: Measured and simulated y direction cutting force shown in the time and frequency domains for the 2 mm thick rib.

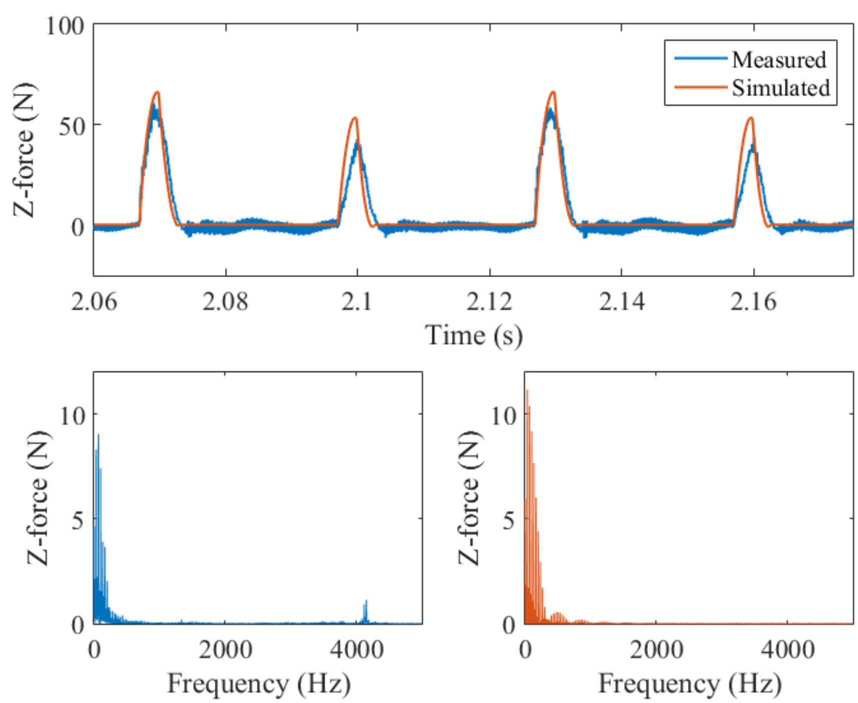

Figure 6.24: Measured and simulated z direction cutting force shown in the time and frequency domains for the 2 mm thick rib.

The measured and simulated workpiece velocity in the y direction are given in Figure 6.25. The time domain signal is shown for one rotation of the cutting tool. The engagement of each cutting tooth is evident as well as the free vibration response occurring between the cutting tooth engagements. Aside from the tooth passing frequency, runout frequency, and their harmonics, the frequency domain signal also reveals quasi-chatter frequencies of 4083 Hz and 9183 Hz which correspond to the first two vibration modes of the workpiece (4071 Hz and 9164 Hz).

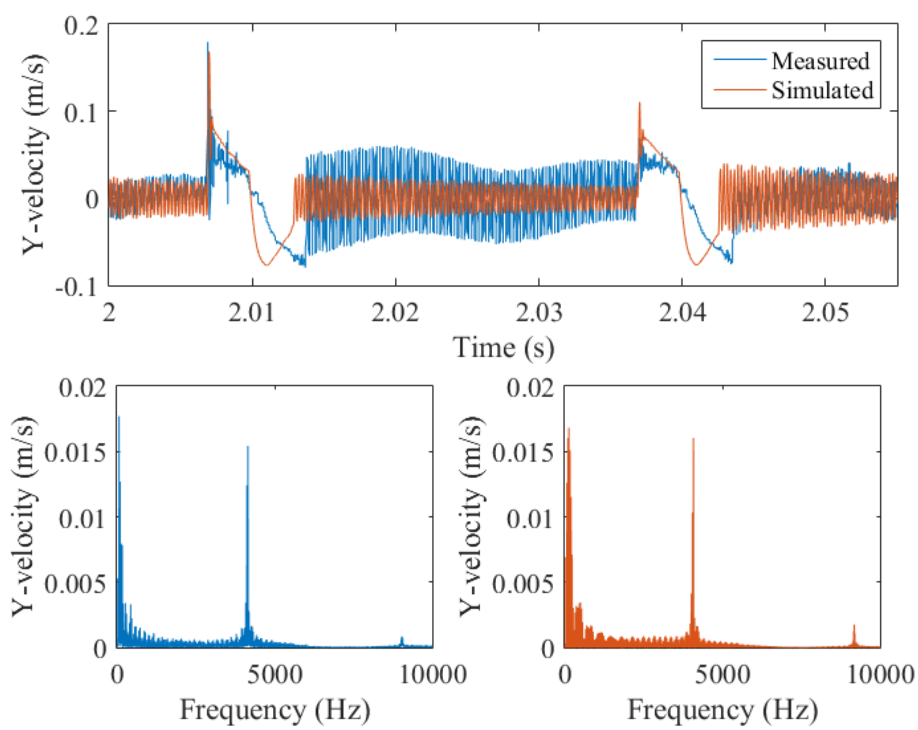

Figure 6.25: Measured and simulated y direction workpiece velocity shown in the time and frequency domains for the 2 mm thick rib.

6.3 Spatially Dependent Workpiece Dynamics Validation

To validate the time domain simulation including spatially dependent workpiece dynamics, experiments were conducted. The validation tests were conducted on compliant workpieces, shown in Figure 6.26. The compliant workpiece was machined from titanium alloy Ti6Al4V (Grade 5) and includes two thin-walled structures (ribs) with clamped-clamped-clamped-free (CCCF) boundary conditions. The nominal geometric dimensions of the thin-walled structures, or ribs, are given in Table 6.9.

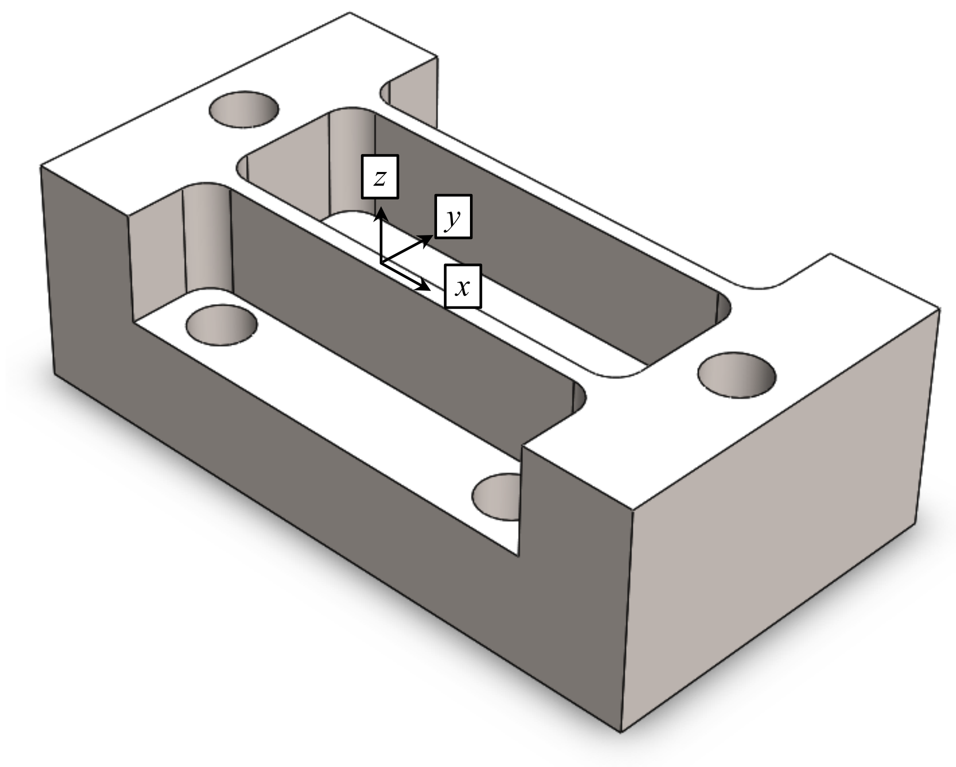

Figure 6.26: Solid model of the flexible workpiece (simulated preform) used for validation testing.

Validation tests were performed on a Haas TM1 vertical machining center with a maximum spindle speed of 4000 rpm. Cutting forces, measured by a dynamometer (Kistler 9257B), and workpiece velocity, measured by a laser vibrometer (Polytec OFV-534), were the primary metrics for validating the simulation outputs. Minimum quantity lubrication (MQL) (i.e., mist coolant) was used during the test cuts. The cutting tool used for the validation experiments was a 19.05 mm carbide end mill with two flutes, evenly spaced, and a 30° helix angle. Modal parameters for the tool were obtained via impact testing using an instrumented hammer (PCB 086C04) to provide the excitation force and a low mass accelerometer (PCB 352C23) to record the response. Table 6.10 lists the natural frequency, f_n, modal stiffness, k, and damping ratio, ζ, for the dominant modes in the plane of the cut (i.e., x-y).

Table 6.9: Nominal geometric dimensions of the flexible ribs.

Length	Height	Thickness
100 mm	24 mm	4 mm

The workpiece was bolted to a cutting force dynamometer (Kistler 9257B) during impact testing, as shown in Figure 6.27, to properly represent the workpiece dynamics during the validation tests. An instrumented hammer (PCB 084A17) was used to provide the excitation force and the workpiece response was measured using a non-contact laser vibrometer (Polytec OFV-534). The measurement was performed at the top, center (i.e., location of minimum stiffness) of the flexible, thin wall. Table 6.11 lists the natural frequency, f_n, modal stiffness, k, and damping ratio, ζ, for the first modes in the direction of greatest compliance (i.e., y direction). The strategy detailed in section 4.1.3 was used to extrapolate the measured workpiece stiffness across the entire thin wall surface.

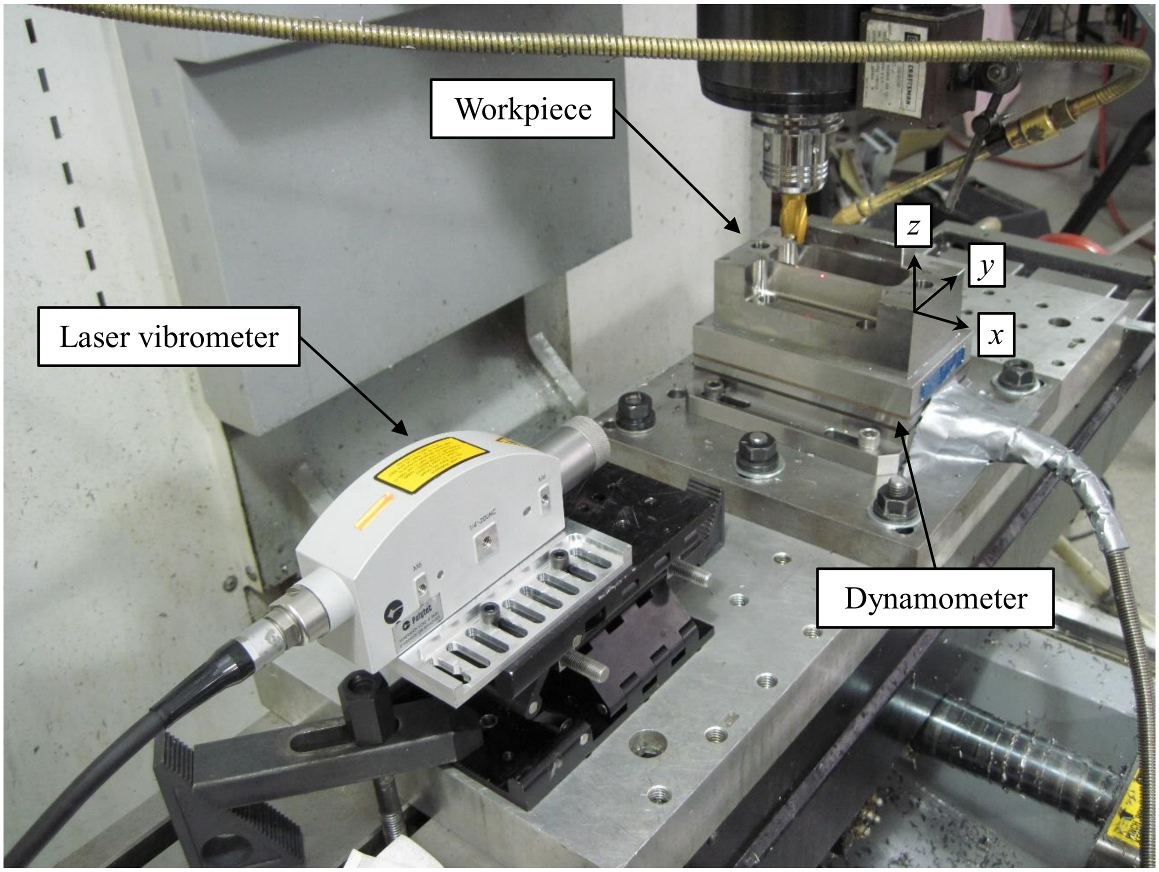

Figure 6.27: Impact testing setup for the compliant workpiece.

Table 6.10: Modal parameters for the cutting tool.

	x direction	
f_n (Hz)	k (N/m)	ζ
1029	4.3×10^7	0.0685
	y direction	
f_n (Hz)	k (N/m)	ζ
1161	6.6×10^7	0.0483

The specific force coefficients used to calibrate the mechanistic force model applied in the time domain simulation were calculated using a nonlinear optimization method similar to the technique described in [78]. This method fits a set of simulated, instantaneous cutting forces to a set of measured, instantaneous cutting forces by iteratively updating the specific force coefficients until the convergence criteria is met. The cutting force coefficients may be considered to be a function of not only the cutting tool geometry and workpiece material, but also machining parameters. Cutting tests, for determining the specific force coefficients, were performed at 2.6% radial immersion, 5 mm axial depth of cut, 1000 rpm spindle speed, and a commanded feed rate of $0.1\ \mathrm{mm/tooth}$. Table 6.12 lists the six specific force coefficients used in the simulation.

Table 6.11: Modal parameters for the compliant workpiece.

Mode	$f_n\ (Hz)$	$k\ (N/m)$	ζ
1	7391	1.2×10^7	0.0010

Table 6.12: Cutting force coefficients used in the time domain simulation.

Cutting force coefficients		
$k_{tc}\ (N/mm^2)$	$k_{rc}\ (N/mm^2)$	$k_{ac}(N/mm^2)$
2076	918	895
Edge force coefficients		
$k_{te}\ (N/mm)$	$k_{re}\ (N/mm)$	$k_{ae}\ (N/mm)$
8	18	-4

The simulations were performed at 2.6% radial immersion in a down milling configuration with a commanded feed rate of $0.1\ \mathrm{mm/tooth}$, a spindle speed of $1000\ rpm$, and an axial depth of cut of $5\ mm$. Flute-to-flute runout was specified as

17.5 μm, and the total length of the cut in the x direction was $100\ mm$. The first vibration mode of the workpiece was included in the simulation. As shown in Figure 6.28, the simulation predicts that as the workpiece stiffness reaches a minimum, the cutting forces also reach a minimum. Similarly, the workpiece velocity reaches a maximum.

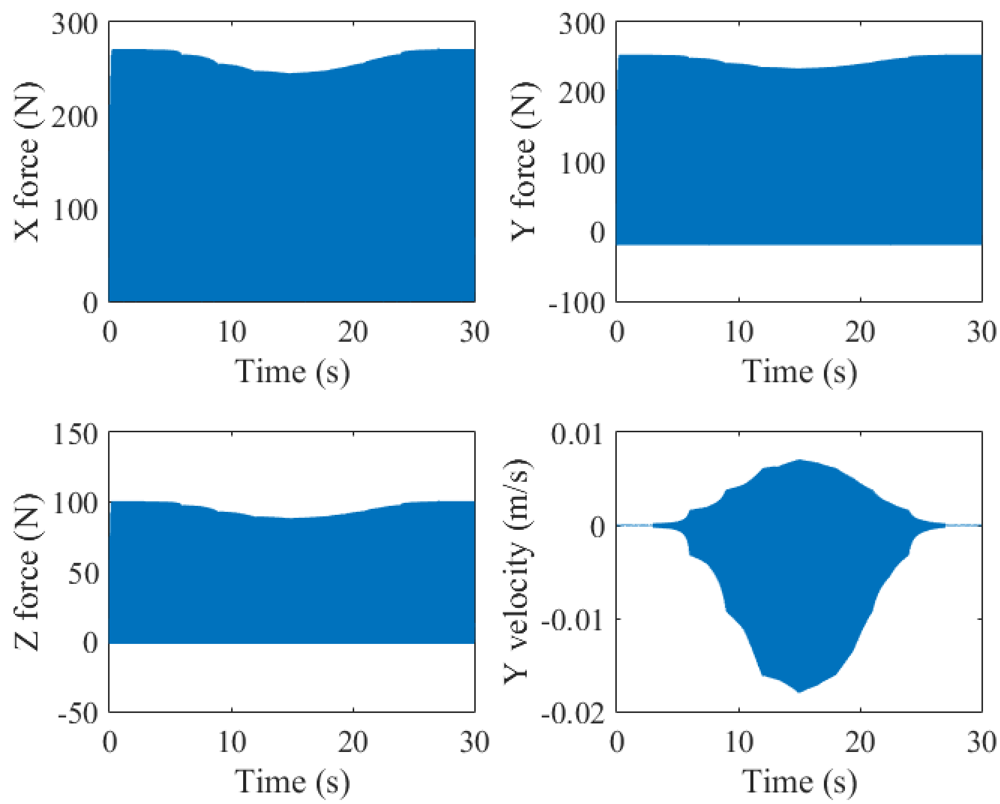

Figure 6.28: Simulated x, y, and z direction cutting forces and y direction workpiece velocity.

6.3.1 Experiment Results

In this section, the validation testing of the time domain simulation including spatially dependent workpiece dynamics is presented. Simulated and measured workpiece velocity (y direction) and cutting forces (x, y, and z directions) are compared in both the time and frequency domains. Although the simulated cut was $100\ mm$ in total length, the validation test cut was limited to $76\ mm$ due to geometric limitations imposed by the workpiece and tool geometries.

For brevity, only the y direction (i.e., the flexible direction) cutting forces and workpiece velocities are shown. The x and z direction cutting forces are provided as supplementary evidence in APPENDIX B.2. Figure 6.29 shows the measured and simulated y direction cutting forces in the time domain. The time domain simulation captures the reduction in cutting forces with workpiece stiffness due to dynamic deflections (i.e., near the center of the cut). A comparison of the simulated and measured cutting forces over one cutter revolution for two different regions of the cut (i.e., workpiece stiffnesses) is also provided. The variation in cutting forces between adjacent flute engagements is due to flute-to-flute runout. The maximum difference in peak cutting force was approximately $14\ \%$.

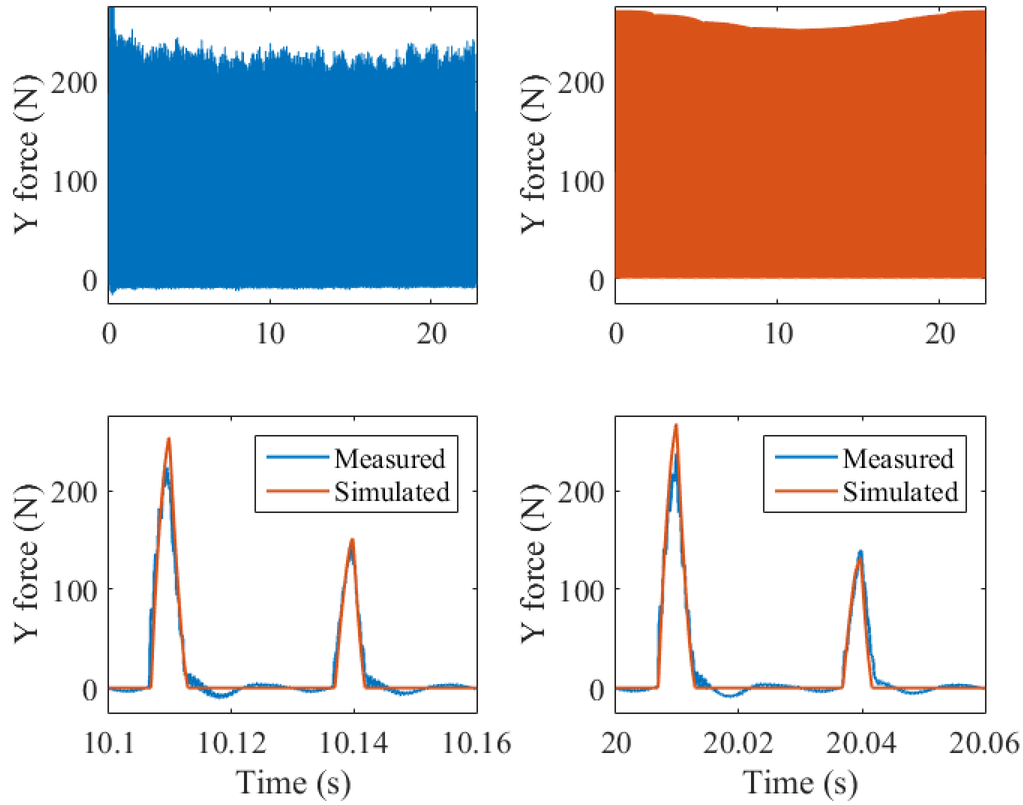

Figure 6.29: Measured and simulated cutting forces in the *y* direction over the entire cut length (top) and over one revolution of the two flute cutting tool (bottom).

The frequency content of the *y* direction cutting forces, calculated using the fast Fourier transform (FFT) of the data in Figure 6.29, is given in Figure 6.30. It is observed that the dominant frequencies are the tooth passing frequency, 33.3 Hz, and the runout frequency, 16.7 Hz, as well as their integer multiples (i.e., harmonics).

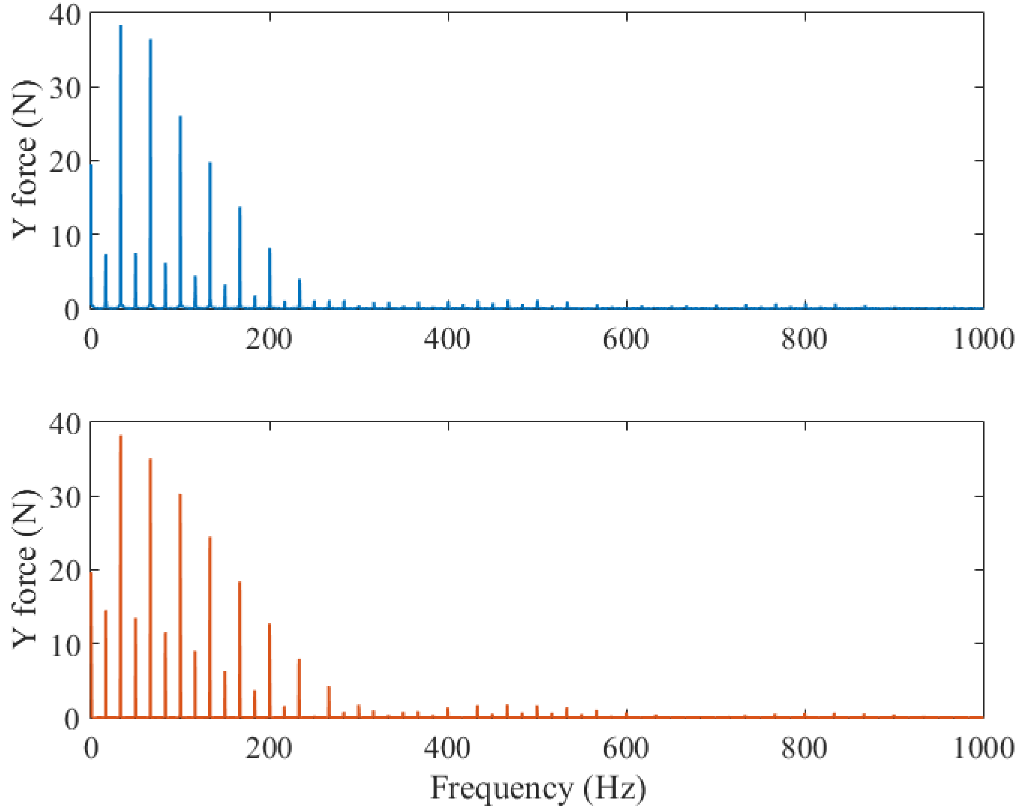

Figure 6.30: Frequency content of the measured (top) and simulated (bottom) *y* direction cutting forces.

The agreement between the measured and simulated workpiece velocity in the *y* direction can be observed in Figure 6.31. As expected, measurements confirm that workpiece velocity increases to a maximum as the cutting tool approaches the center of the cut (i.e., minimum workpiece stiffness).

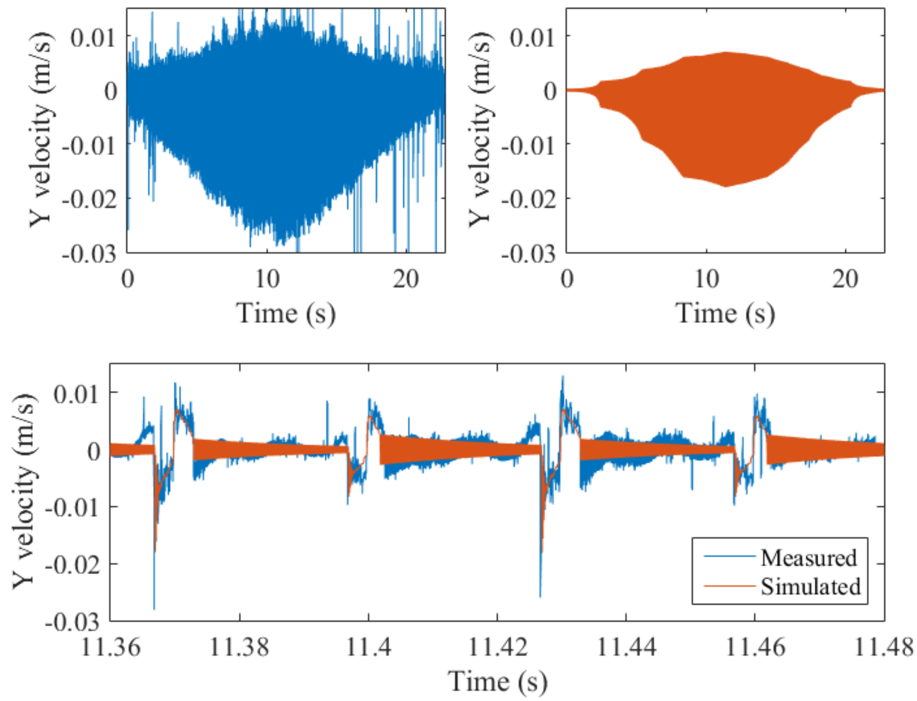

Figure 6.31: Measured and simulated workpiece velocity in the *y* direction over the entire cut length (top) and over two revolutions of the two flute cutting tool (bottom).

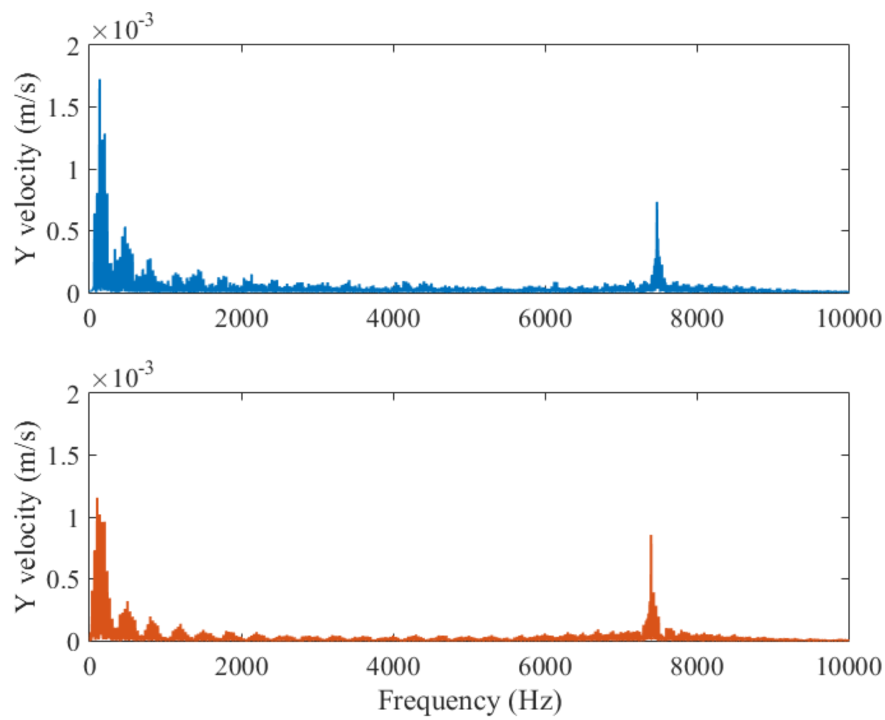

Figure 6.32: Frequency content of the measured (top) and simulated (bottom) *y* direction workpiece velocity.

CHAPTER 7: CONCLUSIONS

In this research, a time domain simulation was presented for predicting stable and unstable milling conditions with application in finish milling of compliant workpieces. The ability of the simulation to deliver the global stability predictions of traditional stability lobe diagrams was demonstrated, and the specific, local information provided by the individual time domain simulations was also validated experimentally.

First, a comparative study was presented that examined the dependence of cutting force coefficients on milling process parameters, including feed per tooth, spindle speed, and radial immersion. The mechanistic force model was detailed and the methods for calibrating the model (i.e., determining the cutting force coefficients) were presented. Next, the cutting force coefficients, calculated using the average force, linear regression and instantaneous force, nonlinear optimization methods, for a range of milling process parameters were reported. Finally, the instantaneous force, nonlinear optimization method was validated in the framework of milling stability tests.

Based on the "Regenerative Force, Dynamic Deflection Model", the time domain simulation determines the instantaneous chip thickness, calculates cutting forces, and uses Euler (fixed time step) numerical integration of the equations of motion to determine tool/workpiece deflections at each incremental time step. The equations of motion are solved in modal coordinates, and the dynamics of the tool and workpiece are represented using modal parameters for an arbitrary number of degrees of freedom. An automated, modal parameter identification method was presented that utilizes a two-stage process including: (1) individual mode identification using the peaking picking method and (2) a nonlinear optimization for all modes.

The outcome of individual time domain simulations contains information specific to the individual spindle speed-axial depth of cut combinations. This includes the instantaneous cutting forces and tool/workpiece deflections, velocities, and accelerations. Based on these keys process outputs, two stability metrics are presented. The first method uses peak-to-peak (PTP) cutting forces [79] and the second method, developed in this research, uses the amplitude ratio of the chatter frequency and tooth passing frequency. The stability diagrams are a contour map of these stability metrics and represent numerous time domain simulations performed over a range of spindle speed-axial depth of cut combinations.

To evaluate the amplitude ratio diagrams, comparison to results found in the literature were performed. Two cases of interest in milling were selected for the study: (1) period-*n* flip instability and (2) helix angle induced islands of instability. It was shown that in both cases, the amplitude ratio diagram was able to delivered similar information in terms of global stability behavior. Additionally, the amplitude ratio diagram provides evidence about the severity of chatter at different spindle speed-axial depth of cut combinations.

To validate the PTP force diagrams, experiments were conducted. The cutting tests were performed on compliant workpieces which simulate near net shape preforms. These compliant workpieces were machined from 6061-T651 aluminum and are composed of two thin-walled structures (ribs) with clamped-clamped-clamped-free (CCCF) boundary conditions. Simulated and measured cutting forces for the stable and unstable validation tests were presented. The agreement of the results was demonstrated in both the time and frequency domains.

A methodology to incorporate the spatial variation of workpiece dynamics into the time domain simulation was presented. The dynamics, represented by the frequency response function, over a grid of discrete positions on the workpiece are modeled and predicted using the finite element method. Modal parameters were extracted using the peak picking technique, and the simulated modal stiffnesses were normalized to the minimum stiffness value thereby constituting a lookup table of multiplication factors. The FRF of the workpiece was experimentally measured at the location of minimum stiffness, and the lookup table of multiplication factors was used to extrapolate the measured stiffness to the simulation locations. Linear interpolation was used to calculate the unknown modal stiffnesses at coordinates adjacent to the simulation coordinates. In the time domain simulation, the tool position at each discrete time step is monitored, and the modal parameters for that position are used to solve the dynamic equations of motion in modal coordinates.

To validate the time domain simulation including spatially dependent workpiece dynamics, experiments were conducted. The validation tests were conducted on compliant workpieces machined from titanium alloy Ti6Al4V (Grade 5) with clamped-clamped-clamped-free (CCCF) boundary conditions. Simulated and measured workpiece velocity (y direction) and cutting forces (x, y, and z directions) are compared in both the time and frequency domains. The time domain simulation captures the reduction in cutting forces and the increase in workpiece velocity with decreasing workpiece stiffness due to dynamic deflections (i.e., near the center of the cut).

REFERENCES

[1] J. Tlusty, S. Smith, W.R. Winfough, Techniques for the Use of Long Slender End Mills in High-speed Milling, CIRP Annals - Manufacturing Technology, 45 (1996) 393-396.

[2] S. Smith, D. Dvorak, Tool path strategies for high speed milling aluminum workpieces with thin webs, Mechatronics, 8 (1998) 291-300.

[3] S. Smith, W.R. Winfough, J. Halley, The Effect of Tool Length on Stable Metal Removal Rate in High Speed Milling, CIRP Annals - Manufacturing Technology, 47 (1998) 307-310.

[4] J. Halley, A. Helvey, K. Smith, W. Winfough, The impact of high-speed machining on the design and fabrication of aircraft components, in: Proceedings of 1999 ASME Design and Technical Conference, 1999.

[5] S. Smith, R. Wilhelm, B. Dutterer, H. Cherukuri, G. Goel, Sacrificial structure preforms for thin part machining, CIRP Annals-Manufacturing Technology, 61 (2012) 379-382.

[6] M.A. Davies, B. Balachandran, Impact dynamics in milling of thin-walled structures, Nonlinear Dynamics, 22 (2000) 375-392.

[7] M.A. Davies, J.R. Pratt, B.S. Dutterer, T.J. Burns, The Stability of Low Radial Immersion Milling, CIRP Annals - Manufacturing Technology, 49 (2000) 37-40.

[8] M.A. Davies, J.R. Pratt, B. Dutterer, T.J. Burns, Stability Prediction for Low Radial Immersion Milling, Journal of Manufacturing Science and Engineering, 124 (2002) 217.

[9] J. Gradišek, E. Govekar, I. Grabec, M. Kalveram, K. Weinert, T. Insperger, G. Stépán, On Stability Prediction for Low Radial Immersion Milling, Machining Science and Technology, 9 (2005) 117-130.

[10] S. Smith, J. Tlusty, Efficient simulation programs for chatter in milling, Annals of the CIRP, 42 (1993) 463-466.

[11] F.W. Taylor, The art of cutting metals, Scientific American, 63 (1907) 25942-25944.

[12] S. Tobias, W. Fishwick, Theory of regenerative machine tool chatter, The engineer, 205 (1958) 199-203.

[13] J. Tlusty, M. Polacek, The stability of machine tools against self-excited vibrations

in machining, International research in production engineering, 1 (1963) 465-474.

[14] H.E. Merritt, Theory of Self-Excited Machine-Tool Chatter: Contribution to Machine-Tool Chatter Research—, Journal of Manufacturing Science and Engineering, 87 (1965) 447-454.

[15] P. Wallace, C. Andrew, Machining forces: some effects of tool vibration, Journal of mechanical engineering science, 7 (1965) 152-162.

[16] T.R. Sisson, R.L. Kegg, An explanation of low-speed chatter effects, Journal of Engineering for Industry, 91 (1969) 951-958.

[17] J. Peters, P. Vanherck, H. Van Brussel, The measurement of the dynamic cutting coefficient, CIRP Annals-Manufacturing Technology, (1971) 129-136.

[18] J. Tlusty, Analysis of the state of research in cutting dynamics, Annals of the CIRP, 27 (1978) 583-589.

[19] C.T. Tyler, T.L. Schmitz, Analytical process damping stability prediction, Journal of Manufacturing Processes, 15 (2013) 69-76.

[20] J. Tlusty, W. Zaton, F. Ismail, Stability lobes in milling, CIRP Annals-Manufacturing Technology, 32 (1983) 309-313.

[21] S. Smith, J. Tlusty, Update on high-speed milling dynamics, Journal of Engineering for Industry, 112 (1990) 142-149.

[22] S. Smith, J. Tlusty, An overview of modeling and simulation of the milling process, Journal of engineering for industry, 113 (1991) 169-175.

[23] Y. Altintaş, E. Budak, Analytical prediction of stability lobes in milling, CIRP Annals-Manufacturing Technology, 44 (1995) 357-362.

[24] S.D. Merdol, Y. Altintas, Multi Frequency Solution of Chatter Stability for Low Immersion Milling, Journal of Manufacturing Science and Engineering, 126 (2004) 459.

[25] T. Insperger, B.P. Mann, G. Stépán, P.V. Bayly, Stability of up-milling and down-milling, part 1: alternative analytical methods, International journal of Machine tools and manufacture, 43 (2003) 25-34.

[26] S. Smith, R. Wilhelm, B. Dutterer, H. Cherukuri, G. Goel, Sacrificial structure preforms for thin part machining, CIRP Annals - Manufacturing Technology, 61 (2012) 379-382.

[27] T. Aoyama, Y. Kakinuma, Development of Fixture Devices for Thin and Compliant

Workpieces, CIRP Annals - Manufacturing Technology, 54 (2005) 325-328.

[28] K. Kolluru, D. Axinte, A. Becker, A solution for minimising vibrations in milling of thin walled casings by applying dampers to workpiece surface, CIRP Annals - Manufacturing Technology, 62 (2013) 415-418.

[29] F. Ismail, R. Ziaei, Chatter suppression in five-axis machining of flexible parts, International Journal of Machine Tools and Manufacture, 42 (2002) 115-122.

[30] E. Shamoto, T. Mori, K. Nishimura, T. Hiramatsu, Y. Kurata, Suppression of regenerative chatter vibration in simultaneous double-sided milling of flexible plates by speed difference, CIRP Annals - Manufacturing Technology, 59 (2010) 387-390.

[31] I. Mañé, V. Gagnol, B.C. Bouzgarrou, P. Ray, Stability-based spindle speed control during flexible workpiece high-speed milling, International Journal of Machine Tools and Manufacture, 48 (2008) 184-194.

[32] U. Bravo, O. Altuzarra, L.N. López de Lacalle, J.A. Sánchez, F.J. Campa, Stability limits of milling considering the flexibility of the workpiece and the machine, International Journal of Machine Tools and Manufacture, 45 (2005) 1669-1680.

[33] V. Thevenot, L. Arnaud, G. Dessein, G. Cazenave–Larroche, Influence of Material Removal on the Dynamic Behavior of Thin-Walled Structures in Peripheral Milling, Machining Science and Technology, 10 (2006) 275-287.

[34] E. Budak, L.T. Tunç, S. Alan, H.N. Özgüven, Prediction of workpiece dynamics and its effects on chatter stability in milling, CIRP Annals - Manufacturing Technology, 61 (2012) 339-342.

[35] H.N. Özgüven, Structural modifications using frequency response functions, Mechanical Systems and Signal Processing, 4 (1990) 53-63.

[36] S. Alan, E. Budak, H.N. Özgüven, Analytical prediction of part dynamics for machining stability analysis, International Journal of Automation Technology, 4 (2010) 259-267.

[37] M.A. Davies, B. Dutterer, J.R. Pratt, A.J. Schaut, J.B. Bryan, On the Dynamics of High-Speed Milling with Long, Slender Endmills, CIRP Annals - Manufacturing Technology, 47 (1998) 55-60.

[38] T.L. Schmitz, A. Honeycutt, The Extended Milling Bifurcation Diagram, Procedia Manufacturing, 1 (2015) 466-476.

[39] M.L. Campomanes, Y. Altintas, An Improved Time Domain Simulation for Dynamic Milling at Small Radial Immersions, Journal of Manufacturing Science

and Engineering, 125 (2003) 416.

[40] M.X. Zhao, B. Balachandran, Dynamics and stability of milling process, International Journal of Solids and Structures, 38 (2001) 2233-2248.

[41] B.P. Mann, T. Insperger, P.V. Bayly, G. Stepan, Stability of up-milling and down-milling, part 2: experimental verification, International Journal of Machine Tools & Manufacture, 43 (2003) 35-40.

[42] T. Insperger, G. Stépán, Vibration Frequencies in High-Speed Milling Processes or a Positive Answer to Davies, Pratt, Dutterer and Burns, Journal of Manufacturing Science and Engineering, 126 (2004) 481.

[43] E. Govekar, J. Gradišek, M. Kalveram, T. Insperger, K. Weinert, G. Stépàn, I. Grabec, On Stability and Dynamics of Milling at Small Radial Immersion, CIRP Annals - Manufacturing Technology, 54 (2005) 357-362.

[44] F.C. Moon, T. Kalmar-Nagy, Nonlinear models for complex dynamics in cutting materials, Philosophical Transactions of the Royal Society London A, 359 (2001) 695-711.

[45] F.C. Moon, Dynamics and chaos in manufacturing processes, Wiley, 1998.

[46] T. Kalmár-Nagy, G. Stépán, F.C. Moon, Subcritical Hopf bifurcation in the delay equation model for machine tool vibrations, Nonlinear Dynamics, 26 (2001) 121-142.

[47] M. Zatarain, J. Muñoa, G. Peigné, T. Insperger, Analysis of the Influence of Mill Helix Angle on Chatter Stability, CIRP Annals - Manufacturing Technology, 55 (2006) 365-368.

[48] T. Insperger, J. Munoa, M. Zatarain, G. Peigne, Unstable Islands in the Stability Chart of Milling Processes Due to the Helix Angle, in: CIRP 2nd International Conference on High Performance Cutting, Vancouver, Canada, 2006.

[49] B. Patel, B. Mann, K. Young, Uncharted islands of chatter instability in milling, International Journal of Machine Tools and Manufacture, 48 (2008) 124-134.

[50] K.F.K. Ehmann, S. G.; DeVor, R. E.; Lazoglu, I., Machining Process Modeling: A Review, Journal of Manufacturing Science and Engineering, 119 (1997) 655 - 663.

[51] C.A. van Luttervelt, T.H.C. Childs, I.S. Jawahir, F. Klocke, P.K. Venuvinod, Y. Altintas, E. Armarego, D. Dornfeld, I. Grabec, J. Leopold, B. Lindstrom, D. Lucca, T. Obikawa, Shirakashi, H. Sato, Present Situation and Future Trends in Modelling of Machining Operations Progress Report of the CIRP Working Group 'Modelling of Machining Operations', CIRP Annals - Manufacturing Technology, 47 (1998)

587-626.

[52] M.E. Merchant, Basic mechanics of the metal cutting process, Journal of Applied Mechanics, 11 (1944) 168-175.

[53] E.J.A.B. Amarego, R. H. , The Machining of Metals, Prentice-Hall, 1969.

[54] J. Mackerle, Finite-element analysis and simulation of machining: a bibliography (1976–1996), Journal of Materials Processing Technology, 86 (1999) 17-44.

[55] M. Martellotti, An analysis of the milling process, trans. ASME, 63 (1941).

[56] F. Koenigsberger, A. Sabberwal, An investigation into the cutting force pulsations during milling operations, International Journal of Machine Tool Design and Research, 1 (1961) 15-33.

[57] A. Sabberwal, F. Koenigsberger, Chip section and cutting force during the milling operation, CIRP Ann, 10 (1961) 62.

[58] E. Budak, Y. Altintas, E. Armarego, Prediction of milling force coefficients from orthogonal cutting data, Journal of Manufacturing Science and Engineering, 118 (1996) 216-224.

[59] T.L. Schmitz, K.S. Smith, Machining dynamics: frequency response to improved productivity, Springer Science & Business Media, 2008.

[60] Y. Altintas, Manufacturing automation: metal cutting mechanics, machine tool vibrations, and CNC design, Cambridge university press, 2012.

[61] O. Gonzalo, J. Beristain, H. Jauregi, C. Sanz, A method for the identification of the specific force coefficients for mechanistic milling simulation, International Journal of Machine Tools and Manufacture, 50 (2010) 765-774.

[62] G. Campatelli, A. Scippa, Prediction of Milling Cutting Force Coefficients for Aluminum 6082-T4, Procedia CIRP, 1 (2012) 563-568.

[63] M. Magnevall, M. Lundblad, K. Ahlin, G. Broman, High Frequency Measurements of Cutting Forces in Milling by Inverse Filtering, Machining Science and Technology, 16 (2012) 487-500.

[64] L. Ricardo Castro, P. Viéville, P. Lipinski, Correction of dynamic effects on force measurements made with piezoelectric dynamometers, International Journal of Machine Tools and Manufacture, 46 (2006) 1707-1715.

[65] T.L. Schmitz, J. Couey, E. Marsh, N. Mauntler, D. Hughes, Runout effects in milling: Surface finish, surface location error, and stability, International Journal of

Machine Tools and Manufacture, 47 (2007) 841-851.

[66] L.M. Kumanchik, T.L. Schmitz, Improved analytical chip thickness model for milling, Precision Engineering, 31 (2007) 317-324.

[67] H.-Y. Feng, C.-H. Menq, The prediction of cutting forces in the ball-end milling process—I. Model formulation and model building procedure, International Journal of Machine Tools and Manufacture, 34 (1994) 697-710.

[68] T.F. Coleman, Y. Li, On the convergence of interior-reflective Newton methods for nonlinear minimization subject to bounds, Mathematical programming, 67 (1994) 189-224.

[69] N. Grossi, L. Sallese, A. Scippa, G. Campatelli, Chatter stability prediction in milling using speed-varying cutting force coefficients, Procedia CIRP, 14 (2014) 170-175.

[70] N. Grossi, L. Sallese, A. Scippa, G. Campatelli, Speed-varying cutting force coefficient identification in milling, Precision Engineering, 42 (2015) 321-334.

[71] T. Schmitz, S. Smith, Machining Dynamics: Frequency Response to Improved Productivity, Springer, New York, NY, 2009.

[72] G. Tlusty, Manufacturing Processes and Equipment, Prentice Hall, Upper Saddle River, 2000.

[73] J. Tlusty, F. Ismail, Basic non-linearity in machining chatter, CIRP Annals, 30 (1981) 299-304.

[74] E. Budak, Y. Altintas, E.J.A. Armarego, Prediction of milling force coefficients from orthogonal cutting data, Journal of Manufacturing Science and Engineering, 118 (1996) 216-224.

[75] V. Ganguly, Characterization of the Dynamic Performance of Machining Spindles, in: Mechanical Engineering and Engineering Sciences, Unviersity of North Carolina at Charlotte, 2014.

[76] V. Gagnol, B. Bouzgarrou, P. Ray, C. Barra, Model-based chatter stability prediction for high-speed spindles, International Journal of machine tools and manufacture, 47 (2007) 1176-1186.

[77] J. Menezes, Semi-Analytical Model of Thin Plate Dynamics, in: Mechanical Engineering and Engineering Sciences, University of North Carolina at Charlotte, 2015.

[78] O. Gonzalo, J. Beristain, H. Jauregi, C. Sanz, A method for the identification of the

specific force coefficients for mechanistic milling simulation., International Journal of Machine Tools & Manufacture, 50 (2010) 765-774.

[79] S. Smith, J. Tlusty, Efficient Simulation Programs for Chatter in Milling, CIRP Annals - Manufacturing Technology, 42 (1993) 463-466.

APPENDIX A: ARBITRARY RADIAL IMMERSION CUTTING FORCE COEFFICIENT SOLUTION

For the general case of arbitrary radial immersion, the six cutting force coefficients of the mechanistic cutting force model from section 3.3.1 may be solved as follows. Expanding equations (3.6), (3.7), and (3.8) and arranging them in slope-intercept form gives:

$$\begin{aligned}\bar{F}_x = \frac{N_t b}{8\pi}\{k_t[\cos(2\emptyset_s) - \cos(2\emptyset_e)] \\ + k_n[(2\emptyset_e - \sin(2\emptyset_e)) - (2\emptyset_s - \sin(2\emptyset_s))]\}f_t \\ + \frac{N_t b}{2\pi}\{k_{te}[\sin(\emptyset_e) - \sin(\emptyset_s)] + k_{ne}[\cos(\emptyset_s) - \cos(\emptyset_e)]\}\end{aligned} \tag{A.1}$$

$$\begin{aligned}\bar{F}_y = \frac{N_t b}{8\pi}\{k_t[(2\emptyset_e - \sin(2\emptyset_e)) - (2\emptyset_s - \sin(2\emptyset_s))] \\ + k_n[\cos(2\emptyset_e) - \cos(2\emptyset_s)]\}f_t \\ + \frac{N_t b}{2\pi}\{k_{te}[\cos(\emptyset_s) - \cos(\emptyset_e)] + k_{ne}[\sin(\emptyset_s) - \sin(\emptyset_e)]\}\end{aligned} \tag{A.2}$$

$$\bar{F}_z = \frac{N_t b}{2\pi}\{k_a[\cos(\emptyset_e) - \cos(\emptyset_s)]\}f_t + \frac{N_t b}{2\pi}\{k_{ae}[\emptyset_s - \emptyset_e]\} \tag{A.3}$$

where the coefficient multiplying feed per tooth is the slope and the remaining term is the intercept. Arranging the expressions in matrix form yields:

$$\begin{bmatrix} b_{11} & \cdots & b_{16} \\ \vdots & \ddots & \vdots \\ b_{61} & \cdots & b_{66} \end{bmatrix} \begin{Bmatrix} k_{tc} \\ k_{te} \\ k_{nc} \\ k_{ne} \\ k_{ac} \\ k_{ae} \end{Bmatrix} = \begin{Bmatrix} a_{1x} \\ a_{0x} \\ a_{1y} \\ a_{0y} \\ a_{1z} \\ a_{0z} \end{Bmatrix} \tag{A.4}$$

where:

$$b_{11} = \frac{N_t b}{8\pi}\left[\cos(2\phi_s) - \cos(2\phi_e)\right] \tag{A.5}$$

$$b_{13} = \frac{N_t b}{8\pi}\left[(2\phi_e - 2\phi_s) + (\sin(2\phi_s) - \sin(2\phi_e))\right] \tag{A.6}$$

$$b_{22} = \frac{N_t b}{2\pi}\left[\sin(\phi_e) - \sin(\phi_s)\right] \tag{A.7}$$

$$b_{24} = \frac{N_t b}{2\pi}\left[\cos(\phi_s) - \cos(\phi_e)\right] \tag{A.8}$$

$$b_{31} = \frac{N_t b}{8\pi}\left[(2\phi_e - 2\phi_s) + (\sin(2\phi_s) - \sin(2\phi_e))\right] \tag{A.9}$$

$$b_{33} = \frac{N_t b}{8\pi}[\cos(2\phi_e) - \cos(2\phi_s)] \tag{A.10}$$

$$b_{42} = \frac{N_t b}{2\pi}[\cos(\phi_s) - \cos(\phi_e)] \tag{A.11}$$

$$b_{44} = \frac{N_t b}{2\pi}[\sin(\phi_s) - \sin(\phi_e)] \tag{A.12}$$

$$b_{55} = \frac{N_t b}{2\pi}[\cos(\phi_e) - \cos(\phi_s)] \tag{A.13}$$

$$b_{66} = \frac{N_t b}{2\pi}(\phi_s - \phi_e) \tag{A.14}$$

All other elements are equal to 0. The vector of specific force coefficients can be determined using:

$$\begin{Bmatrix} k_{tc} \\ k_{te} \\ k_{nc} \\ k_{ne} \\ k_{ac} \\ k_{ae} \end{Bmatrix} = \begin{bmatrix} b_{11} & \cdots & b_{16} \\ \vdots & \ddots & \vdots \\ b_{61} & \cdots & b_{66} \end{bmatrix}^{-1} \begin{Bmatrix} a_{1x} \\ a_{0x} \\ a_{1y} \\ a_{0y} \\ a_{1z} \\ a_{0z} \end{Bmatrix} \tag{A.15}$$

APPENDIX B: SUPPLEMENTARY EXPERIMENTAL MILLING SIMULATION VALIDATION

B.1 Titanium Milling Stability Validation

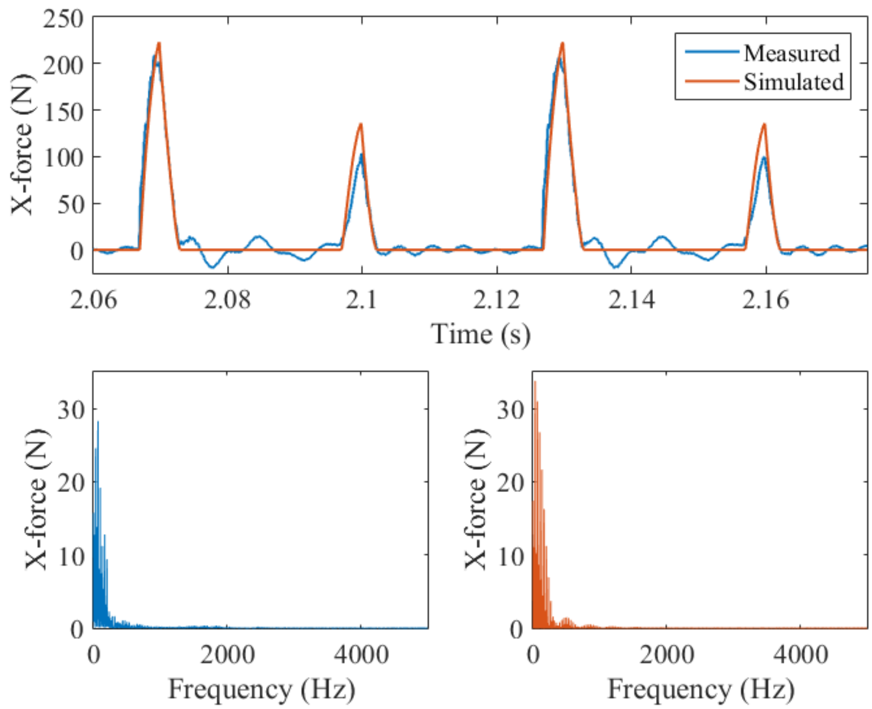

Figure B.1: Measured and simulated x direction cutting force shown in the time and frequency domains for the 3.5 mm thick rib.

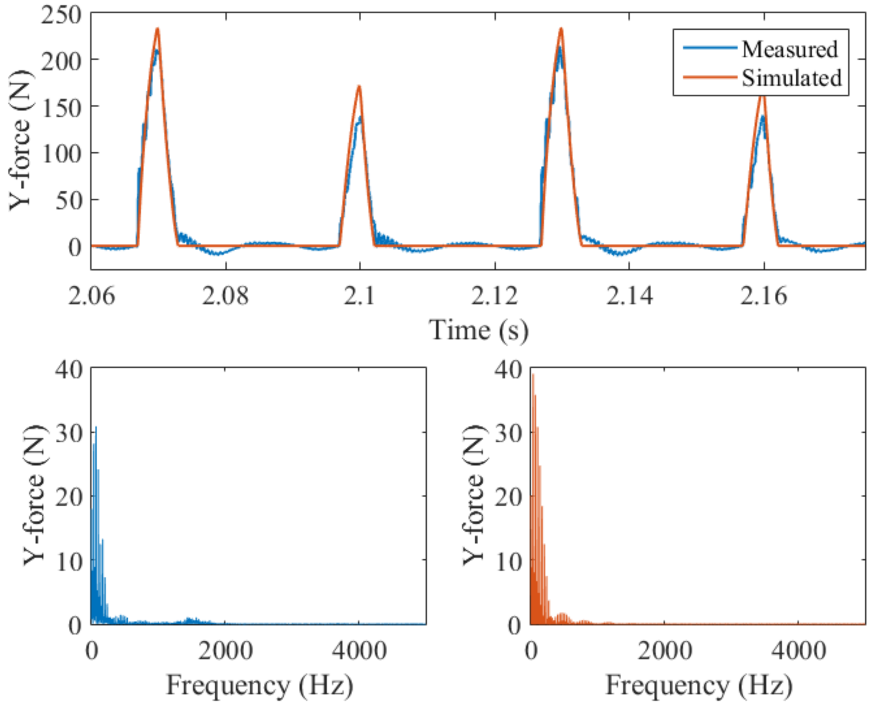

Figure B.2: Measured and simulated y direction cutting force shown in the time and frequency domains for the 3.5 mm thick rib.

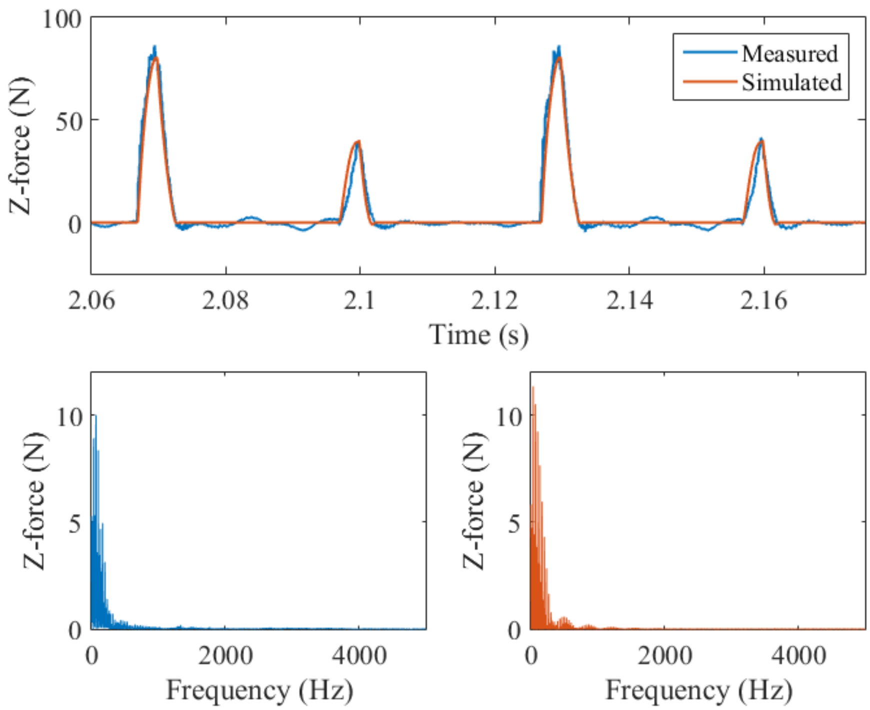

Figure B.3: Measured and simulated z direction cutting force shown in the time and frequency domains for the 3.5 mm thick rib.

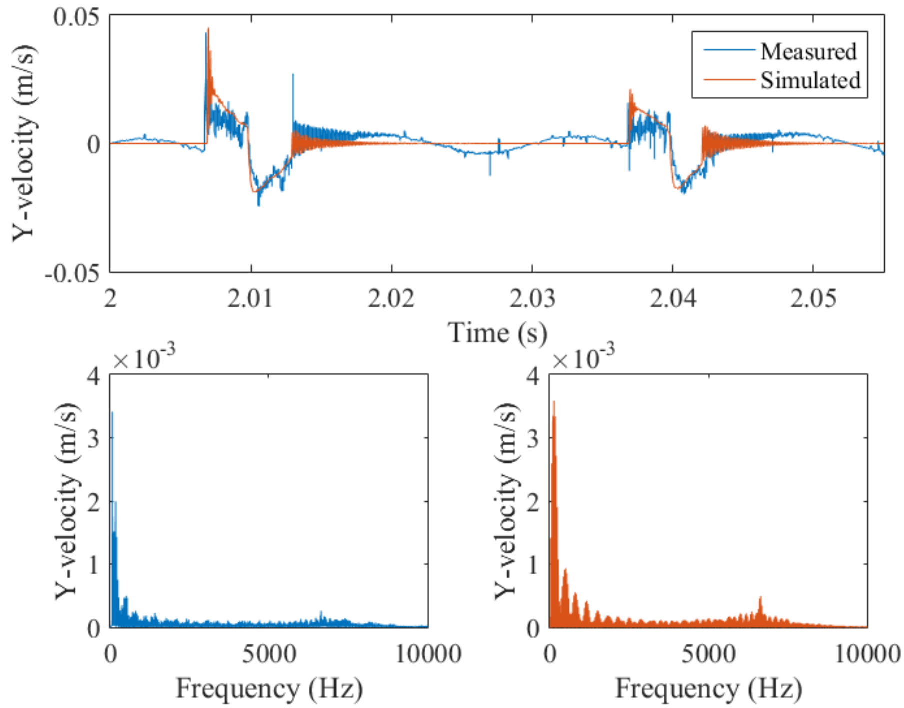

Figure B.4: Measured and simulated *y* direction workpiece velocity shown in the time and frequency domains for the 3.5 mm thick rib.

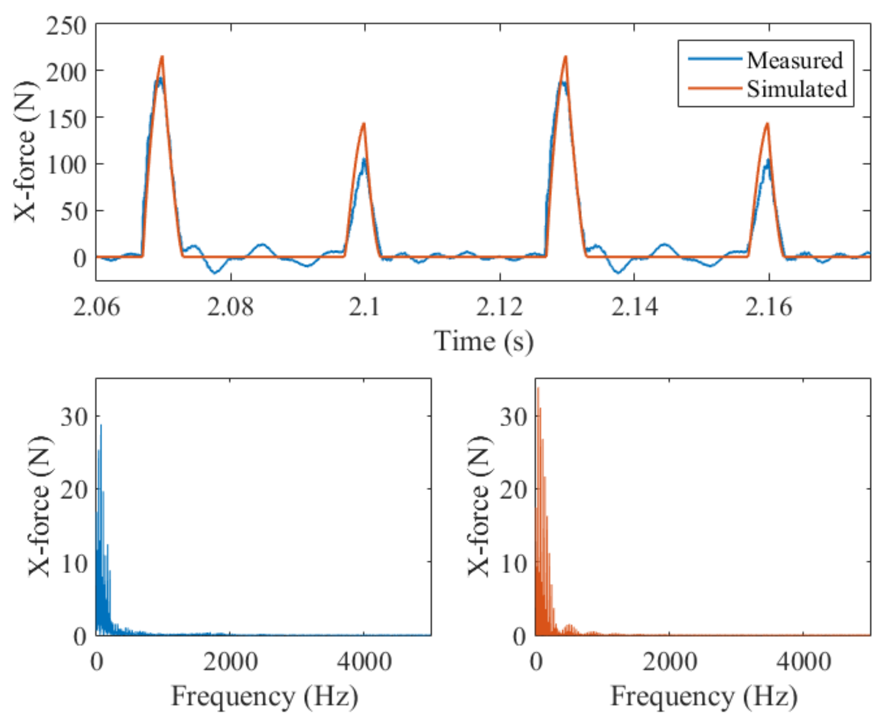

Figure B.5: Measured and simulated *x* direction cutting force shown in the time and frequency domains for the 3 mm thick rib.

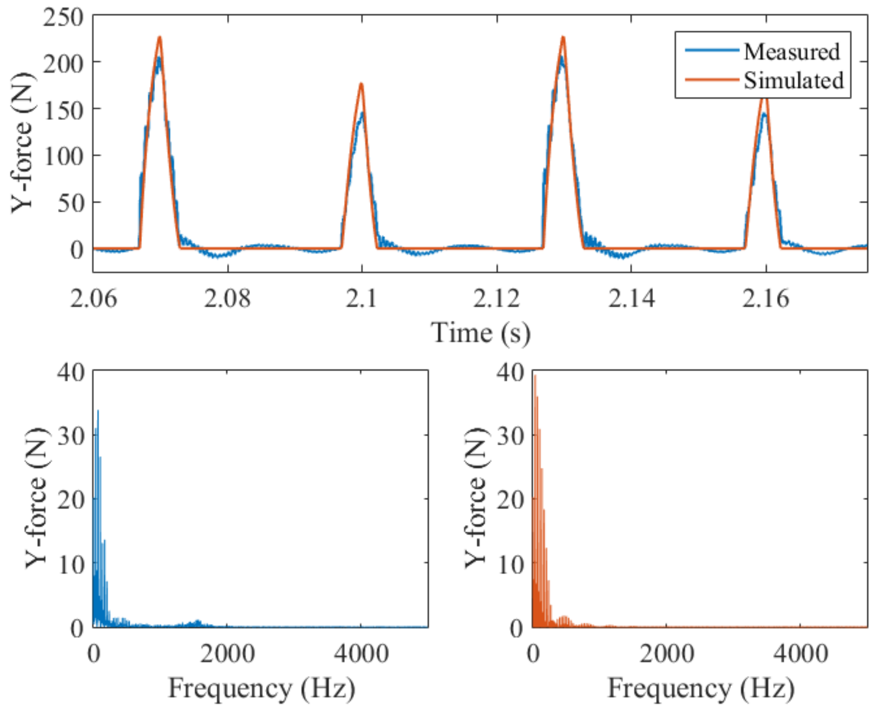

Figure B.6: Measured and simulated y direction cutting force shown in the time and frequency domains for the 3 mm thick rib.

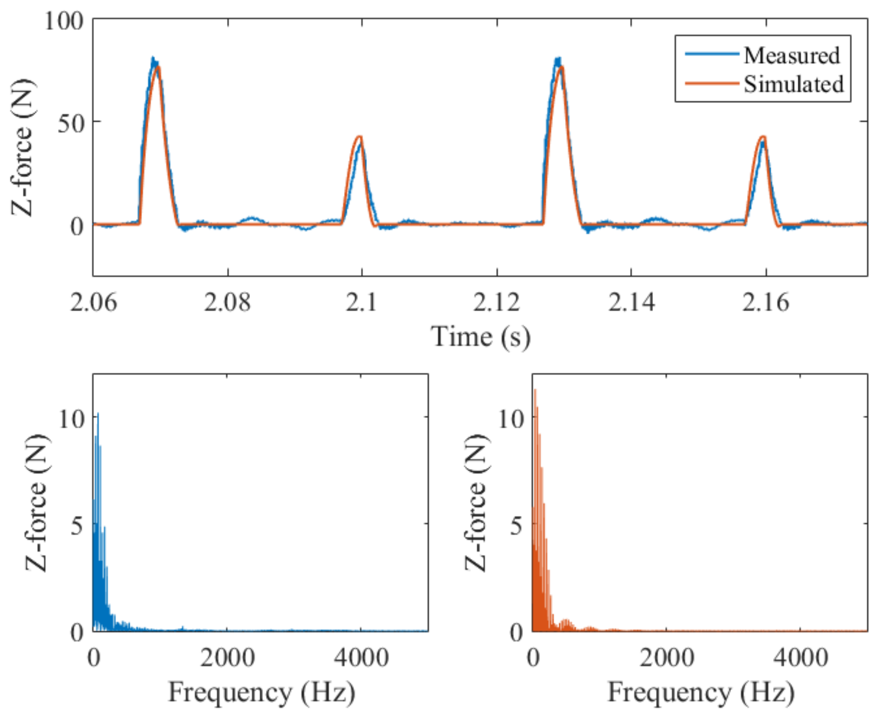

Figure B.7: Measured and simulated z direction cutting force shown in the time and frequency domains for the 3 mm thick rib.

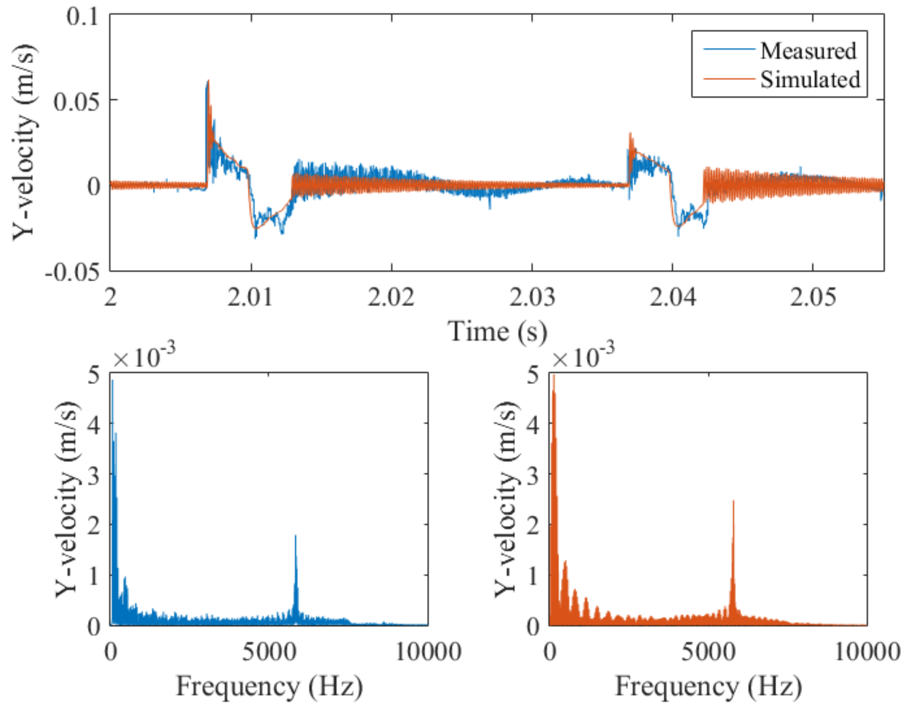

Figure B.8: Measured and simulated *y* direction workpiece velocity shown in the time and frequency domains for the 3 mm thick rib.

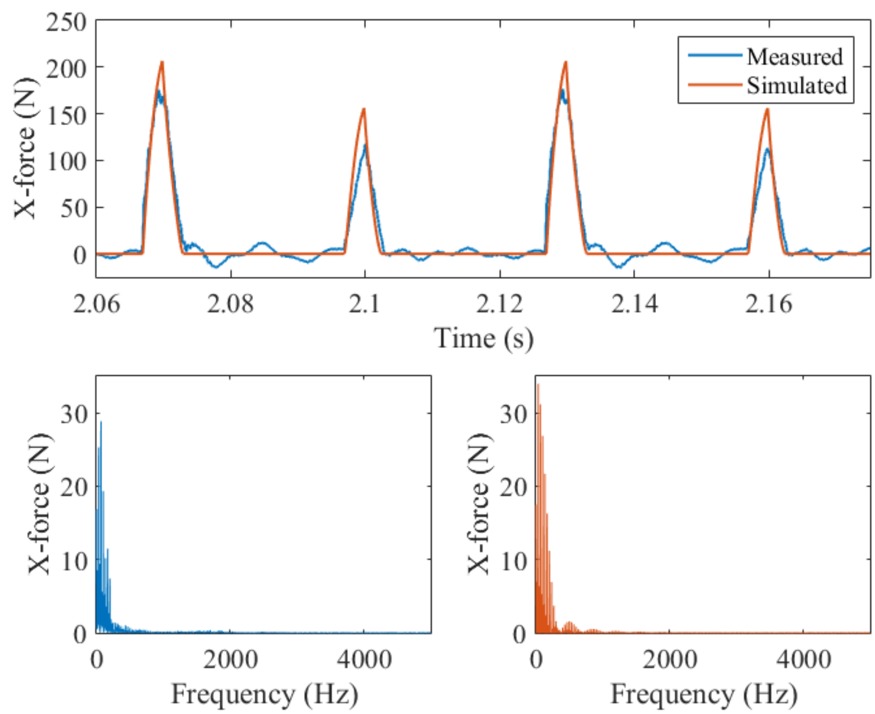

Figure B.9: Measured and simulated *x* direction cutting force shown in the time and frequency domains for the 2.5 mm thick rib.

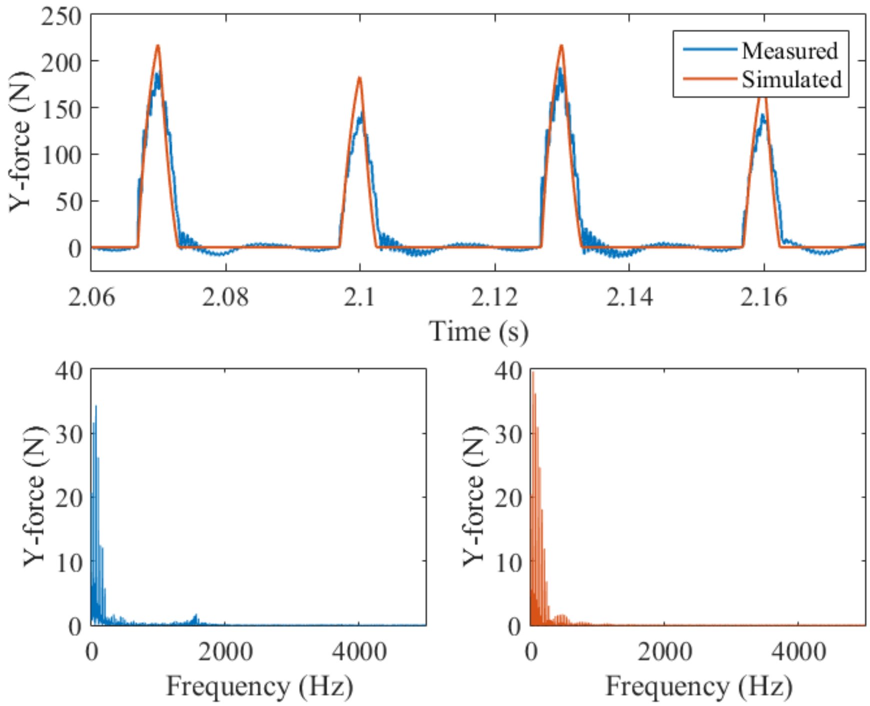

Figure B.10: Measured and simulated *y* direction cutting force shown in the time and frequency domains for the 2.5 mm thick rib.

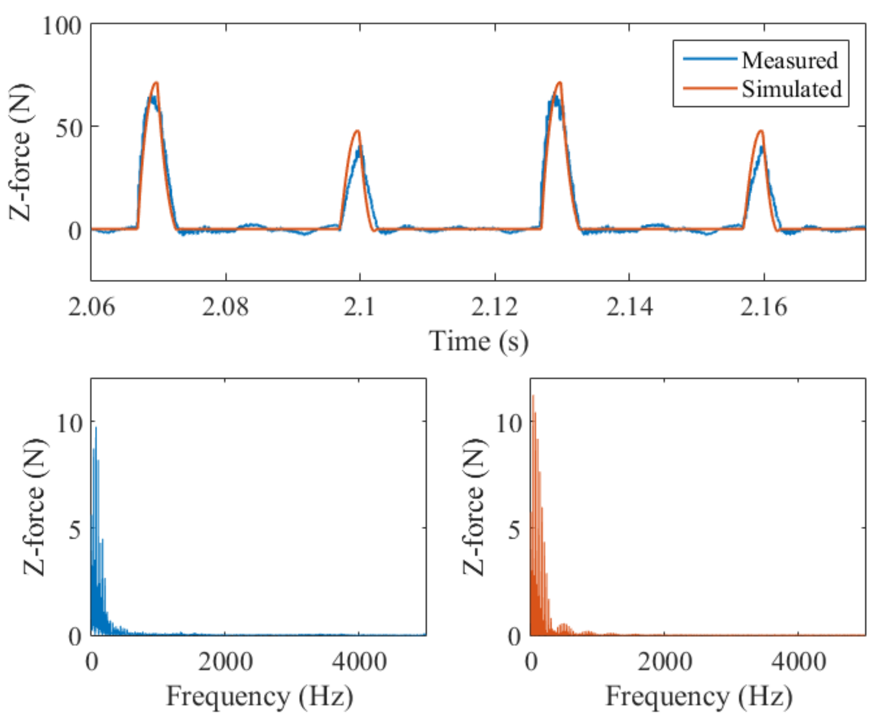

Figure B.11: Measured and simulated *z* direction cutting force shown in the time and frequency domains for the 2.5 mm thick rib.

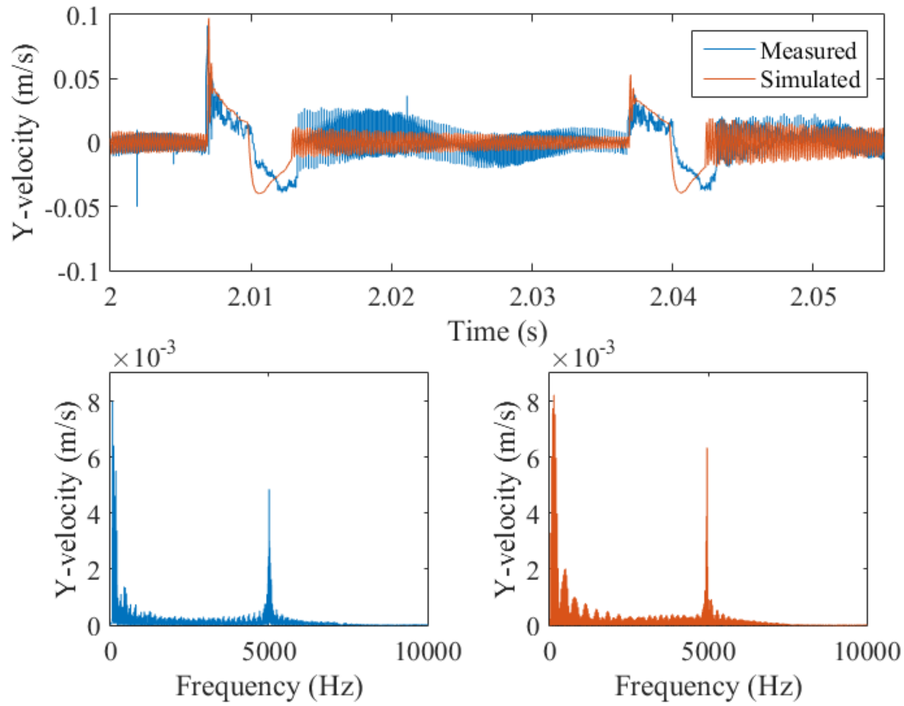

Figure B.12: Measured and simulated y direction workpiece velocity shown in the time and frequency domains for the 2.5 mm thick rib.

B.2 Spatially Dependent Workpiece Dynamics Validation

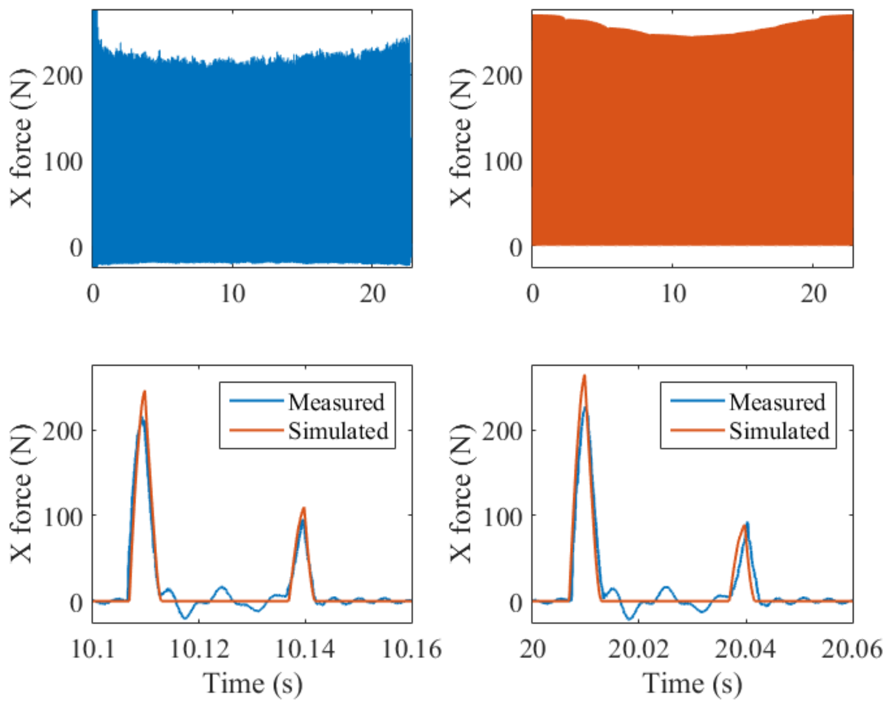

Figure B.13: Measured and simulated cutting forces in the *x* direction over the entire cut length (top) and over one revolution of the two flute cutting tool (bottom).

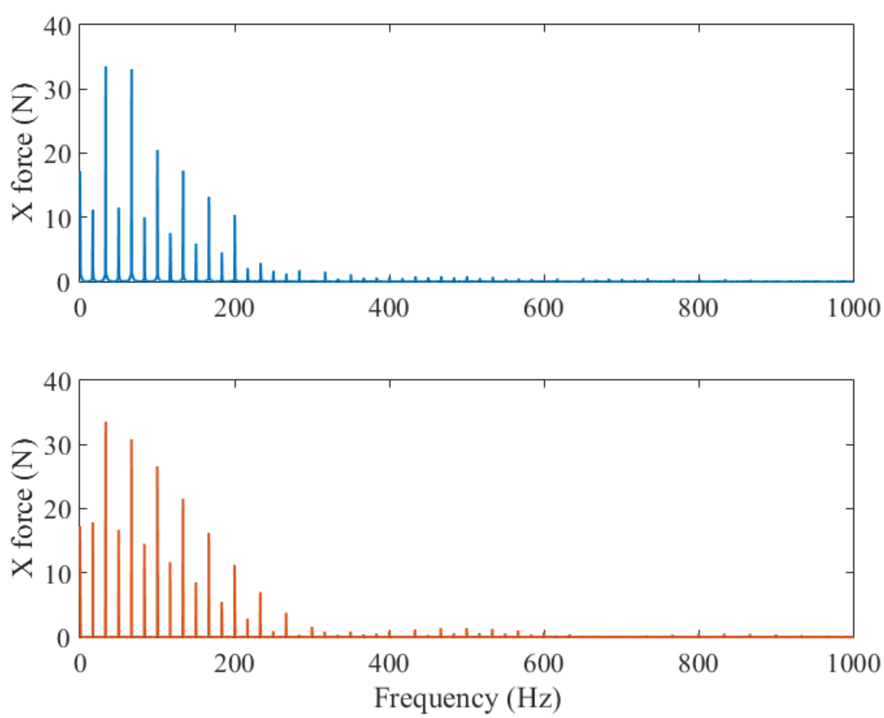

Figure B.14: Frequency content of the measured (top) and simulated (bottom) *x* direction cutting forces.

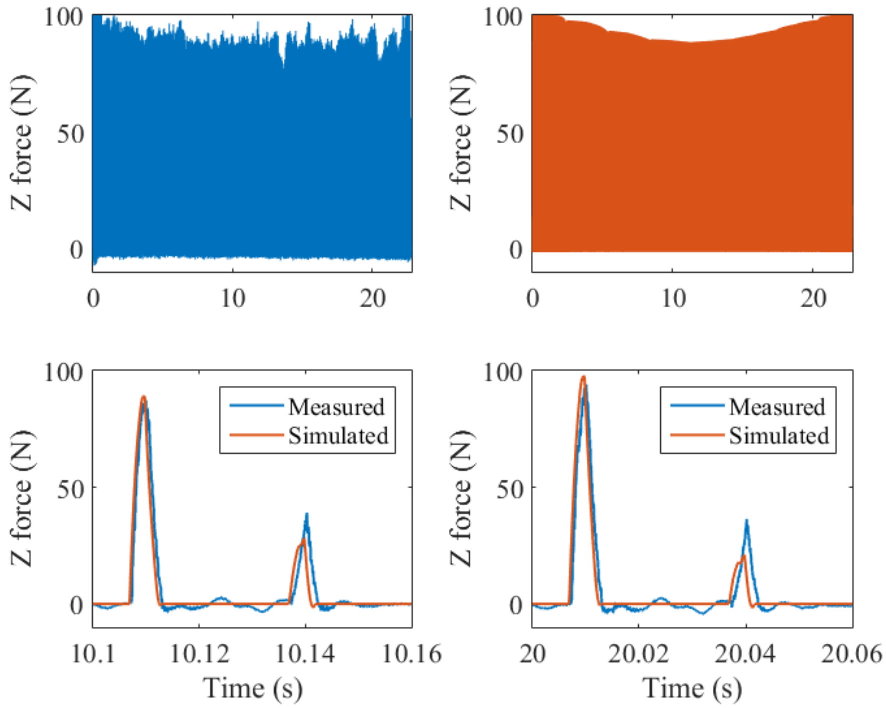

Figure B.15: Measured and simulated cutting forces in the *z* direction over the entire cut length (top) and over one revolution of the two flute cutting tool (bottom).

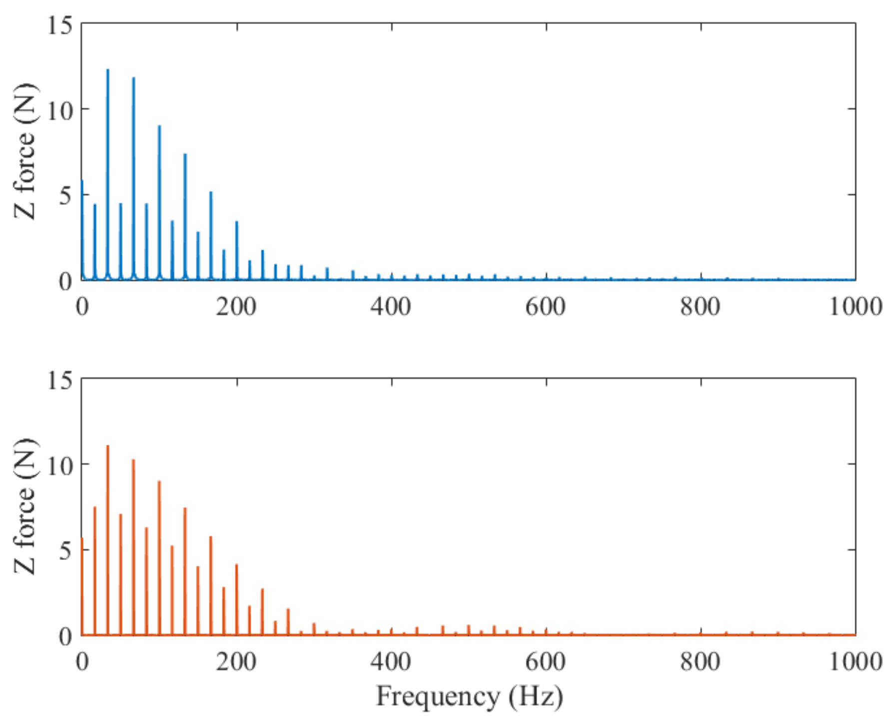

Figure B.16: Frequency content of the measured (top) and simulated (bottom) *z* direction cutting forces.